



**HAL**  
open science

## Single-molecule localization microscopy

Mickaë Lelek, Melina T Gyparaki, Gerti Beliu, Florian Schueder, Juliette Griffié, Suliana Manley, Ralf Jungmann, Markus Sauer, Melike Lakadamyali, Christophe Zimmer

### ► To cite this version:

Mickaë Lelek, Melina T Gyparaki, Gerti Beliu, Florian Schueder, Juliette Griffié, et al.. Single-molecule localization microscopy. *Nature Reviews Methods Primers*, 2021, 1 (1), pp.39. <10.1038/s43586-021-00038-x>. <pasteur-03695794>

**HAL Id: pasteur-03695794**

**<https://pasteur.hal.science/pasteur-03695794v1>**

Submitted on 15 Jun 2022

**HAL** is a multi-disciplinary open access archive for the deposit and dissemination of scientific research documents, whether they are published or not. The documents may come from teaching and research institutions in France or abroad, or from public or private research centers.

L'archive ouverte pluridisciplinaire **HAL**, est destinée au dépôt et à la diffusion de documents scientifiques de niveau recherche, publiés ou non, émanant des établissements d'enseignement et de recherche français ou étrangers, des laboratoires publics ou privés.



HAL Authorization

# Single-molecule localization microscopy

Mickaël Lelek<sup>1</sup>, Melina T. Gyparaki<sup>2</sup>, Gerti Beliu<sup>3</sup>, Florian Schueder<sup>4,5</sup>, Juliette Griffié<sup>6</sup>, Suliana Manley<sup>6\*</sup>, Ralf Jungmann<sup>4,5\*</sup>, Markus Sauer<sup>3\*</sup>, Melike Lakadamyali<sup>7,8\*</sup>, Christophe Zimmer<sup>1\*</sup>

<sup>1</sup>Imaging and Modeling Unit, Institut Pasteur, Paris, France

<sup>2</sup>Department of Biology, University of Pennsylvania, PA 19104-6058 USA

<sup>3</sup>Department of Biotechnology and Biophysics Biocenter, University of Würzburg, Am Hubland, 97074, Würzburg, Germany

<sup>4</sup>Faculty of Physics and Center for Nanoscience, Ludwig Maximilian University, Munich, Germany

<sup>5</sup>Max Planck Institute of Biochemistry, Martinsried, Germany

<sup>6</sup>Laboratory of Experimental Biophysics, Institute of Physics, École Polytechnique Fédérale de Lausanne (EPFL), Route Cantonale, Lausanne, Switzerland

<sup>7</sup>Department of Physiology, Perelman School of Medicine, University of Pennsylvania, Philadelphia, PA 19104-6058, USA

<sup>8</sup>Department of Cell and Developmental Biology, Perelman School of Medicine, University of Pennsylvania, Philadelphia, PA 19104-6058, USA

\* corresponding authors

Author contributions: Introduction (M.Le. and C.Z.), Experimentation (G.B., F.S., J.G., S.M., R.J. and M.S.), Results (M.Le. and C.Z.), Applications (M.T.G. and M.La.), Reproducibility and data deposition (J.G., S.M. and C.Z.), Limitations and optimizations (M.T.G. M.La, F.S., R.J., M. Le and C.Z.), Outlook (M.T.G., M.La, G.B., F.S., R.J., M.S., M.Le. and C.Z.). Overview of the Primer (C.Z.).

## 29 **Abstract**

30 Single-molecule localization microscopy (SMLM) has emerged as a particularly powerful family  
31 of imaging techniques that dramatically improve the spatial resolution over standard, diffraction-  
32 limited microscopy techniques and can reveal biological structures at the molecular scale. In  
33 SMLM, individual fluorescent molecules are computationally localized from diffraction-limited  
34 image sequences, and the localizations are used to generate a super-resolution image, or in some  
35 cases a super-resolution movie or molecular trajectories. In this Primer, we first introduce the  
36 basic principles of SMLM techniques, then describe the main experimental strategies to perform  
37 SMLM, including fluorescent labeling, sample preparation, hardware requirements and image  
38 acquisition in fixed and live cells. We then explain how low-resolution image sequences are  
39 computationally processed to reconstruct super-resolution images and/or extract quantitative  
40 information, and highlight a selection of biological discoveries enabled by SMLM and closely  
41 related methods. We also discuss some of the main current limitations and potential artifacts of  
42 SMLM, as well as ways to alleviate them. Finally, we propose an outlook on advanced techniques  
43 and promising new developments in the fast-evolving field of SMLM. We hope that this Primer  
44 will be a useful reference for both newcomers and practitioners of SMLM.

45

46

## 47 [H1] Introduction

48 The spatial resolution of standard optical microscopy is limited to roughly half the wavelength of  
49 light<sup>1</sup>, as a consequence of the optical phenomenon of diffraction. Because of diffraction, the 'point  
50 spread function' (PSF) — i.e., the image of an arbitrarily small source of light through a lens-  
51 based microscope — is not a point, but an Airy pattern, with a central peak approximately ~200-  
52 300 nm in width (**Fig. 1a**). Diffraction thus leads to a blurring of structures below this spatial scale.  
53 Although light microscopy has been used to study living organisms since the 17th century, the  
54 diffraction limit has severely restricted its ability to study subcellular organization at the scale of  
55 molecules or molecular complexes. For example, the structure of a nuclear pore complex, which  
56 is made up of hundreds of individual proteins, remains obscured by conventional light microscopy  
57 because the entire complex has a diameter of only ~120 nm (**Fig. 1b**). Over the past two decades,  
58 however, microscopy methods have emerged that overcome the diffraction limit and now enable  
59 insights into biological structures such as nuclear pores, viruses, chromatin complexes or  
60 cytoskeletal filaments closer to molecular scales<sup>2</sup>. The most well-known of these super-resolution  
61 microscopy methods fall into three main categories: stimulated emission depletion (STED)<sup>3</sup>,  
62 structured illumination microscopy (SIM)<sup>4,5</sup>, and single molecule localization microscopy (SMLM)<sup>6-</sup>  
63 <sup>9</sup> - the focus of this Primer. SMLM usually employs conventional widefield excitation, and unlike  
64 STED or SIM achieves super-resolution by localizing individual molecules<sup>6-15</sup>. Although each  
65 super-resolution method has its unique advantages and limitations and is optimally suited for  
66 different applications, as discussed elsewhere<sup>2</sup>, SMLM has become broadly adopted in the life  
67 sciences owing to its high spatial resolution and relative ease of implementation.

68 SMLM is fundamentally based on the fact that the spatial coordinates of single fluorescent  
69 molecules (also called fluorophores, or emitters) can be computed with high precision if their PSFs  
70 are isolated (i.e. do not overlap). This is true because, with sufficient oversampling  
71 (magnification), subpixel shifts of the coordinates lead to predictable changes in pixel intensities  
72 (**Fig. 1c**). Localization precision can be defined by standard deviation of the scatter of localizations  
73 that would be obtained if a molecule was imaged and localized many times. For a single molecule,  
74 this precision is fundamentally limited by the number of photons relative to background and noise  
75 — the signal-to-noise ratio (SNR), with higher SNR allowing better precision — and not by the  
76 wavelength of light or the pixel size (**Fig. 1d**). In conventional widefield microscopy, nearby  
77 fluorescent molecules will have overlapping PSFs, preventing their localization (**Fig. 1b,f**). The  
78 central idea underlying SMLM is to avoid these overlaps by separating the fluorescent emissions  
79 of distinct molecules in time. The most common approach to obtain this temporal separation  
80 employs the fact that many fluorescent molecules can switch between an 'active' (or 'bright'/'ON')  
81 state, where they emit fluorescent light when excited, and one or more 'inactive' (or 'dark'/'OFF')  
82 states in which they do not (**Fig. 1e**). While this photo-switching of a particular molecule is a  
83 stochastic (i.e. random) event, the switching probabilities can be experimentally modulated –  
84 using specific fluorophores, laser irradiation, controlling the chemical environment or other means.  
85 Under suitable conditions, this allows one to ensure that at any given time only a small number of  
86 molecules are ON, and hence appear as spatially isolated, non-overlapping PSFs. Many  
87 thousands of image frames of the same field of view (FOV) are then typically acquired  
88 sequentially, so that many (ideally all) fluorescent molecules are ON in at least one frame of the  
89 sequence (**Fig. 1g**). The OFF/ON/OFF switching leads to a 'blinking' of the fluorophores in this

90 sequence of diffraction-limited images. These images are then processed computationally to  
91 detect all ON molecules (**Fig. 1h**) and determine their coordinates (**Fig. 1i**). Finally, all these  
92 localizations are accumulated to assemble a single image, whose resolution is no longer limited  
93 by optical diffraction (**Fig. 1j-I**). The resolution of this image is determined by the accuracy and  
94 precision with which individual molecules are localized, and by the distance between molecules  
95 whose coordinates contribute to the image, which itself depends on the density of molecules and  
96 the percentage of molecules that have been localized (**Box 1**).

97 While this general concept of sequentially imaging sparse random subsets of fluorophores  
98 and computing their positions is common to most forms of SMLM, there are multiple ways to  
99 perform SMLM, wherein technical choices will impact the spatial and temporal resolution, the  
100 ability to perform imaging in 2D or 3D, in one or multiple colors, in fixed or live cells and more.  
101 Instead of generating super-resolution images, very similar experimental approaches to SMLM  
102 can be used to track large numbers of single molecules in live cells in an approach known as  
103 'single particle tracking PALM' (spt-PALM)<sup>16</sup>.

104 A first key choice concerns the fluorophores and how they can be induced to switch  
105 between ON and OFF states. Fluorescence photoactivated localization microscopy<sup>6,7,17</sup>  
106 ((F)PALM) was initially demonstrated using fluorescent proteins (FP) that can be activated by UV  
107 illumination, while (direct) stochastic optical reconstruction microscopy ((d)STORM) and closely  
108 related methods<sup>8,9,18</sup> are based on synthetic fluorophores (dyes) that can photoswitch in the  
109 presence of suitable buffers. Point Accumulation In Nanoscale Topography<sup>10</sup> (PAINT) is a  
110 different SMLM approach that does not require photoswitching, but instead relies on fluorophores  
111 that switch between free diffusion and immobilization by binding to a target. The most prominent  
112 variant of PAINT is DNA-PAINT<sup>19</sup>, where transient immobilization is achieved by hybridization of  
113 DNA strands.

114 A second key parameter is the labeling, i.e. how fluorophores are attached to the target  
115 molecule of interest, e.g. by genetic fusion with a FP or with antibodies.

116 A third important consideration for SMLM is how samples are prepared, e.g. whether and  
117 how they are chemically fixed and what buffer is used to enable or promote photoswitching.

118 Fourth, while the hardware requirements of most SMLM setups are relatively basic, the  
119 details of the optical system affect the resolution and ability to perform multicolor and 3D imaging.

120 A fifth choice is how image sequences are acquired, e.g. how many frames are taken and  
121 with what exposure time, and how laser power is set

122 Sixth, it is crucial to use appropriate software to computationally detect and localize (and  
123 possibly track) single molecules with high fidelity, and, if necessary to quantify the data.

124 Finally, SMLM can suffer from a number of artifacts such as sample drift or overlapping  
125 PSFs, that need to be addressed to ensure high quality images.

126  
127 This Primer article aims to provide an introduction to all main facets of SMLM and some closely  
128 related approaches. The Experimentation section discusses experimental strategies including  
129 choice of fluorophores, labeling, sample preparation, optical system, and image acquisition. The  
130 Results section discusses how to computationally reconstruct and quantify SMLM images. The  
131 Application section highlights examples of biological applications made possible by SMLM. The  
132 remaining sections address issues of reproducibility and data deposition, explore limitations and

133 optimizations of current SMLM techniques, and finally provide an outlook on advanced and  
134 promising new approaches.

## 135 [H1] Experimentation

136 SMLM techniques critically require that the molecules to be imaged (typically, but not exclusively,  
137 proteins) be fluorescently labeled. In an ideal SMLM experiment, the function, location and  
138 number of target molecules would be preserved by the fluorescent labeling and each target  
139 molecule would be tagged at its exact position by exactly one fluorophore of minimal physical size  
140 (although some advanced studies label multiple sites of the same protein or DNA molecule to  
141 determine their 3D conformation, eg. <sup>20,21</sup>). To separate the fluorescent signals in time, each  
142 fluorophore would ideally be briefly active in one image frame and inactive otherwise, hence have  
143 high contrast ratio, and when active should emit a large number of photons relative to the  
144 background to enable high SNR and localization precision. For live cell super-resolution imaging,  
145 active fluorophores should also become inactive very quickly to enable rapid turnover and  
146 sampling, and imaging conditions should be compatible with maintaining the cellular physiology.  
147 Below, we discuss some of the main fluorophores and labeling approaches for SMLM relative to  
148 these ideal requirements. **Table 1** lists a selection of recommended ingredients for newcomers to  
149 SMLM.

## 150 [H2] Fluorophores for SMLM and how to switch them

151 SMLM fluorophores fall in one of five classes, depending on how they switch between ON and  
152 OFF states (**Fig. 2a-e**). Some of these classes include both synthetic dyes and FPs. Compared  
153 to FPs, synthetic dyes generally have higher photon counts and therefore better localization  
154 precision. FPs are generally more suited for live cell applications, but premature bleaching and/or  
155 incomplete labeling can further limit the structural resolution (**Box 1**). Note that for many  
156 fluorophores, the exact molecular mechanisms underlying photoswitching are still under  
157 investigation. We detail these five types of fluorophores and how to use them in SMLM below.

158

## 159 [H3] Photoswitchable fluorophores

160

161 Photoswitchable fluorophores (**Fig. 2a**) undergo reversible transitions from an ON to an OFF-  
162 state, such that a single fluorophore can blink many times. The first synthetic dyes used for SMLM  
163 were photoswitchable dyes, including carbocyanine dyes (Cy5, Alexa Fluor 647), rhodamine and  
164 oxazine dyes (e.g. most Alexa Fluor and ATTO dyes)<sup>22</sup>. These dyes can be reversibly switched  
165 between ON- and OFF-states upon irradiation with light of appropriate wavelength and using a  
166 photoswitching buffer consisting of PBS, 10-100 mM of a thiol such as mercaptoethylamine  
167 (MEA), and an enzymatic oxygen scavenger if necessary. Optimized buffers are available  
168 commercially (**Table 1**). Typically, UV light ( $\lambda_{ON}=405$  nm) promotes activation from OFF to ON,  
169 while light of longer wavelength (e.g.  $\lambda_{OFF}=650$  nm for Cy5) excites fluorescence and induces  
170 transition from ON to OFF. This photoswitching behaviour occurs either in the presence<sup>23</sup> or

171 absence of an activator dye<sup>24</sup> and laid the foundation for STORM<sup>8</sup> and *direct* STORM (*d*STORM)<sup>9</sup>,  
172 respectively.

173  
174 At the beginning of the experiment, all fluorophores reside in their ON-state. Hence, cells can be  
175 easily identified and brought into focus and, standard widefield images can be recorded for later  
176 comparison. To enable SMLM, the vast majority of fluorophores must then be turned OFF. This  
177 usually requires high irradiation intensities ( $\sim 10\text{-}30\text{ kW cm}^{-2}$  at  $\lambda_{\text{OFF}}$ ) over a few seconds. Once  
178 the density of active dyes is low enough to allow single molecule detection, the irradiation intensity  
179 can be decreased to  $\sim 1\text{-}3\text{ kW cm}^{-2}$ . This excitation pumps the active dyes to dark states (inactive  
180 triplet states), which are reduced by the thiol at pH > 7.0. The ON-state lifetime can be adjusted  
181 by the irradiation intensity, the thiol concentration, and the pH of the photoswitching buffer and is  
182 typically 5-20 ms, but can vary from 1 ms to 500 ms<sup>25</sup>. A recent study promotes the use of low  
183 excitation intensity and long exposure time to minimize initial photobleaching and improve  
184 resolution<sup>26</sup>. The reduced OFF-states exhibit a stability of several seconds before they are  
185 transferred back to the singlet ground state upon reaction with residual oxygen<sup>27</sup>. Direct excitation  
186 of the OFF-state at  $\lambda_{\text{ON}}=405\text{ nm}$  can be used to increase the activation and localization rate, e.g.  
187 for low density target molecules. While carbocyanine dyes perform better in the absence of  
188 oxygen, some oxazine dyes such as ATTO 655 also exhibit photoswitching in the presence of  
189 oxygen and require generally lower thiol concentrations. Therefore, it is recommended to vary the  
190 oxygen concentration to optimize the blinking performance for new dyes in (*d*)STORM  
191 experiments. Since cells contain the thiol glutathione at millimolar concentrations, some synthetic  
192 dyes can be used advantageously for live-cell *d*STORM<sup>28</sup>. For novices, we recommend to start  
193 with Alexa Fluor 647 or Cy5 in their first *d*STORM experiments (**Table 1**).

194  
195 Photoswitchable fluorescent proteins (FPs) such as Dronpa<sup>29</sup> can be toggled reversibly from an  
196 OFF state to an ON state upon irradiation with different excitation wavelengths ( $\lambda_{\text{ON}}=405\text{ nm}$ ,  
197  $\lambda_{\text{OFF}}=488\text{ nm}$ ) without requiring any special buffer. Moreover some “standard” FPs (e.g. YFP) can  
198 undergo a spontaneous recovery from OFF to ON states after partial photobleaching, but their  
199 use leads to localizing only a small subset of molecules, hence limiting resolution (**Box 1**).

200

### 201 **[H3] Photoactivatable fluorophores**

202

203 Photoactivatable fluorophores (**Fig. 2b**) essentially reside in their OFF state at the beginning of  
204 the experiment, i.e. the sample is dark, but these fluorophores can irreversibly switch to an ON  
205 state, either spontaneously or upon UV-light ( $\lambda=405\text{ nm}$ ) activation under aqueous conditions.

206 Synthetic photoactivatable dyes include photochromic rhodamine amides<sup>30</sup>, the azetidinyI Janelia  
207 Farm (JF) rhodamine PA-JF<sub>549</sub> and silicon-rhodamine PA-JF<sub>646</sub><sup>31</sup>, and the bridged carbocyanine  
208 Cy5B<sup>32</sup>. Because fluorophores are initially OFF, activation with 405 nm light is usually required to  
209 focus the microscope. To allow single molecule localization, photoactivated fluorophores must be  
210 photobleached, i.e. excited long enough until they permanently turn OFF, prior to activation of  
211 new fluorophores The PA-JF dyes exhibit usually longer ON-state lifetimes and deliver higher  
212 photon yields and localization precisions than the more common dyes they are derived from (e.g.  
213  $\sim 5\text{ nm}$ ) but, on the other hand, require longer total acquisitions times, typically exceeding several

214 hours. A benefit of these dyes is their membrane permeability, rendering them ideally suited for  
215 live-cell SMLM.

216  
217 Photoactivatable fluorescent proteins include PA-mCherry, PA-mRFP ( $\lambda_{ON}=405$  nm,  $\lambda_{exc}=564$   
218 nm), PA-mKate ( $\lambda_{ON}=405$  nm,  $\lambda_{exc}=586$  nm) and PA-GFP<sup>33</sup> ( $\lambda_{ON}=405$  nm,  $\lambda_{exc}=488$  nm) and  
219 have been used in the first demonstration of (F)PALM in fixed cells<sup>6,7</sup> as well as in live cells<sup>16,34</sup>.  
220 For most live-cell applications, photoactivatable FPs such as PAmCherry or PAtagRFP, are  
221 doubtless labels of choice. However, compared to most synthetic dyes, FPs have only moderate  
222 photostability and photon counts, reducing the localization precision<sup>35</sup> and requiring long  
223 acquisition times.

224

### 225 **[H3] Photoconvertible fluorophores**

226  
227 Photoconvertible fluorescent proteins (**Fig. 2c**) including Eos<sup>36</sup> (and its derivatives like mEos2),  
228 Dendra2<sup>36</sup> and mMaple<sup>37</sup> can switch irreversibly from one spectral state (i.e. color) to another  
229 upon irradiation with light of appropriate wavelength. For example, Eos can be switched from  
230 green to red, by irradiation at  $\lambda_{G\rightarrow R}=405$  nm, and is excited at  $\lambda_G=488$  nm and  $\lambda_R=561$  nm,  
231 respectively. For Dendra2,  $\lambda_{G\rightarrow R}=405$  nm,  $\lambda_G=488$  nm and  $\lambda_R=520$  nm.

232  
233 The signal of the (usually weaker) shorter wavelength fluorescence (before photoconversion) can  
234 be used to focus the sample and obtain a diffraction limited image before starting the SMLM image  
235 acquisition sequence. As for the photoactivatable fluorophores, after photoconversion, activated  
236 fluorophores must be photobleached to avoid PSF overlap with newly converted fluorophores,  
237 and the photobleaching time can be controlled by the irradiation intensity. Photoconvertible FPs  
238 are good choices for live cell SMLM.

239

### 240 **[H3] Spontaneously-blinking dyes**

241  
242 Spontaneously blinking dyes (**Fig. 2d**) are based on a pH-dependent chemical reaction  
243 (intramolecular spirocyclization) and enable SMLM at defined pH in an aqueous solution<sup>38</sup> without  
244 requiring a photoswitching buffer. These dyes include the silicon-rhodamine dye HMSiR<sup>39</sup>,  
245 HEtetTFER<sup>40</sup>, and FRD<sup>41</sup>. These fluorophores exhibit excellent photon yield, are partially  
246 membrane permeable, and can thus be used advantageously in live-cell SMLM experiments.  
247 Spontaneously blinking fluorophores show immediate blinking from the onset of an SMLM  
248 experiment. The blinking kinetics is independent of the irradiation intensity and mainly controlled  
249 by the pH of the aqueous buffer. ON-state lifetimes vary in the range of 10-300 ms<sup>38</sup>.

250

### 251 **[H3] Temporarily binding dyes and DNA-PAINT**

252

253 Unlike (F)PALM and (d)STORM, PAINT does not require fluorophores to switch between OFF  
254 and ON states. Instead, PAINT uses dyes<sup>10</sup> or dye-labeled ligands<sup>42</sup> that freely diffuse until they  
255 interact with targets of interest by either permanent or transient binding (**Fig. 2e**). Because free

256 dyes diffuse rapidly over many pixels during acquisition of a single image frame, they only appear  
257 as a blurred background and are not localized, whereas bound dyes appear as a PSF and are  
258 localized. This strategy effectively decouples the switching between ON and OFF-states from the  
259 dye photophysics. PAINT is not prone to photobleaching since the fluorophore reservoir can be  
260 replenished, and bright and photostable fluorescent dyes can be used. Any synthetic dye that  
261 exhibits a sufficient fluorescence quantum yield is compatible with PAINT.

262 DNA-PAINT<sup>43</sup> is a specific variation of PAINT that uses short (typically 6–10 nucleotide long) dye-  
263 labeled DNA oligonucleotides (called ‘imager strands’) that can transiently, yet sequence-  
264 specifically interact with their target-bound complements (called ‘docking strands’) (**Fig. 2e**). In  
265 DNA-PAINT, the ON-times (also called bright times,  $\tau_b$ ) can be almost arbitrarily tuned by the  
266 stability of the DNA duplex, as they are directly linked to the dissociation rate  $k_{OFF}$  of the imager-  
267 docking-duplex via  $\tau_b = 1/k_{OFF}$ . Typical  $\tau_b$  values are approximately 500 ms for an 8 bp duplex  
268 consisting of two CG and 6 AT pairs. As a rule of thumb, increasing the length by one bp results  
269 in roughly an order of magnitude increase in  $\tau_b$ <sup>43</sup>. Fluorescence OFF-times (also called dark times,  
270  $\tau_d$ ) are linked to DNA hybridization rates ( $k_{ON}$ ) and imager concentration  $c_i$  via  $\tau_d = 1/(c_i \cdot k_{ON})$   
271 and can be tuned by either changing  $c_i$  or  $k_{ON}$ . Bright times can be tuned to extract the highest  
272 number of photons per single binding event, resulting in high localization precisions down to ~1  
273 nm<sup>19,44</sup>.

274

## 275 [H2] Fluorescent labeling strategies

276 Several options are available to permanently or transiently link SMLM-compatible fluorophores to  
277 the molecules of interest. The main options are genetic fusion of a FP to the target protein;  
278 immunolabeling with synthetic dye conjugated antibodies; genetic fusion of the target protein with  
279 a tag that can bind to synthetic dyes; direct binding of synthetic dyes for specific structures and  
280 using labels for PAINT and DNA-PAINT. The choice of labeling strategy is critical, as it contributes  
281 to determining the resolution via the linkage error, i.e. the distance between the target molecule  
282 and the fluorophore (**Fig. 2f**), and via the labeling density. It also determines whether the target  
283 molecule retains its physiological localization and whether live cell imaging is possible.

284

## 285 [H3] Encoding fluorescent proteins

286 Genetically-encoded fluorescent proteins (FPs) are the most prominent labels for live cell  
287 fluorescence microscopy and have been used early on for (F)PALM in fixed<sup>6</sup> and live cells<sup>16,45</sup>.  
288 One labeling approach is to transfect cells using an expression vector containing DNA constructs  
289 consisting of the gene encoding the target protein genetically fused to the desired FP<sup>46</sup> (**Table 1**).  
290 An important disadvantage of transient transfection is that the number of expressed target  
291 proteins can vary widely. In stably transfected cell lines, the protein gene is overexpressed, to  
292 levels that can be controlled by construct optimization, but the endogenous protein is left  
293 unlabelled. By contrast, CRISPR knock-ins allow for homozygous labeling of the endogenous  
294 genes, such that protein abundance is not altered and all target proteins are labeled. FPs exhibit  
295 a size of 2-5 nm and can thus also perturb protein functionality<sup>47</sup>. Nevertheless, in the ideal case

296 each protein of interest carries a single FP and shows wild-type functionality. For more details,  
297 see ref.<sup>33,45,48,49</sup>.

298

### 299 **[H3] Immunolabeling**

300 Since synthetic dyes cannot be genetically encoded into biomolecules, they generally need to be  
301 coupled to other compounds, which can bind to a target molecule. Classical immunostaining, in  
302 which an antibody directed against an antigen enables binding of a specific biomolecule of  
303 interest, remains the standard method for labeling endogenous proteins in fixed cells. In direct  
304 immunolabeling, the antibody is chemically coupled to a synthetic dye (e.g. via NHS-chemistry),  
305 but indirect labeling using a second antibody that targets the primary antibody is often used to  
306 ensure higher sensitivity and specificity (**Table 1**). Indeed, the binding of multiple secondary  
307 antibodies to a single primary antibody amplifies the fluorescent signal, and unlabeled primary  
308 antibodies can have better epitope binding affinity than primary antibodies modified for fluorescent  
309 labeling and hence less background. An important drawback of immunolabeling in SMLM,  
310 however, is that the commonly used immunoglobulin G antibodies are large (~10 nm), which  
311 entails a significant linkage error, especially with indirect labeling (linkage errors of ~20 nm).  
312 Camelid antibodies (nanobodies) are substantially smaller (~2.5-4 nm) and therefore offer an  
313 attractive alternative, especially for proteins tagged with GFP, for which highly specific  
314 nanobodies are available<sup>50</sup>, or in combination with primary antibodies.

315 Since immunostaining of intracellular proteins requires permeabilization of cell membranes, it is  
316 also generally incompatible with live cell imaging, except for extracellular or membrane proteins,  
317 and in the latter case can modulate biological functions. The recent development of cell  
318 permeable nanobodies may however facilitate live cell immunolabeling in the future<sup>51</sup>, as do  
319 electroporation based methods<sup>52</sup>. In general, it is important to check that the immunolabeling,  
320 permeabilization and fixation conditions allow specific labeling of the target proteins without  
321 artifacts<sup>53</sup>.

322

### 323 **[H3] Protein tags**

324 To ensure specific labeling with minimal linkage error, an alternative are biorthogonal peptide-  
325 motifs or self-labeling protein tags including FIAsH tags, lipoic acid ligase, SNAP-tags, and Halo-  
326 tags<sup>54-56</sup>. These tags can be genetically co-expressed with a target protein and covalently bind  
327 their respective reagent or ligand, which is directly coupled to a fluorophore. These labeling  
328 methods combine genetic expression with the excellent photophysical properties of synthetic  
329 dyes, while reducing the linkage error to a few nanometers. Furthermore, they can be used for  
330 live-cell imaging experiments as long as the dye-substrate exhibits cell membrane permeability<sup>57</sup>.

331

### 332 **[H3] Direct labeling**

333 Some biological structures can be labeled using dye conjugated small peptides or drugs, such as  
334 the bicyclic heptapeptide phalloidin or the taxane paclitaxel, which target actin and microtubule  
335 filaments, respectively<sup>58,59</sup>. However, despite their small size and minimal linkage error, such  
336 labels often impair biophysical function and act as biological modulators. Additionally, some

337 modified fluorophores can be directly integrated into the biostructure itself (e.g. organelle trackers  
338 or modified lipids)<sup>60</sup>.

339 Regarding polypeptides or proteins, the smallest linkage error can be achieved via site-specific  
340 labeling of a single amino acid. Finally, genetic code expansion enables incorporation of custom-  
341 designed unnatural amino acids, such as TCO\*-lysine, which can be directly coupled to  
342 functionalized synthetic dyes via fluorogenic click reactions without affecting biological  
343 functionality<sup>61-63</sup> and enabling live cell imaging.

344

### 345 **[H3] PAINT and DNA-PAINT labeling**

346 PAINT imaging has initially been restricted to imaging organelles for which transiently binding  
347 fluorescent molecules exist<sup>10,42,64</sup>. For example, PAINT was originally demonstrated by imaging  
348 large unicellular vesicles with the fluorophore Nile Red, which is only weakly fluorescent in water  
349 but becomes much brighter in a lipid environment<sup>10</sup> and has been applied to imaging DNA with  
350 dyes such as Hoechst<sup>65</sup>. DNA-PAINT, by contrast, can be used for any target molecule that can  
351 be linked to a docking strand. For this purpose, the most common approach is again  
352 immunolabeling, with unlabeled primary antibodies targeting the protein of interest and secondary  
353 antibodies conjugated to DNA docking strands using e.g. standard maleimide chemistry<sup>19,66</sup>. To  
354 overcome the large linkage errors of antibodies, DNA-PAINT has recently been combined with  
355 smaller and more efficient labeling reagents including nanobodies<sup>66-68</sup>, genetically-encoded  
356 tags<sup>67</sup>, affimers<sup>69</sup> and novel aptamer probes called SOMAmers<sup>70</sup>.

## 357 **[H2] Sample preparation**

358 To achieve the sampling required for high resolution, dense structures such as the actin  
359 cytoskeleton generally require long acquisition times exceeding minutes. Therefore, cells and  
360 tissue samples must generally be fixed. Nevertheless, sparse and/or slowly moving cellular  
361 structures, such as focal adhesions<sup>34</sup> can to some extent be investigated using live cell SMLM.  
362 Below, we discuss sample preparation for fixed samples and live cell imaging.

363

### 364 **[H3] Fixed samples**

365

366 SMLM in fixed samples demands chemical fixation methods that crosslink proteins, preserve their  
367 binding sites and do not destroy molecular interactions. Aldehyde-based fixatives such as  
368 paraformaldehyde (PFA) and glutaraldehyde have been widely used in fluorescence imaging  
369 applications and are still among the most common fixation reagents for SMLM. Alternatives  
370 consisting of alcohols (e.g. ice-cold methanol) show efficient fixation especially for cytoskeletal  
371 components, but are unsuited to preserve the ultrastructure and molecular organization of cellular  
372 membranes or organelles. In addition, glyoxal has been suggested as an alternative fixative with  
373 improved preservation of cellular morphology for super-resolution microscopy<sup>71</sup>. For the  
374 investigation of dynamic biological processes or protein-protein interactions in membranes,  
375 residual mobility of membrane components must be considered, since it can induce artifacts such

376 as antibody cluster formation. To avoid residual mobility, membrane components should always  
377 be fixed using 4% PFA and 0.2% glutaraldehyde for 30 min or longer<sup>72,73</sup>.

378 For immunolabeling, cells must also be permeabilized. After fixation and permeabilization, a  
379 blocking buffer such as bovine serum albumine (BSA) in PBS or normal goat serum (NGS) can  
380 be used to reduce non-specific binding and background signal before labeling<sup>27</sup>. In cryofixation,  
381 samples are very rapidly cooled down to cryogenic temperatures (<-150°C) under high pressure  
382 to prevent the formation of ice crystals. Although cryofixation is technically more demanding, has  
383 been mostly restricted to thin sections<sup>6</sup> and can affect photoswitching properties, it is compatible  
384 with both SMLM and electron microscopy and achieves optimal preservation of cellular  
385 ultrastructure<sup>74,75</sup> (see Outlook).

386

### 387 **[H3] Live cells**

388

389 For live cell experiments, after expression of the protein of interest and FP or labeling with tag  
390 substrates, cells are imaged in phenol red free medium or PBS. A major limitation of live cell  
391 SMLM are light-induced defects caused by high laser intensities (phototoxicity), especially at  
392 shorter wavelengths. A useful test for phototoxicity is to grow cells in medium overnight at 37°C  
393 and 5% CO<sub>2</sub> and check their survival using cell proliferation assays. A much more sensitive  
394 viability parameter is, however, if the irradiated cells undergo cell division during the next 20-24  
395 hours after the SMLM experiment<sup>76</sup>. The illumination mode, irradiation wavelength and sample  
396 temperature should be adjusted to minimize phototoxic effects<sup>76</sup>.

397

398

### 399 **[H2] Optics of SMLM**

400 Unlike other super-resolution methods, SMLM requires only a wide-field microscope equipped  
401 with standard continuous wave lasers for excitation and activation and a sensitive camera to  
402 detect single molecules (**Fig. 3a,b**). As a result of this relative simplicity, numerous commercial,  
403 low-cost open hardware, and homebuilt implementations exist<sup>77-79</sup>. SMLM compatible cameras  
404 are either electron-multiplying charge-coupled devices (EM-CCDs) or (back-illuminated) scientific  
405 complementary metal-oxide semiconductor (sCMOS) cameras. EM-CCDs use electron  
406 amplification gains that allow detection of single photons with negligible read-out noise and are  
407 particularly suited for low photon counts, despite multiplicative noise due to the stochastic  
408 amplification process. Modern sCMOS cameras have inhomogeneous read-out noise that  
409 requires extra correction, are somewhat less sensitive for weak signals, but have higher frame  
410 rates, larger chips (enabling larger FOV) and achieve similar SNR for bright dyes. The microscope  
411 body itself can be a standard commercial one, but many custom microscopes use more  
412 economical, minimal bodies and may lack an eyepiece and brightfield illumination (**Fig. 3b**).  
413 Because microscopes require much higher stability for SMLM than conventional microscopy,  
414 most commercial or custom microscopes include automated systems to keep the specimen in  
415 focus. For multicolor microscopy (see also **Box 2**), multiple laser lines can be combined and co-  
416 aligned using dichroic mirrors, which reflect and transmit only select wavelengths of light. Several

417 simple approaches are available to enable SMLM in 3D, e.g. through PSF engineering by  
418 inserting a cylindrical lens into the optical path<sup>80</sup> (**Fig. 3d,e, Box 4**). Widefield illumination of the  
419 sample can be generated by expanding a laser beam's circular intensity profile, then cropping the  
420 FOV to keep only the relatively uniform central area.

421 The sample's fluorescence emission is imaged through an objective lens onto the detector.  
422 Typically, a 60-100x, high numerical aperture (NA = 1.4 or higher) oil immersion objective is used  
423 to ensure efficient photon collection. When imaging samples close to the coverslip such as cellular  
424 membranes, total internal reflection fluorescent (TIREF)<sup>81</sup> or highly inclined and laminated optical  
425 sheet (HILO) illumination can be used to diminish out-of-focus background and thereby improve  
426 SNR and localization precision<sup>82</sup>. A dichroic is again used to separate excitation and emission  
427 light; for multicolor imaging a dichroic with multiple bandpasses can be chosen to reflect the  
428 excitation laser lines and pass emission wavelengths. For detection, the camera pixel size should  
429 be well-matched to the PSF size. The optimal magnification can be determined theoretically for  
430 specific background and photon numbers<sup>83,84</sup>, but as a rule of thumb the pixel size should be  
431 approximately equal to half the PSF width. For example, for Alexa 647 dyes imaged with NA=1.4,  
432 the PSF width (FWHM) is 290 nm. With a 60x objective and an EM-CCD camera with 16  $\mu\text{m}$   
433 pixels, the pixel size in the sample plane is 267 nm, and hence too large, while with a 100x  
434 objective, the pixel size is diminished to 160 nm, allowing better localization precision.

435

## 436 **[H2] Data acquisition in SMLM**

437 In SMLM, the number of active fluorophores in each frame should be low enough to avoid PSF  
438 overlaps, but should be as high as possible to minimize acquisition time. However, experimentally  
439 optimizing active fluorophore density can be challenging; for photoswitching dyes, it results from  
440 a balance between excitation and activation laser intensities, and for PAINT from binding affinities  
441 and binder concentration. While these parameters are usually determined manually, SMLM can  
442 be automated with control software that implements a feedback loop to tune active fluorophore  
443 density<sup>85-87</sup>.

## 444 **[H3] Structural imaging in fixed cells**

445 High-resolution studies of biological structures are generally done on fixed or purified samples,  
446 which allow for long acquisitions, to maximize the number of fluorophores localized and minimize  
447 motion artifacts.

448 The exposure time of each frame should ideally match the single molecule ON state lifetime,  
449 which is typically ~10-100 ms (see above). The total number of frames needed to reconstruct an  
450 image depends strongly on the structure being imaged and the desired resolution (**Box 1**). For  
451 higher-dimension structures (e.g. 2D membranes vs 1D filaments), the signal from an ON  
452 fluorophore will overlap with a larger portion of the structure and thus require more frames to  
453 reconstruct<sup>88</sup>. An accurate assessment requires a detailed analysis<sup>34,88,89</sup>, but simple rules of

454 thumb give a rough estimate. For example, a structure like the centriole can be approximated as  
455 a hollow cylinder 250 nm in diameter and 400 nm long, for an area of  $3 \times 10^5 \text{ nm}^2$ , fitting into a  
456 single PSF. To resolve its surface at a scale of 20 nm would require that neighboring localizations  
457 should be at least that close to each other, but due to stochasticity and the need to oversample  
458 to build up the image, it ends up being at least 10 times as many, so approximately 5-10,000  
459 molecules. With only one molecule 'ON' per frame, this implies that at least 10-20,000 frames  
460 should be collected. With a typical per-frame exposure time of 10-100 ms, this implies an  
461 acquisition time of 2-30 minutes.

### 462 **[H3] Structural dynamics in live cell SMLM**

463 For SMLM studies in live cells, two main imaging modes can be distinguished: structural dynamics  
464 and molecular dynamics (**Fig. 4**). Structural dynamics aims to reveal the time evolution of a  
465 structure composed of many molecules, such as a focal adhesion, a clathrin coated pit, or an  
466 organelle membrane<sup>34,60,90</sup>. In these studies, time series of super-resolution images are  
467 constructed from the localizations obtained in consecutive (non-overlapping) sets of frames (**Fig.**  
468 **4a**). Choosing the number of frames in each set faces two conflicting requirements: more frames  
469 imply diminished temporal resolution and potentially motion blur, while less frames imply sparse  
470 sampling of the structure and hence worse spatial resolution<sup>34</sup> (**Box 1**).

### 471 **[H3] Single molecule dynamics in live cells (spt-PALM)**

472 The goal of molecular dynamics is to follow the trajectories of single molecules, often considering  
473 them as a probe of local environmental properties (**Fig. 4b**). Individual molecules are photo-  
474 converted, identified and tracked over multiple frames, in an approach first introduced as 'spt-  
475 PALM'<sup>16</sup>. In order to avoid misconnecting trajectories, the distance between molecules in each  
476 frame should be several times larger than the distance they travel between consecutive frames  
477 <sup>16,42</sup>. This implies that the density of active fluorophores must be significantly lower than for  
478 structural dynamics. Fluorophore motion between adjacent frames becomes a desired  
479 characteristic rather than a problem, so the time between frames should be chosen to allow  
480 molecules to move a distance greater than their localization precision. Although single molecule  
481 tracking existed before SMLM<sup>91,92</sup>, the repeated photoactivation or photoconversion of  
482 fluorophores in live cells allows collection of orders of magnitude more molecular trajectories and  
483 hence enables much more detailed insights into molecular movements and the factors that control  
484 them<sup>93</sup>.

## 485 **[H1] Results**

486 In SMLM, super-resolution images are not seen through the eyepiece of the microscope, but are  
487 assembled in a computer. Thus, the quality of super-resolution images strongly depends on image  
488 processing. Below, we discuss the computational aspects of SMLM data analysis. The majority  
489 of SMLM reconstruction methods can be decomposed in three main consecutive steps: single

490 molecule detection, single molecule localization, and super-resolution image rendering. We  
491 discuss these three steps in more detail below.

## 492 [H2] Single molecule detection

493 In the detection step, each diffraction-limited image is processed to determine the approximate  
494 location of active emitters. Before this, the image is often preprocessed to remove  
495 inhomogeneous background, e.g. using rolling ball, difference of Gaussians or wavelet filtering<sup>94</sup>  
496 or by estimating the background from the entire image sequence<sup>95</sup>. Detection is then typically  
497 done by extracting local maxima from the background-corrected image. Alternatively, the raw  
498 image can be searched for PSF-like patterns, e.g. by computing the correlation of this image with  
499 a small image representing the model PSF (e.g. a Gaussian approximation of the Airy function,  
500 or a more elaborate model for engineered PSFs in 3D SMLM, see **Box 4**) and thresholding the  
501 correlation image. The result is usually a set of pixel regions likely to contain single molecules. It  
502 can be shown mathematically that any detection algorithm will make false positives and/or false  
503 negatives, whenever images are corrupted by noise<sup>96</sup>. The lower the SNR of the image, the more  
504 unavoidable errors. Cameras used in SMLM can in principle have several sources of noise,  
505 including additive noise from thermal electrons (dark current noise), read-out noise, or  
506 multiplicative noise from stochastic amplification of photoelectrons. While read-out is usually  
507 negligible, dark noise can be reduced by using cooled cameras and multiplicative noise by setting  
508 low amplification gain, a fundamentally inevitable noise comes from the fact that fluorophores and  
509 the background emit only a finite number of photons, leading to Poisson noise. High photon counts  
510 relative to the background imply high SNR and therefore better detection performance.

## 511 [H2] Single molecule localization

512 In the crucial localization step, the pixel regions determined above are analyzed further to  
513 compute the subpixelic  $(x, y)$  coordinates of each molecule. We now briefly discuss the  
514 fundamental limits to localization precision and how localizations are computed.

## 515 [H3] Fundamental precision limits

516 Because of noise, localizations cannot be computed exactly, thus algorithms will make errors.  
517 These errors generally have random and systematic parts, as measured by the variance and the  
518 bias<sup>83,84</sup>, and by precision and accuracy, respectively (see **Box 3**). Statistical estimation theory  
519 shows that the precision of an algorithm without bias is limited by the Cramer-Rao lower bound  
520 (CRLB)<sup>97</sup>. This limit depends on the SNR, with higher SNR allowing better precision. A well-known  
521 form of the CRLB is:  $\sigma_{loc} \geq \sigma_0 / \sqrt{N}$ , where  $\sigma_{loc}$  is the precision, defined as the standard deviation  
522 of errors in estimating coordinates,  $\sigma_0$  is the standard deviation of the PSF and  $N$  is the number  
523 of photons collected by the camera (see **Box 3**). Typical values are  $\sigma_0 \approx 100$  nm and  $N = 10^2 -$   
524  $10^4$ , which would predict precision limits of  $\sigma_{loc} \geq 1-10$  nm. However, this simple formula is  
525 generally too optimistic, because it ignores factors such as non-Gaussian PSF shape, read and  
526 amplification noise, background signal, finite pixel size, and dipole orientation, all of which worsen

527 the precision limit. More complex expressions have been derived that take some or all of these  
528 factors into account<sup>84,98</sup>, for example:

$$529 \quad \sigma_{loc} \geq \sqrt{\left(\frac{\sigma_0^2 + a^2/12}{N}\right)\left(\frac{16}{9} + \frac{8\pi\sigma_0^2 b^2}{a^2 N^2}\right)}$$

530 where  $a$  is the pixel size, and  $b$  the background intensity<sup>98</sup>. The CRLB has become an essential  
531 notion in SMLM, because it defines a fundamental limit that all localization algorithms can (and  
532 should) be compared to.

### 533 [H3] Localization algorithms

534 Among the many different localization algorithms that have been proposed, the gold standard is  
535 maximum likelihood estimation (MLE), which approaches the CRLB for high SNR<sup>84,98-100</sup>. MLE  
536 aims to compute the  $(x, y)$  coordinates for which the probability  $p(I; x, y)$  of obtaining the actually  
537 observed image  $I$  (the likelihood) is highest. To find this maximum, MLE algorithms employ an  
538 iterative procedure called ‘gradient ascent’, which starts from an initial position  $(x_0, y_0)$  (e.g. the  
539 center of a pixel identified in the detection step) and displaces it by small increments  $(x_{n+1} = x_n +$   
540  $\delta x_n; y_{n+1} = y_n + \delta y_n)$  designed to increase the likelihood, until it cannot be increased further. The  
541 same approach can be extended to compute 3D  $(x, y, z)$  coordinates (**Box 4**). In practice, MLE  
542 algorithms differ depending on the assumed mathematical model of image formation, including  
543 assumptions on PSF shape, background and noise, and MLE implementations may differ in  
544 technicalities of the gradient ascent procedure. On simulated images, MLE algorithms typically  
545 reach the CRLB, suggesting that their precision cannot be improved upon. A critical requirement  
546 to achieving this in practice is to have an accurate model of the PSF. The widely used Gaussian  
547 models are inaccurate, however, since they do not match the Airy patterns predicted from  
548 diffraction theory. More complex functions based on optical theory provide better PSF models,  
549 but may depend on unknown parameters and fail to capture aberrations due to imperfections of  
550 the optical system and/or induced by the sample. Therefore, it is preferable to calibrate PSF  
551 models, e.g. on real images of subdiffraction fluorescent beads by cubic spline fitting or phase  
552 retrieval, especially in 3D SMLM<sup>101,102</sup>. Unsurprisingly, algorithms that use experimentally  
553 measured PSFs outperform those based on idealized PSFs<sup>99</sup>. Equally important is a good  
554 modeling (or subtraction) of the background, which is often assumed flat, but can also lead to  
555 biases in localizations if not properly accounted for. The iterative nature of MLE generally makes  
556 these algorithms slower than less precise non-iterative algorithms<sup>79</sup>. However thanks to GPUs  
557 and other optimizations, state-of-the-art MLE algorithms now typically allow real-time analysis of  
558 SMLM image sequences<sup>99</sup>.

### 559 [H2] Postprocessing of localizations

560 After localizations are computed for all detected molecule, software apply post-processing steps  
561 to filter out suboptimal localizations, e.g. those with poor computed CRLB, or whose image does  
562 not match the model PSF well. Stringent filtering can easily improve the average localization  
563 precision, but will not necessarily improve resolution, because rejecting localizations  
564 compromises sampling (see **Box 1**). Another important post-processing step is to merge nearby

565 localizations in consecutive frames, which most likely arise from the same molecule, resulting in  
566 a single, more precise localization, without degrading sampling density. In addition, most SMLM  
567 experiments require drift correction, to be discussed later (see 'Limitations and optimizations').

## 568 [H2] Super-resolution image rendering

569 Once all diffraction-limited images have been processed, the extracted localizations are rendered  
570 in a new 'super-resolution' image. Typically, a grid is defined, with pixel sizes similar to the  
571 precision (say,  $\sigma_{loc} = 10$  nm) and counting how many localizations fall into each bin (**Fig. 1k**). This  
572 2D histogram is then visualized like any other image, with counts treated as intensities (**Fig. 1l**).  
573 Minor variations of this image rendering exist. For example, more weight can be given to  
574 localizations with higher intensities, or localizations can be replaced by Gaussian spots with a  
575 standard deviation given by their estimated precision (and normalized to an integral of 1 as  
576 probability densities). The resulting image should have sub-diffraction resolution, provided that  
577 certain conditions are met, as discussed in **Box 1**.

## 578 [H2] Software

579 Because computational processing is crucial to SMLM, over a hundred independent software  
580 packages have now been developed. To help users choose among this plethora of tools, a  
581 challenge has been organized that objectively compares many localization software on simulated  
582 images and a small set of experimental data, and its results are updated on a dedicated  
583 website<sup>99,103</sup>. Although these challenges are not without caveats (software are typically run by  
584 their authors and require expert fine-tuning, and results are contingent on the chosen simulation  
585 assumptions and experimental data), they provide a good starting point for state-of-the-art SMLM  
586 software. See **Table 2** for a selection of recommended software packages.

## 587 [H2] Quantitative analyses

588 Beyond generating super-resolution images for visual inspection, it is often desirable to extract  
589 quantitative information, such as the number, density or spatial distribution of molecules. The  
590 nature of SMLM data as molecular localizations opens distinct possibilities, but also comes with  
591 challenges. We discuss selected quantitative analyses methods for SMLM below.

## 592 [H3] Identifying clusters and counting molecules

593 One common question in SMLM studies of protein distributions is whether these form clusters,  
594 and if so of what size and stoichiometry. Analytic tools from spatial statistics such as Ripley's K  
595 function can help determine if a distribution of points in an image is clustered (or on the contrary  
596 exhibits spatial dispersion) and if so over which length scales. However, applying such tools to  
597 SMLM data is complicated by the fact that a single molecule often gives rise to a cluster of  
598 localizations owing to stochastic blinking and localization errors. Ignoring this can lead to  
599 artifactual clustering<sup>104,105</sup>. One approach to distinguishing apparent single molecule clusters from  
600 real molecular clusters is to determine the statistical distribution of localization errors, and apply  
601 pair-correlation analysis, as was demonstrated in an early study of membrane protein clusters<sup>105</sup>.

602 This early method requires careful calibration, however, and although it provided average sizes  
603 of clusters, it cannot identify and measure individual ones. Analyzing clusters individually requires  
604 segmenting the image into groups of localizations. One proposed solution is a Bayesian method  
605 that can adapt to varying localization precisions<sup>106</sup>, but requires strong assumptions on cluster  
606 shape. Alternative clustering methods include the density-based spatial clustering of applications  
607 with noise algorithm (DBSCAN) and tessellation-based approaches<sup>107,108</sup>.

608 Once localizations are segmented into clusters, a common goal is to count the underlying target  
609 molecules. This is often challenging, however, because some target molecules may be localized  
610 many times, either because of repeated blinking (as in (d)STORM), or because they are labeled  
611 by multiple fluorophores (as in secondary immunolabeling), whereas others may not be localized  
612 at all for lack of labeling (as with partial transfection labeling) or failed photoactivation during  
613 acquisition time<sup>104,105,109</sup>. These confounding factors can be reduced, but not entirely eliminated,  
614 with endogenous homozygous labeling by photoactivatable proteins. In general, calibration  
615 standards are a useful approach to account for repetitive blinking, but also failed photoactivation  
616 and variations in labeling stoichiometry<sup>105,110-114</sup>. Another approach to reduce counting errors is  
617 kinetic modeling of the photoswitching<sup>115</sup>, which has been demonstrated successfully for  
618 photoactivatable proteins and shown to enable correct estimates of the number of copies of a  
619 molecular motor protein in bacteria<sup>116</sup>. However, modeling photoswitching kinetics in the presence  
620 of multiple dark states can be very complex. DNA-PAINT offers a particularly promising avenue  
621 for quantification thanks to well-known kinetics of binding. Its derivative qPAINT<sup>117</sup> uses the fact  
622 that binding frequency (assuming constant probe influx) scales linearly with the number of docking  
623 strands and thus targets. If calibrated for a single site, the number of targets in an unknown region  
624 can be calculated based on the observed blinking frequency, and the virtually unlimited sampling  
625 of target molecules allows minimization of statistical error.

626

### 627 **[H3] Single particle reconstruction**

628 For molecular complexes present in large numbers of identical copies, one can gain structural  
629 information at scales below SMLM resolution, by superimposing and averaging SMLM images of  
630 many individual structures after translations and rotations— as commonly done in electron  
631 microscopy<sup>118,119</sup>. The averaging allows measurement of structural features with a precision that  
632 is only limited by the number of imaged complexes, and not by single molecule localization  
633 precision. This approach has allowed determination of the radial position of nucleoporin epitopes  
634 within nuclear pore complexes with sub-nanometric precision<sup>120</sup> and has been extended to 3D  
635 applications to analyze the structure of human centrioles<sup>119</sup>. Single particle reconstruction is thus  
636 a powerful means to determine subunit architecture of large multi-protein complexes.

### 637 **[H3] Colocalization analyses**

638 Multicolor fluorescence microscopy is commonly used to determine if different molecules  
639 associate. In conventional microscopy, colocalization analyses typically measure the extent to  
640 which the diffraction limited signals from two or more channels overlap or correlate<sup>121</sup>. In multicolor

641 SMLM, strict colocalization should theoretically never occur, since distinct molecules cannot  
642 occupy the same physical location, and colocalization should be replaced by analyses of  
643 distances between molecules. Because of localization errors, however, individual localizations  
644 are better viewed as samples of probability densities, which can overlap for different color  
645 channels if molecules are closer than SMLM resolution. In principle, a simple way to assess  
646 colocalization is to apply established methods for conventional microscopy<sup>121</sup> to pairs of super-  
647 resolution images, but results can be strongly affected by stochastic blinking and/or background  
648 noise. Some recent methods therefore measure colocalization based on the localizations  
649 themselves, e.g. by adapting tools from spatial statistics or using tessellation-based segmentation  
650 of probability densities<sup>122-124</sup>. More work is needed to compare and improve colocalization  
651 methods against solid ground truth data. Regardless of the method used, chromatic aberrations  
652 can pose serious issues and must be carefully measured and corrected using, e.g. multicolor  
653 beads or fluorospheres.

### 654 **[H3] Single molecule tracking**

655 To quantify molecular dynamics in sptPALM<sup>16</sup>, two main approaches can be distinguished:  
656 Lagrangian and Eulerian. Lagrangian methods focus on characterizing the dynamics of individual  
657 molecules by following them individually, for example by computing mean-squared displacements  
658 and estimating diffusion coefficients or transport states for each molecule<sup>16,125</sup> (**Fig. 4b**). Eulerian  
659 methods instead focus on individual regions in the sample and use the dynamics of molecules  
660 passing through them to infer local properties that characterize or affect molecule dynamics, e.g.  
661 maps of diffusivity or energy potentials<sup>126</sup>. For both approaches, it is important to take into account  
662 the fundamental uncertainties discussed above, to avoid biases in the analysis of molecular  
663 dynamics such as apparent subdiffusion or spurious energy potentials due to random localization  
664 errors<sup>127,128</sup>. More extensive discussions of single molecule tracking methods can be found in  
665 refs<sup>93,129</sup>.

### 666 **[H3] Other quantification methods**

667 Many more methods have been developed to analyze SMLM point clouds in specific or generic  
668 contexts. These include various methods to segment structures from the background to analyze  
669 their morphologies, as shown e.g. for dendritic spines in neurons<sup>108</sup>, or cytoskeletal filaments, e.g.  
670 to measure their orientation, lengths or curvature<sup>130,131</sup>. Another example are iterative hierarchical  
671 clustering methods, to classify the morphology of protein aggregates<sup>132</sup>. Given the variety of  
672 techniques and the current lack of comparative assessments, careful validation of each  
673 quantification method on simulated and experimental data remains critical. For more complete  
674 discussions of SMLM data analysis, see refs<sup>107,133,134</sup>.

## 675 **[H1] Applications**

676 Compartmentalization of cells is crucial for regulating cell function. In recent years, SMLM has  
677 enabled us to visualize the spatial organization of proteins and nucleic acids within sub-cellular

678 compartments with nanoscale resolution. Below we summarize major new biology emerging from  
679 these studies, focusing on specific sub-cellular compartments including the nucleus, cell  
680 cytoplasm and plasma membrane.

## 681 [H2] Nucleus

682 Despite being a compartment of its own, the nucleus communicates with the rest of the cell  
683 through the nuclear pore complexes, transport portals that allow protein and nucleic acid  
684 exchange with the cytoplasm. Advances in SMLM have facilitated the study of the cell nucleus  
685 and the visualization of intranuclear structures and nuclear pores.

## 686 [H3] Chromatin Organization

687 Recent studies have demonstrated that chromatin is not randomly distributed inside the nucleus  
688 but is intricately folded and spatially organized<sup>135</sup>. SMLM methods are playing an important role  
689 in deciphering the organization of the human genome at length scales that are inaccessible to  
690 standard light microscopy (20-100 nm or 10 kB-1 Mb) and that are important for regulating gene  
691 function (for a recent review see ref<sup>136</sup>). Chromatin compaction has been thought to follow a  
692 hierarchical order where nucleosomes form a 10 nm fiber that resembles beads on a string, which  
693 further compacts into a 30nm fiber. However, this textbook view has been challenged in recent  
694 years. SMLM enabled the visualization of “nucleosome clutches” consisting of tens to hundreds  
695 of nucleosomes (few Kb in genomic scale and 20-100 nm in spatial scale) along the chromatin  
696 fiber in interphase nuclei of somatic cells. Similar results, in which nucleosomes pack into  
697 nanodomains of varying sizes were obtained by live cell super-resolution imaging<sup>137</sup> and recently  
698 recapitulated at specific genomic loci using mesoscale modeling<sup>138</sup>. While clutch size may be  
699 underestimated, especially in compact chromatin regions, due to imperfect labeling, these results  
700 suggest that chromatin packing in the nucleus is more heterogeneous than the regular 30 nm  
701 fiber (**Fig. 5a**)<sup>139</sup>. Clutch size was cell-type specific and depended on epigenetic histone  
702 modifications<sup>140,141</sup>, suggesting that it can be a regulator of gene activity. While labeling of histones  
703 relies on immunostaining or over-expressing a tagged histone and the labeling efficiency depends  
704 on epitope accessibility to the antibody or the incorporation of tagged histones into nucleosomes,  
705 DNA itself can be labeled very efficiently using modified nucleotides and click chemistry<sup>140,142</sup>.  
706 Dual color SMLM imaging of histones and DNA showed a high level of co-localization between  
707 the two compartments as expected, suggesting that SMLM histone images are representative of  
708 chromatin organization within the nucleus<sup>140</sup>.

709 Similarly, SMLM imaging of DNA labeled with Oligo-Paint probes showed that distinct epigenetic  
710 states follow distinct DNA packing and spatial organization in *Drosophila* cells<sup>143</sup>. In addition to  
711 the nucleosomal level, SMLM was also used to study larger chromatin domains including  
712 topologically associating domains (TADs), which are Megabase regions (100-500 nm length  
713 scale) of DNA determined by genome-wide chromosome conformation capture (Hi-C), within  
714 which DNA sequences interact more frequently with each other than with neighboring DNA  
715 sequences outside of TADs<sup>144</sup>. SMLM, in combination with multiplexed DNA-FISH (fluorescence  
716 in situ hybridization) methods, showed that the boundaries of TADs are more variable in single

717 cells than previously thought using population Hi-C<sup>20,145</sup>, highlighting the importance of visualizing  
718 these small domains at high resolution in single cells.

719 For recent reviews of high resolution imaging of chromatin see refs.<sup>136,146</sup>.

### 720 **[H3] Transcriptional machinery and nuclear proteins**

721 Live-cell SMLM has been used to visualize the dynamics and spatial organization of the  
722 transcriptional machinery, in particular RNA Polymerase II (RNA PolII)<sup>147</sup>. These studies showed  
723 that RNA PolII assembled into transient nuclear clusters, with lifetimes that correlated with their  
724 mRNA output, suggesting that they are transcriptionally active<sup>148</sup>. Follow up work showed that at  
725 least some of the RNA PolII clusters were phase separated liquid droplet condensates,  
726 particularly in genome regions known as super-enhancers<sup>149</sup>. SMLM further showed that several  
727 nuclear proteins, including architectural proteins like CCCTC-binding factor (CTCF) and the  
728 Polycomb group proteins, form nano-sized clusters within the nucleus<sup>150,151</sup>. Hence, clustering of  
729 nuclear proteins may be a general phenomenon for both shaping genome organization and  
730 regulating transcriptional output. Live cell SMLM will be important to determine if nuclear proteins  
731 form phase separated clusters that cannot be resolved with conventional microscopy.

### 732 **[H3] Nuclear Pore Complex (NPC)**

733 NPCs are excellent reference structure for characterizing and further improving super resolution  
734 microscopy modalities<sup>113,152,153</sup>, and SMLM studies have helped to elucidate the structure of  
735 NPCs<sup>120,152</sup>. Most recently, live-cell high-speed single-molecule microscopy enabled the  
736 visualization of protein domains translocating through NPC channels and gave insight into  
737 transmembrane protein transport<sup>154</sup>. Finally, as previously mentioned, the arrangement of  
738 individual subunits within the NPC was elucidated by combining SMLM with single particle  
739 averaging<sup>120,152</sup> (**Fig. 5b**). This approach promises to be a powerful method for elucidating the  
740 subunit architecture of large multi-protein complexes.

## 741 **[H2] Cytoplasmic contents**

### 742 **[H3] Microtubules**

743

744 Microtubules were an early target structure to visualize with SMLM and validate SMLM methods  
745 due to their known shape and size (polymers with a diameter of 30 nm), as well as the abundance  
746 and ease of labeling of microtubule subunits ( $\alpha$ -tubulin and  $\beta$ -tubulin)<sup>80 155</sup>. Besides being good  
747 test structures for SMLM, microtubules also play several important cellular functions including  
748 facilitating long-range transport and cell division. Combining super-resolution imaging of  
749 microtubules with single particle tracking of sub-cellular compartments enabled visualization of  
750 how these compartments are transported within the complex microtubule network in the crowded  
751 cell cytoplasm<sup>156 157 158</sup>. These studies uncovered that a special subset of microtubule tracks that  
752 are detyrosinated, play a crucial role in transporting and spatially organizing lysosomal and  
753 autophagosomal compartments to regulate autophagy<sup>158</sup>.

### 754 **[H3] Mitochondria, lysosomes and the endoplasmic reticulum**

755 The photoswitching capability of common membrane probes specific to mitochondria,  
756 endoplasmic reticulum (ER) or lysosomes has further enabled visualizing the dynamics of these  
757 organelles with high spatial (30-60 nm) and temporal (1-2 s) resolution, revealing for example  
758 fusion and fission dynamics of individual mitochondria<sup>60</sup>. SMLM has resolved the organization of  
759 mitochondrial sub-compartments including mitochondrial inner and outer membrane, cristae and  
760 nucleoids<sup>159</sup>. SMLM revealed that mitochondrial nucleoids are heterogeneous in terms of their  
761 shape and size, are closely associated with the inner mitochondrial membrane, and that  
762 mitochondrial DNA inside nucleoids is more condensed than previously thought<sup>160</sup>. Low-resolution  
763 images suggested that the morphology of the ER consisted of tubules and sheets. Combining  
764 lattice light sheet (see 'Outlook') and PAINT, it was shown that these apparent ER-sheets are in  
765 fact very dense tubular structures, changing the textbook perception of this crucial organelle<sup>161</sup>.

## 766 [H2] Plasma membrane

767 Because the plasma membrane can be imaged with TIRF<sup>81</sup>, which affords improved resolution,  
768 SMLM is ideally suited to study the molecular organization of the plasma membrane with  
769 fluorescently labeled antibodies, toxins or ligands. SMLM has been instrumental in revealing that  
770 membrane receptors are often not uniformly distributed but sequester into small, functional nano-  
771 domains too small to be resolved with conventional light microscopy. One early PALM study  
772 showed for example how clusters of GPI-anchored proteins are disrupted by cholesterol  
773 depletion<sup>105</sup>. Recent studies used *d*STORM to investigate the effect of inflammatory activation on  
774 the clustering of tumor necrosis factor receptor 1 (TNFR1)<sup>162</sup> or the toll-like receptor TLR4<sup>163</sup>, and  
775 sensitive detection of very low levels of an antigen in myeloma cells, with implications for cancer  
776 immunotherapy<sup>164</sup>. Earlier SMLM studies found that T cell antigen receptor (TCR) and linker for  
777 activation of T cells (Lat) are found in separate protein islands that concatenate after T-cell  
778 activation<sup>165</sup>. Subsequent studies revealed that TCR nano-clusters have a functional role in  
779 antigen recognition and therefore signal initiation<sup>166</sup>. However, this view has been recently  
780 challenged with quantitative super resolution imaging methods that attributed the clustering to  
781 overcounting artifacts<sup>167</sup>, emphasizing the importance of careful quantitative analyses of SMLM  
782 data. More applications of SMLM to plasma membrane organization and associated challenges  
783 are discussed e.g. in ref. <sup>168</sup>

784 The plasma membrane interacts with the extracellular matrix (ECM) through focal adhesions,  
785 which are crucial both for cell adhesion and migration. iPALM, an advanced form of SMLM (see  
786 'Outlook') was used to study the 3D organization of proteins within focal adhesions<sup>169</sup>. This work  
787 revealed the layered organization of focal adhesions, in which integrins and actin are separated  
788 by 40nm vertically (**Fig. 5d**), a region that comprises several layers; a membrane-apposed layer  
789 containing integrin tails, paxillin and focal adhesion kinase, an intermediate layer with talin and  
790 vinculin and an upper layer with actin regulators such as zyxin,  $\alpha$ -actinin and vasodilator-simulated  
791 phosphoprotein. More recently, using SMLM, talin — but not vinculin — was identified as the  
792 primary determinant of focal adhesion organization as it diagonally spans the 40nm focal  
793 adhesion core region and acts as a molecular ruler<sup>170</sup>.

## 794 [H2] Neuronal synapses and axons

795 Neurons are the most compartmentalized cells with a highly polarized and extended morphology  
796 in which the cell soma is separated from axonal, dendritic and synaptic compartments. The size  
797 of the synapse is below the diffraction limit, since the distance between the pre-synaptic and post-  
798 synaptic structures is ~20-30 nm. SMLM has been particularly useful in elucidating synaptic  
799 organization as it can readily resolve pre-synaptic and post-synaptic markers and determine the  
800 molecular architecture of proteins within synapses<sup>171</sup>. For example, SMLM revealed the  
801 nanoscopic organization of Bruchpilot (Brp) proteins within the synaptic active zone (AZ), a  
802 structure found within the presynaptic terminal in *Drosophila*<sup>172</sup>. Quantitative analysis further  
803 estimated the precise stoichiometry of the Brp proteins within nanoscopic complexes, showing  
804 that there are hundreds of these proteins within the AZ arranged in several heptameric clusters<sup>172</sup>.  
805 Moreover, SMLM allowed the detection of AMPA and NMDA receptor nanoclusters within the  
806 post-synapse, a finding with important implications for the regulation of synaptic transmission<sup>173-  
807 175</sup> and a recent dSTORM study analyzed glutamate receptor clustering at presynaptic active  
808 zones of the mouse cerebellum<sup>176</sup>.

809 Neuronal axons are densely packed with proteins, and therefore, challenging to image with  
810 conventional microscopy. One of the most striking findings enabled by SMLM was the discovery  
811 of actin rings with highly regular periodicity of <200 nm, wrapped around the circumference of  
812 neuronal axons (**Fig. 5c**)<sup>58</sup>. Moreover, spectrin also demonstrated similar periodicity to actin and  
813 was further shown to be interconnected with actin, resulting in the formation of a quasi-1D lattice  
814 structure, also known as the membrane-associated periodic scaffold (MPS).

## 815 [H2] Microbes

816 In addition to helping reveal the organization of cells, SMLM is well adapted to shed light on the  
817 inner structure of microbes and on how they can subvert the cellular machinery for their own  
818 purposes. SMLM is especially relevant for viruses, most of which are smaller than the diffraction  
819 limit, e.g. the HIV virion has a diameter of only ~100 nm. Unsurprisingly, SMLM or spt-PALM have  
820 been used to revisit the internal structure of all facets of their replication cycle from cellular entry,  
821 intracellular transport, replication, assembly, release and maturation for viruses such as HIV,  
822 herpes simplex virus, or respiratory syncytial virus<sup>177-183</sup> and SMLM approaches are also currently  
823 used to study SARS-CoV-2 infected cells. While bacteria are typically somewhat larger than the  
824 diffraction limit (~1 um in width and 2-3 um in length), SMLM has also proven very useful to  
825 analyze their internal architecture, for example to reveal the helical organization of the cytoskeletal  
826 protein FtsZ<sup>184</sup>, or the organization of nucleoid associated proteins in *E coli*<sup>185</sup>. SMLM has also  
827 helped to clarify how bacteria interact with host cells, e.g. by visualizing septin cages entrapping  
828 *Shigella* as part of a cellular defense mechanism<sup>186</sup>. For more applications of super-resolution  
829 imaging to bacterial pathogens, see ref. <sup>187</sup>.

## 830 [H1] Reproducibility and data deposition

831 SMLM involves a much larger number of experimental and analytical parameters than  
832 conventional microscopy studies. Furthermore, the intrinsic stochasticity of single molecule  
833 blinking makes typical SMLM images particularly noisy. These factors pose a challenge to

834 reproducibility of SMLM experiments. Therefore, it is especially important to carefully document  
835 experimental protocols and computational analyses and to make data and software available. On  
836 the software side, many free and open source software tools for SMLM are now available and  
837 have been compared using shared benchmarking data<sup>99</sup>, but there is still a need to record and  
838 share the analysis parameters used, such as filtering on photon counts or localization precision.  
839 Competitions that benchmark downstream analyses such as cluster identification or single particle  
840 reconstruction will be useful to complement the challenges on localization. Platforms that integrate  
841 and compare existing tools would be useful to increase reproducibility of quantitative analyses.

842

843 On the data side, image deposition is increasingly recognized as important, leading to data  
844 sharing initiatives in the microscopy community, such as through archiving on Zenodo, FigShare,  
845 BioStudies and to some extent the Image Data Resource<sup>188</sup>. However, the large image volumes  
846 generated by SMLM experiments are an impediment to raw data sharing. Therefore, we propose  
847 that a good first step is to share localization data together with minimal information about the  
848 experiment. These data should include the target molecule(s) and/or epitope(s); the fluorescent  
849 labeling technique used with details of antibody concentrations and the functionality of FP tagging;  
850 the fixation protocol if relevant; microscope parameters such as laser wavelength, laser power  
851 density, camera type, exposure time, pixel size, objective magnification, numerical aperture and  
852 immersion medium; reconstruction software and parameters used, and a localization table  
853 including at least x,y coordinates and frame numbers, and preferably photon counts. A community  
854 resource that allows users to catalogue data doi with this information appended could catalyze  
855 data sharing and reuse and improve reproducibility in SMLM.

## 856 **[H1] Limitations and optimizations**

857

858 Although powerful, current SMLM techniques face a number of limitations. These include  
859 susceptibility to reconstruction artifacts, difficulties in imaging thick samples or tissues, and very  
860 low throughput, and limited applicability in live cell imaging. In this section, we highlight some of  
861 these limitations as well as optimizations to alleviate them.

862

## 863 **[H2] Reconstruction artifacts and solutions**

864 Several types of artifacts can affect the quality of reconstructed super-resolution images, including  
865 drift, overlapping PSFs, and localization biases.

## 866 **[H3] Sample drift**

867 A very common issue in SMLM is sample drift relative to the objective during image sequence  
868 acquisition, which is often unavoidable, even when using autofocus systems designed to limit  
869 axial drift . If ignored, even small drifts can result in blurring of the reconstructed image or even  
870 generate artefactual features, e.g. shadow microtubules<sup>79</sup> (**Fig. 6a**). However, drift can be  
871 measured, typically by tracking fiducial markers, such as fluorescent beads or gold coordinates

872 (which ideally remain fluorescent for the entire experiment), and the coordinates can then be  
873 corrected, simply by subtracting the estimated drift (**Fig. 6a, Table 1**). An interesting recent  
874 alternative is to estimate the drift from speckle patterns generated by back-scattered light<sup>189</sup>. For  
875 highly redundant structures such as microtubules, the lateral drift can also be estimated directly  
876 from the single molecule localizations alone using e.g. image cross-correlation, although this  
877 requires more caution<sup>190,191</sup>. Since axial drift can also deteriorate 2D SMLM images, 3D drift  
878 correction methods should be used whenever possible<sup>102,189,192</sup>. Many SMLM software packages  
879 provide drift correction tools (**Table 2**). Unlike drift, high frequency vibrations that affect  
880 localization precision by blurring individual diffraction-limited frames cannot be corrected  
881 computationally. Therefore, it is important to isolate the microscope from sources of vibration. The  
882 best way to avoid residual vibrations and drift artefacts is to eliminate them using active, real-time  
883 adjustment of the stage position<sup>191,193,194</sup>. For example, fiducial markers added to the coverslip  
884 can be tracked with a second camera and a closed loop system to drive piezoelectrical actuators  
885 that precisely reposition the stage<sup>195</sup>. Such approaches, although technically more demanding,  
886 can reduce drift to single nanometers or less<sup>195-197</sup>.

### 887 **[H3] Overlapping PSFs**

888 Although the basic principle of SMLM assumes spatially isolated PSFs, avoiding PSF overlaps  
889 entirely is difficult, especially in high density regions. Furthermore, it can be desirable to increase  
890 the activation probability (hence leading to PSF overlaps) to increase imaging speed. Standard  
891 localization algorithms tend to treat overlapping PSFs as a single molecule and compute an  
892 incorrect position located somewhere in between. This can for example lead to an artificial blurring  
893 at intersecting filaments (**Fig. 6b**). In principle, such artifacts can be alleviated by stringent filtering  
894 of localizations for which the image deviates from that of a single PSF. However, stringent filtering  
895 can lead to reject most localizations and lead to the paradox that high density regions appear  
896 dimmer than low density regions in the reconstructed image (**Fig. 6c**). A simple but effective  
897 approach to detecting such artifacts is to verify if a blurred version of the super-resolution image  
898 is consistent with the widefield image. This approach yields a map that can highlight regions  
899 affected by reconstruction errors<sup>198</sup>.

900 To avoid these artifacts and analyze images with high activation density, several ‘multi-emitter  
901 fitting’ algorithms have been developed that explicitly allow for PSF overlaps<sup>99,103</sup> or compute  
902 differences between consecutive images to create images closer to single molecule conditions<sup>199</sup>.  
903 Some related methods even dispense of the notion of localizing single molecules altogether<sup>200</sup>.  
904 These algorithms can indeed produce super-resolution images. However, overlapping PSFs  
905 necessarily imply significantly poorer resolution compared to low density SMLM regimes<sup>99,103,201</sup>.

### 906 **[H3] Other biases**

907 Several other artifacts can occur in absence of drift or PSF overlaps. One example is a localization  
908 bias within the camera pixel, which can arise, for example, from ill convergence of MLE algorithms  
909 due to a mismatch between the model PSF and the actual PSF, and result in images with apparent  
910 grid patterns<sup>202</sup> (**Fig. 6d**). This type of bias can be easily identified from the histogram of  
911 localizations relative to pixel centers (**Fig. 6d**). It is less easy to identify spatially varying biases,

912 caused e.g. by a non-uniform background. One solution here is to take into account or eliminate  
913 non-uniform background by estimating it from individual images or from the entire image  
914 sequence<sup>95</sup>. Another common issue in 3D SMLM with engineered PSFs are aberrations due to  
915 refractive index mismatch between sample and oil, which can cause distortions along the axial  
916 dimension. Such distortions can be detected and prevented by careful calibration, typically by  
917 imaging fluorescent markers at known axial positions in the sample and adjusting the PSF model  
918 to fit them (**Box 4**)<sup>102,203,204</sup>.

919 Another, much more fundamental and often overlooked localization bias stems from the fact that  
920 the PSF can depend on the orientation of the molecule's dipole, which is generally unknown. If  
921 the dipole remains fixed or constrained to certain angles during exposure time, ignoring dipole  
922 orientation can bias estimated positions by up to ~125 nm<sup>205</sup>. Recent work has shown that  
923 molecular positions and dipole orientations can be simultaneously estimated in advanced setups  
924 that feature polarizers and multiple cameras<sup>206</sup>. With standard SMLM systems, localization  
925 artifacts can fortunately still be avoided using fluorescent labels that rotate rapidly during the  
926 exposure time, such that all possible angles are equally sampled and biases are averaged out<sup>206</sup>.

927 A very different type of artifact are unspecific detections that can arise from autofluorescence or  
928 impurities on the coverslip. Autofluorescence is stronger at shorter wavelengths, and can hence  
929 be alleviated using longer wavelength (redder) fluorophores and/or appropriate filters. Impurities  
930 can be reduced, though not entirely removed, by appropriate cleaning of coverslips, e.g. plasma  
931 cleaners<sup>207</sup> (**Table 3**).

## 932 **[H2] Limitations for imaging tissues**

933 Applying SMLM to tissues poses several challenges, some of which can be addressed by adapted  
934 sample preparation. A first challenge is fluorescent labeling. Tissues are thicker than cells and  
935 must be sufficiently permeabilized to be labelled properly. However, extensive permeabilization  
936 can compromise tissue structure. Additionally, fixed thick tissues are more likely to have  
937 background fluorescence and increased light scattering. One way to overcome the increased  
938 background/scattering problem is to cut tissues into thin slices and reconstruct a 3D SMLM image  
939 from many slices<sup>208</sup>. Cutting thin tissue slices often requires paraffin embedding of the tissue,  
940 which can make epitopes unavailable for antibody binding and can decrease labeling efficiency.  
941 Antibody labeling prior to embedding and using specific resins for the embedding step such as  
942 epoxy-resin can overcome this problem and also maintain high photon output of fluorophores<sup>208</sup>.  
943 Another solution to the fluorescent background problem is tissue-clearing<sup>209 210</sup>, which together  
944 with other optimizations allowed to image high-resolution chromatin using *d*STORM in  
945 pathological tissue relevant for cancer diagnosis<sup>210</sup>. In this context, *d*STORM was also shown to  
946 be applicable to samples obtained by scalpel excision from tumor tissue<sup>211</sup>. Finally, SMLM puts  
947 additional demands on the way tissue samples are mounted, since sample drift must be avoided  
948 and specialized aqueous imaging buffers are required. To overcome this challenge, an imaging  
949 chamber was developed<sup>209</sup>, consisting of a permeable agarose pad and a custom-built stainless  
950 steel imaging adapter to keep tissue slices flat, immobile and bathed in imaging buffer during  
951 image acquisition.

952 Optical systems adapted to imaging thick samples and tissue without slicing will be discussed in  
953 the 'Outlook' section.

## 954 **[H2] Throughput limitations**

955 A major limitation of SMLM techniques is their limited throughput, i.e. the low number of cells  
956 imaged per unit time, which results from a relatively small FOV, and the fact that it typically takes  
957 minutes or more to obtain a high quality super-resolution image of a single animal cell. This  
958 severely restricts the ability of SMLM to image large areas or tissue volumes or to reveal rare  
959 cellular phenotypes. Furthermore, SMLM approaches are typically limited to a few colors because  
960 of the small number of spectrally distinguishable fluorophores. Nevertheless, several efforts have  
961 been deployed to address these limitations:

### 962 **[H3] Larger fields of view**

963 Initial SMLM studies were often restricted to a FOV of, say  $\sim 25 \times 25 \mu\text{m}$ , because they relied on  
964 EMCCD cameras with  $512 \times 512$  pixel arrays, and because non-uniform laser illumination typically  
965 results in spatially varying photoswitching and photon emission rates, therefore requiring cropping  
966 of images to the central region of this array, where illumination is approximately constant. Much  
967 larger FOV can now be obtained using sCMOS cameras with bigger arrays ( $2024 \times 2024$  pixels)  
968 and methods to homogenize illumination (flat-fielding)<sup>212-214</sup>. For example, a low-cost microlens  
969 array (MLA)-based epi-illumination system -flat illumination for field-independent imaging (FIFI)  
970 increased the FOV to  $100 \times 100 \mu\text{m}^2$ <sup>213</sup>, hence allowing to image  $\sim 2$ -5 mammalian cells  
971 simultaneously with high resolution.

### 972 **[H3] Multiplexing**

973 Several multiplexing approaches have been developed to image more than a few molecular  
974 species in the same sample<sup>215,216</sup>. DNA-PAINT is particularly amenable to multiplexing because  
975 DNA sequences provide exquisite programmability and specificity. In Exchange-PAINT<sup>216</sup>,  
976 different molecular targets are simultaneously labeled with orthogonal DNA docking strands,  
977 followed by sequential delivery, imaging, and washing steps using complementary imager strands  
978 (**Fig. 6e,f**). Importantly, each imager species can carry the same dye, since target identity is  
979 encoded by the respective sequence and imaging round as opposed to the dye color<sup>217</sup>. Similar  
980 approaches can also be used with sequential labeling of proteins by different primary antibodies,  
981 using the same dye-conjugated secondary antibodies. For example, maS<sup>3</sup>TORM (multiplexed  
982 automated serial staining stochastic optical reconstruction microscopy) enabled SMLM of 15  
983 target proteins in single cells<sup>215</sup>.

984 To increase throughput in multiplexed DNA-PAINT, target molecules can furthermore be  
985 engineered to blink with precisely adjustable frequency and duration, thereby providing a distinct  
986 "kinetic barcode" for the simultaneous detection of hundreds of unique molecular species<sup>218</sup>. In a  
987 related approach, frequency multiplexing DNA-PAINT modulates the excitation lasers at different  
988 frequencies and uses Fourier transformation to unmix the fluorescent response, hence enabling  
989 simultaneous imaging of several fluorophores<sup>219</sup>.

990 Note that highly multiplexed approaches such as MERFISH or seqFISH+ are now increasingly  
991 used to visualize thousands of distinct RNA species or DNA-loci in single cells. Although they rely  
992 on sequential labeling rather than photoswitching, these methods enable super-resolution views  
993 into 3D genome structure and cellular transcriptome. For more information, see refs.<sup>146,220</sup>.

### 994 **[H3] Automation**

995 To perform high throughput or multiplexed imaging for more than a few conditions or target  
996 proteins, one needs a fully automated microscope solution that allows fluid exchange, can perform  
997 staining, sample positioning and image acquisition. The automation problem is being addressed  
998 through several recent developments. Combining high-content screening concepts with SMLM  
999 through an automated microscope and automated data analysis, (HCS)–SMLM enabled 3D  
1000 imaging of an entire 96-well plate<sup>221</sup>. The fluid exchange problem was tackled using a fluidics  
1001 system composed of low cost Lego hardware controlled by ImageJ software<sup>222</sup>. The above-  
1002 mentioned maS<sup>3</sup>TORM used a fully automated and coordinated 3D SMLM microscope with a  
1003 pipetting robot to perform staining experiments *in situ*<sup>215</sup>. An example biological application of  
1004 automated SMLM image acquisition and analysis (though not with automated staining) is the  
1005 study of 23 proteins involved in yeast endocytosis<sup>87</sup>.

### 1006 **[H3] Faster SMLM**

1007 Increasing FOV improves throughput, but not the speed and temporal resolution of SMLM, which  
1008 typically remain poor. Nevertheless, tremendous progress in optimizing the speed of SMLM has  
1009 been made since the first PALM study, which required ~2-12 h for a single FOV. Using sCMOS  
1010 cameras with high (>1 kHz) frame rates and synthetic dyes, the rate of localization can be  
1011 dramatically increased, although this requires high laser powers (>50 kW cm<sup>-2</sup>) to maintain good  
1012 SNR and localization precision<sup>25,223</sup>. Such optimizations allowed for example 2-color 3D SMLM of  
1013 more than 10,000 mammalian cells in ~26 hours<sup>224</sup>.

1014 DNA-PAINT has traditionally been a particularly slow SMLM technique. The influx rate of dye-  
1015 labeled imagers to their targets, which ultimately determines the achievable acquisition speed, is  
1016 limited by the overall DNA association rate  $k_{on}$  ( $\sim 10^6$  (Ms)<sup>-1</sup>), leading to a blinking event every  
1017 100 s for typical imager concentrations of 10 nM) and the imager concentration. While increasing  
1018 the imager concentration can in principle speed-up DNA-PAINT, concentrations in excess of a  
1019 few tens of nM would increase background fluorescence, hence reduce SNR and reduce  
1020 precision. To address this, FRET-based approaches have been implemented<sup>225-227</sup>, effectively  
1021 suppressing fluorescence from diffusing imager strands. Orthogonal approaches aim at  
1022 increasing  $k_{on}$ . This can be done by rational sequence design and buffer optimizations, leading  
1023 to an order of magnitude faster  $k_{on}$  and thus imaging speed<sup>228</sup>. Another approach to increase  $k_{on}$   
1024 is based on preloading DNA-PAINT imager strands with Argonaute proteins<sup>229</sup>. The latest  
1025 development is the use of periodic, concatenated sequence motifs of rationally designed  
1026 sequences, which now speeds up DNA-PAINT by 100-fold over the classical implementation<sup>230</sup>.

### 1027 **[H3] Cheaper SMLM**

1028 Although the cost of SMLM hardware, especially custom-built setups, is moderate compared to  
1029 other advanced microscopy systems, typical systems still have price tags on the order of  
1030 ~100,000 € or more. However, efforts to replace expensive components by cheaper alternatives  
1031 (e.g. EMCCDs by sCMOS cameras or scientific grade lasers by LEDs) and/or leverage  
1032 smartphone technology have resulted in prototypes ~10 k€ or less<sup>77,231-233</sup>. Although they do not  
1033 always achieve the spatial resolutions of more sophisticated microscopes, such approaches may  
1034 prove sufficient for many applications and could also enable large-scale parallelization and hence  
1035 gains in throughput.

## 1036 **[H2] Structural dynamics limitations**

1037 Perhaps the most severe limitation of standard SMLM is its restricted applicability to study  
1038 structural dynamics in live cells. Live-cell structural studies are rare, because collecting enough  
1039 localizations to provide a super-resolution snapshot of a biological structure before it rearranges  
1040 is generally challenging it not impossible. While the above speed optimizations with high frame  
1041 rates are applicable to fixed cells, the intense laser excitation required for fast turnover is much  
1042 more problematic for live cells because of its adverse effects on cell physiology (phototoxicity),  
1043 especially when using UV activation<sup>34</sup>, and rapid photobleaching. Because of these constraints,  
1044 structural SMLM studies have for the most part been limited to technical proofs of principle or to  
1045 relatively slowly moving structures with few reconstructed snapshots<sup>34,85,90,223</sup>. As discussed  
1046 above, methods designed for higher activation densities can overcome this limitation to some  
1047 extent, but at the cost of a significant reduction in spatial resolution.

## 1048 **[H1] Outlook**

1049 We conclude this Primer with a look at advanced SMLM techniques and particularly promising  
1050 ongoing developments that aim to address some of the main remaining challenges in SMLM.  
1051 These include: imaging the ultrastructural context, moving towards truly molecular resolution,  
1052 imaging thick samples and tissues, imaging live samples without phototoxicity or photobleaching  
1053 and more.  
1054

## 1055 **[H3] SMLM with light sheets**

1056 To overcome the challenges of imaging deep inside thick tissue, SMLM was combined  
1057 with light sheet fluorescence microscopy (LSFM) for imaging live<sup>234</sup> and fixed tissues<sup>89</sup>. In LSFM,  
1058 the sample is illuminated with a thin light sheet perpendicular to the optical axis<sup>235</sup>. This optical  
1059 sectioning is advantageous for living tissues, as they experience much reduced irradiation and  
1060 hence less stress during imaging, but also for fixed tissues, as background fluorescence is  
1061 significantly reduced and contrast is improved. In individual molecule localization-selective plane  
1062 illumination microscopy (IML-SPIM), a cylindrical lens is used to create activation and readout  
1063 light sheets to photoactivate single fluorescent molecules in thick tissue<sup>234</sup>. More recently, lattice  
1064 light sheet (LLS) microscopy was combined with 3D dSTORM for plasma membrane receptor

1065 imaging on the basal and apical membrane as well as for 3D single-particle tracking<sup>236</sup> and tissue  
1066 imaging by PAINT using newly developed membrane probes<sup>89</sup>, achieving multi-color super  
1067 resolution imaging of samples up to 20  $\mu\text{m}$  thick and whole-cell 3D SMLM of intracellular  
1068 membranes. The contrast achieved with this approach resembles that achieved with heavy metal-  
1069 stained EM images, without mechanical sectioning. Light sheet SMLM can further be combined  
1070 with Adaptive Optics (AO) to correct for PSF aberrations induced by the scattering tissue to  
1071 improve the imaging depth and spatial resolution when imaging thick samples<sup>237</sup>.

## 1072 [H2] Combining electron microscopy and SMLM

1073 Electron microscopy (EM) generally offers even better spatial resolution than SMLM, and also  
1074 provides a global view of the cellular ultrastructure that SMLM does not. Conversely, EM lacks  
1075 the molecular specificity afforded by fluorescence. Super-resolution visualization of specific  
1076 molecules within an ultrastructural context is possible by combining EM with SMLM on the same  
1077 sample (Correlative light and electron microscopy; CLEM). For example, combining platinum  
1078 replica electron microscopy (PREM) (a technique where the sample is coated by a heavy metal  
1079 to increase its contrast by EM), with iPALM and STORM, provided important details about the  
1080 distinct structural zones inside clathrin-coated structures<sup>238,239</sup>. Similarly, SMLM and PREM  
1081 allowed to show that actin rings found in neurons consist of long, intertwined actin filaments,  
1082 revealing an unexpected braid-like organization of actin rings<sup>240</sup>. Correlative cryogenic SMLM  
1083 (cryo-SMLM) and electron tomography was demonstrated to study the subcellular localization of  
1084 important regulatory proteins in *Caulobacter crescentus*<sup>241</sup>. In a recent tour de force, fluorescently  
1085 labeled high-pressure frozen cells were preserved in vitreous ice, imaged with cryo-SMLM and  
1086 subsequently with 3D focused ion beam scanning electron microscopy (FIB-SEM), and the  
1087 images resulting from the two modalities were registered to nanoscale precision. This approach  
1088 achieved  $\sim 40\text{nm}$  resolution visualization of protein distribution within frozen whole cells in 3D in  
1089 the context of their ultrastructure<sup>242</sup> and revealed unexpected relationships between different  
1090 cellular compartments, such as the existence of ER proteins inside the nucleus. These methods,  
1091 while requiring challenging sample preservation and preparation, nonetheless hold great promise  
1092 for visualizing various molecular complexes in their ultrastructural context.

## 1093 [H2] SMLM with opposing objectives

1094 Because localization precision critically depends on the SNR, one way to improve resolution is to  
1095 collect more photons from single fluorophores. This can be done using two opposing objectives  
1096 (4 Pi setups) that collect twice as many photons from single fluorophores as single objective  
1097 systems, thus improving localization precision by a factor  $\sim\sqrt{2}$ . Such systems enabled lateral  
1098 resolutions  $<10\text{nm}$  and, in combination with astigmatism (**Box 4**) axial resolution  $<20\text{nm}$  in 3D  
1099 STORM, allowing to distinguish individual actin filaments and to visualize two distinct layers of  
1100 actin networks that showed sheet-like protrusions<sup>243</sup>. Interferometric PALM (iPALM)<sup>244</sup> also uses  
1101 two opposing objectives, but allows laser beams to interfere in a three-way beam splitter and  
1102 propagate to 3 CCD cameras, allowing to determine the 3 coordinates of fluorescent molecules.  
1103 In contrast to PSF shaping or multi-plane systems (see **Box 4**), iPALM does not trade off  
1104 localization precision for axial range and achieved isotropic  $<20\text{ nm}$  3D resolution with fluorescent

1105 proteins. More recently, interferometric SMLM has been extended to achieve 10-20 nm resolution  
1106 imaging of the ER, mitochondria, NPCs, bacteriophages and other structures in whole mammalian  
1107 cells without compromising resolution<sup>245</sup>. Careful calibration of refractive index variations will be  
1108 needed to extend this approach to whole nuclei.  
1109

## 1110 [H2] SMLM with minimum fluxes

1111 Since the onset of SMLM, the dominant paradigm to increase localization precision has been to  
1112 collect more photons from single fluorophores, as in the methods above. This paradigm has  
1113 meanwhile been shifted by the introduction of MINFLUX<sup>246</sup>, a concept for localizing single emitters  
1114 not by their highest intensity, but by lowest emission fluxes arising from a local minimum in  
1115 excitation. In the original implementation, an excitation doughnut in combination with a three-  
1116 point-estimator was used to precisely determine the emitter position (**Fig. 7a**). In combination with  
1117 photoswitching, MINFLUX attains single nanometer resolution with considerably reduced photon  
1118 counts compared to standard SMLM (**Fig. 7b**). This allows for very high localization precisions,  
1119 even with relatively dim FPs, and >100-fold faster single molecule tracking than previous  
1120 methods<sup>246</sup>.

1121 Recently, two independent groups have replaced the excitation doughnut by a standing  
1122 wave to spatially modulate excitation intensities, either using diffraction gratings (SIMFLUX<sup>247</sup>) or  
1123 optical interference (Repetitive Optical Selective Exposure or ROSE<sup>248</sup>). In both implementations,  
1124 localization precision is improved by ~2-fold compared to standard SMLM. While MINFLUX can  
1125 theoretically achieve arbitrarily high localization precision, SIMFLUX and ROSE possess the  
1126 advantage that image acquisition times do not scale with FOV, thus currently offer faster  
1127 acquisition speed.

1128 With further advancements (e.g. 3D, multicolor, live cell imaging)<sup>249</sup> and simplification to  
1129 hardware and software, these methods are poised to set a new standard for molecular-resolution  
1130 SMLM.

## 1131 [H2] SMLM in expanded samples

1132 Whereas almost all super-resolution methods aim to diminish the size of the effective  
1133 PSF<sup>2</sup>, expansion microscopy (ExM) takes an entirely orthogonal approach and improves  
1134 resolution by physically expanding a sample embedded in a polyelectrolyte hydrogel<sup>250</sup> (**Fig. 7c**).  
1135 Although ExM can achieve super-resolution with conventional microscopes (e.g. 70 nm resolution  
1136 with five-fold expansion<sup>250</sup> or 25 nm with 20-fold expansion<sup>251</sup>), combining it with SMLM can  
1137 potentially improve resolution down to single nanometers. An important challenge is that many of  
1138 the targeted molecules can lose their label after free-radical polymerization of the hydrogel,  
1139 compromising labeling density and resolution<sup>252</sup>. Furthermore, addition of photoswitching buffer  
1140 as required for dSTORM leads to shrinking of polyelectrolyte hydrogels. Finally, expansion of  
1141 prelabelled samples results in further displacement of the fluorophore from the target molecule,  
1142 increasing the linkage error, e.g. from 17.5 nm with indirect immunostaining to 70 nm after 4-fold  
1143 expansion, again severely limiting the resolution. Recently, trifunctional linkers have been  
1144 developed that are inert to polymerization, digestion and denaturation, and enable direct labeling  
1145 and covalent linking of target molecules and functional groups to the hydrogel<sup>253,254</sup>. Furthermore,

1146 it was shown that re-embedding of the expanded hydrogel prevents shrinking and post-expansion  
1147 labeling preserves the ultrastructure of multiprotein complexes, improves the labeling efficiency  
1148 and reduces the linkage error from 17.5 nm to ~5 nm for 3.2-fold expansion<sup>255</sup>. The potential of  
1149 these new methods has been demonstrated by imaging of clathrin-coated pits, microtubules and  
1150 centrioles with ~5 nm resolution<sup>255 254</sup> (**Fig. 7d**). Ex-SMLM thus provides another promising road  
1151 map for achieving true molecular resolution.

## 1152 **[H2] Enhanced SMLM with deep learning**

1153 The increasingly complex imaging data acquired thanks to advances in SMLM exacerbate the  
1154 demand for computational analysis. In recent years, the field of computer vision has been  
1155 revolutionized by machine learning methods based on multi-layer artificial neural networks (deep  
1156 learning)<sup>256</sup>. Unsurprisingly, deep learning is now also adapted to advance light microscopy  
1157 methods, including SMLM<sup>257</sup>. For example, deep learning has been used to extract single  
1158 molecule localizations from diffraction-limited images, including in high activation density  
1159 conditions, which can dramatically reduce processing time compared to MLE<sup>258</sup>. However, deep  
1160 learning can also help accelerate image acquisition itself by overcoming apparently fundamental  
1161 sampling constraints. This is possible because deep learning can reconstruct high quality images  
1162 from much fewer localizations than traditionally needed<sup>259</sup> by learning structural redundancies  
1163 from similar images (**Fig. 7e**). With further adaptations, such methods might greatly facilitate  
1164 super-resolution in live cells while minimizing phototoxicity, as recently demonstrated for 3D light  
1165 sheet microscopy<sup>260</sup>. Deep learning will certainly also make inroads in the quantitative analysis of  
1166 SMLM data, such as the segmentation of biological features<sup>261,262</sup>.

1167 The power of deep neural networks comes from their ability to learn complex features from  
1168 training data. However this reliance on training data also carries the risk that neural network  
1169 outputs might be biased towards the training data, potentially leading to miss novel phenotypes  
1170 or even to generate artifacts<sup>257,259,263</sup>. This well-known Achilles heel of machine learning therefore  
1171 calls for careful validations and/or retraining of existing deep learning frameworks and the  
1172 development of methods that are aware of or robust to mismatches between testing and training  
1173 data. If these challenges are correctly addressed, machine learning methods will likely play a key  
1174 role in overcoming key limitations of advanced microscopy and SMLM in particular.

1175

## 1176 **[H2] Concluding remarks**

1177 SMLM is a powerful, yet relatively accessible, family of imaging technique that combines  
1178 fluorophore chemistry, optics and computation to image and analyze biological structures and/or  
1179 dynamics at increasingly higher resolution. In this Primer, we attempted to introduce all main basic  
1180 aspects of SMLM, highlighting biological applications that illustrate the maturity of SMLM  
1181 methods, while also covering advanced and promising recent developments. As the SMLM field  
1182 continues to evolve, it brings us nearer to a future where all molecules within a cell, tissue or  
1183 organism may be individually localized, counted and tracked. We hope that this Primer will  
1184 encourage more investigators to adopt and further improve SMLM to explore the innermost  
1185 architecture and mechanisms of living systems.

1186  
1187  
1188

1189 **TABLES**

1190

1191 **Table 1: Selected commercial reagents for SMLM experiments**

1192 This table lists examples of some recommended reagents for newcomers to SMLM. For multi-color imaging,  
 1193 see **Box 2**. For more comprehensive information and/or systematic comparisons of SMLM labeling  
 1194 techniques, see e.g. <sup>35,36,60,264,265</sup> and the protocols listed in **Table 3**.

Type of reagent	Reagent(s)	Supplier	Reference	Application
Primary antibodies, unlabeled (use with labeled secondary antibodies)	Rat anti-tubulin antibody (recognizes the $\alpha$ subunit of tubulin)	Bio-Rad	<a href="#">link</a>	(d)STORM of microtubules
	Rabbit anti-nucleoporin Nup133	Abcam	<a href="#">link</a>	(d)STORM of nuclear pores in human cells
Secondary antibodies conjugated to synthetic dyes (use with unlabeled primary antibodies)	Anti-rat antibody coupled to Alexa Fluor 647	ThermoFisher	<a href="#">link</a>	dSTORM
	Anti-rabbit antibody coupled to Alexa Fluor 647	Jackson ImmunoResearch	<a href="#">link</a>	dSTORM
Fluorescent protein plasmids	mEos3.2 plasmid	Addgene	<a href="#">link</a>	(F)PALM
	mMaple3 plasmid	Addgene	<a href="#">link</a>	(F)PALM
DNA-PAINT kits	DNA-conjugated secondary antibodies/nanobodies (docking strands)	Massive Photonics	<a href="#">link</a>	DNA-PAINT
	Dye-conjugated DNA (imager strands)	Massive Photonics	<a href="#">link</a>	DNA-PAINT
Direct labeling	Phalloidin conjugated to Alex Fluor 647	ThermoFisher	<a href="#">link</a>	dSTORM of actin
	MitoTracker Red	ThermoFisher	<a href="#">link</a>	Live cell STORM of mitochondrial membranes
Photoswitching buffers	SAFe Reagents	Abbelight	<a href="#">link</a>	(d)STORM
	Everspark	idylle	<a href="#">link</a>	(d)STORM
Labeled samples	Cells with labeled microtubules, mitochondria, podosomes..	Abbelight	<a href="#">link</a>	(d)STORM
Fiducial markers	TetraSpeck microspheres (100 nm diameter)	ThermoFisher	<a href="#">link</a>	Correction of drift and/or chromatic aberrations

1195

1196 **Table 2: Selected SMLM software**

1197 This table lists a few recommended software packages for SMLM image reconstruction. All listed software  
1198 are free, can reconstruct 3D SMLM images and all except SMAP enable drift correction. This selection is  
1199 partly subjective, as it is based on software known to (and in part developed by the authors), but also based  
1200 on objective results from the 2D/3D SMLM localization challenges. For more details and quantitative  
1201 comparisons of these and many other SMLM software (currently 95), we refer to the challenges and their  
1202 updates (<http://bigwww.epfl.ch/smlm>).

Software name	URL	Comments	Reference
ThunderSTORM	<a href="https://zitmen.github.io/thunderstorm/">https://zitmen.github.io/thunderstorm/</a>	Widely used, implements multiple 2D and 3D algorithms. Strong performance in 2D SMLM challenge	94
SMAP	<a href="https://github.com/jries/SMAP">https://github.com/jries/SMAP</a>	Handles arbitrary PSFs; Strong performance in 3D SMLM challenge	266,267
SMOImolphot	<a href="https://bitbucket.org/ardiloot/smolphot-software/wiki/Home">https://bitbucket.org/ardiloot/smolphot-software/wiki/Home</a>	Strong performance in 3D SMLM challenge	NA
ZOLA-3D	<a href="https://github.com/imodpasteur/ZOLA-3D">https://github.com/imodpasteur/ZOLA-3D</a>	Handles arbitrary PSFs and refractive index mismatch	102
Picasso	<a href="https://github.com/jungmannlab/picasso">https://github.com/jungmannlab/picasso</a>	Software package optimized for DNA-PAINT	19

1203

1204

1205

1206 **Table 3: Selected experimental protocols for SMLM**

1207 The following is a non exhaustive list of some recommended experimental protocols for SMLM.

- 1208 • Van de Linde et al. (ref. <sup>27</sup>) : *d*STORM, live cells.
- 1209 • Gould et al. (ref. <sup>202</sup>) : (F)PALM.
- 1210 • Schnitzbauer et al. (ref. <sup>19</sup>): DNA-PAINT, multicolor, quantification (qPAINT).
- 1211 • Jimenez et al. (ref. <sup>268</sup>): *d*STORM, DNA-PAINT, multicolor, optimized sample preparation.
- 1212 • Manley et al. (ref. <sup>269</sup>): spt-PALM.
- 1213 • Kaplan et al. (ref. <sup>270</sup>): sample preparation optimized for *d*STORM in yeast.
- 1214 • Davis et al. (ref. <sup>207</sup>): how to prepare coverslips to minimize impurities in SMLM

1215

1216

1217

1218

1219 **FIGURE LEGENDS**

1220

1221 **Figure 1: Principle of SMLM.**

1222 **a)** A single fluorescent molecule (green dot) imaged through a microscope appears on the camera  
1223 as a fuzzy, ~200 nm wide spot (the PSF) extending over multiple pixels. **b)** PSFs from  
1224 simultaneously emitting molecules overlap if their distances are smaller than the PSF. **c)** The  
1225  $(X_0, Y_0)$  coordinates of a single molecule can be computed with high precision, because subpixel  
1226 displacements (e.g. here by 0.5 pixels in X and Y) lead to predictable changes in pixel values, as  
1227 shown by the grey scale image (bottom) and corresponding 2D histogram (center) (simulated  
1228 data). The mesh surface shows a Gaussian model PSF centered on  $(X_0, Y_0)$ . **d)** Higher photon  
1229 counts (N) lead to higher SNR images and more precise localizations (red crosses). **e)** SMLM  
1230 usually exploits the fact that fluorophores stochastically switch between an active ('ON') state and  
1231 one or more inactive ('OFF') states. **f)** A diffraction-limited image of nuclear pores, with all  
1232 fluorophores ON, is blurred by overlapping PSFs. **g)** A sequence of diffraction-limited images of  
1233 the same area, where only few molecules are ON simultaneously. **h,i)** In each frame, single  
1234 molecules are computationally detected (**h**) and localized (**i**). Molecules at the border of the image  
1235 are not detected. **j)** An SMLM experiment results in a localization table, where each row  
1236 represents a distinct localization event and columns indicate x, y coordinates and additional  
1237 information, e.g. frame number and photon counts (N). There are usually multiple localizations  
1238 per frame, and the same molecule can be localized in multiple frames. **k,l)** Accumulated  
1239 localizations visualized as a scatter plot (**k**), or a 2D histogram (**l**), with bins much smaller than  
1240 raw image pixels. The raw image pixels are shown by the dashed grid, and 10x10 small bins are  
1241 shown inside a single raw image pixel in **k**). This 'super-resolution' image reveals the ring-like  
1242 (octagonal) structure of nuclear pores that was previously hidden.

1243

1244 **Figure 2: Fluorophore types and labeling strategies in SMLM.**

1245 **a-e)** Fluorophores compatible with SMLM can be divided into five classes: photoswitchable (**a**),  
1246 photoactivatable (**b**), photoconvertible (**c**), spontaneously blinking (**d**), or temporarily binding (**e**).  
1247 The boxes indicate properties of fluorophores in each class and an example fluorophore. The  
1248 schematic involving the lambda symbol indicates the nature of switching that enables SMLM. **f)**  
1249 Comparison of different fluorescent labeling approaches and the resulting linkage error, i.e. the  
1250 distance between the molecular target of interest (here, tubulin) and the fluorophore. From left to  
1251 right: immunolabeling with primary and secondary antibodies (orange); labeling with a small  
1252 camelid antibody (nanobody, yellow), often in combination with primary antibodies or GFP  
1253 (green); labeling with a genetically encoded protein such as Eos (magenta) or a self-labeling  
1254 protein tag; direct labeling with a dye-conjugated ligand such as the microtubule-binding  
1255 compound docetaxel (turquoise box); incorporation of unnatural amino acids such as TCO\*-lysine  
1256 (blue box) via genetic code expansion (GCE) enables rapid labeling with functionalized synthetic  
1257 dyes. Structure of immunoglobulin (PDB-ID 1IGT), green fluorescent protein bound to enhancer  
1258 nanobody (PDB-ID 3K1K), EOS-FP (mEos2, PDB-ID 3S05), exemplified target protein (tubulin,  
1259 PDB-ID 1FFX).

1260

1261 **Figure 3: SMLM Hardware.**

1262 **a,b)** A basic SMLM setup consists of illumination (laser, Köhler lens, i); imaging optics and stage  
1263 (objective, sample, ii) and detection (tube lens, camera, iii). Dichroic mirrors are used to separate  
1264 excitation and emission wavelengths, and can be combined with additional emission filters to  
1265 reject autofluorescence. **c)** A 2D *d*STORM image of microtubules. **d)** A 3D SMLM system can be  
1266 obtained simply by adding an optical component to engineer the PSF, such as a cylindrical lens,  
1267 which generates astigmatism. **e)** A z-stack of a fluorescent bead shows the axial variations of an  
1268 astigmatic PSF. **f)** A 3D super-resolution image obtained by analysis of 2D single molecule  
1269 images, displayed here in 2D with color indicating z. Here, PSF calibration and image  
1270 reconstruction was performed with ZOLA-3D<sup>102</sup>.

1271

#### 1272 **Figure 4: Live cell SMLM**

1273 **a)** Structural dynamics of a focal adhesion (tdEos-paxillin) reveal its appearance near the cell  
1274 edge before maturation and motion toward the interior. Each super-resolution image is  
1275 reconstructed from 1,000 raw frames. Scale bar: 500 nm. From ref. <sup>34</sup>. **b)** Molecular dynamics of  
1276 the vesicular stomatitis virus glycoprotein (VSVG-tdEos), a transmembrane protein freely  
1277 diffusing on the plasma membrane. The motion of each protein is traced over multiple frames,  
1278 with different colors representing individual molecules (left). Each trajectory can be analysed, to  
1279 create a map of diffusion coefficients (center). In contrast, the dynamics of molecules within the  
1280 actin cytoskeleton (actin-tdEos) show directed motion near the cell's leading edge and diffusive  
1281 motion toward the interior (right). Scale bars: 500 nm. From ref. <sup>16</sup>.

1282

#### 1283 **Figure 5. Major discoveries enabled by SMLM**

1284 **a)** STORM image of histone H2B in human fibroblast cells (hFb) with progressively higher zoomed  
1285 insets, adapted from ref.<sup>139</sup>. Scale bars: 2  $\mu$ m and 500 nm. **b)** Top: *d*STORM image of nuclear  
1286 pore complexes (NPCs) labeled with antibodies against the nucleoporin Nup133. Three individual  
1287 NPCs are shown on the right and an average image of 4,171 aligned NPCs on the lower right.  
1288 Scale bars: 0.5  $\mu$ m and 0.1  $\mu$ m. Bottom: Left: Colored circles show radial positions of different  
1289 nucleoporins in the plane of the nuclear envelope, determined from averaged images, with the  
1290 inferred position of the Y-shaped scaffold complex overlaid. Circle thickness reflects 95%  
1291 confidence intervals of average radial distances. Center and right: side and frontal views of the  
1292 EM structure (grey), with the radial positions of nucleoporins shown in color, and two positions of  
1293 the Y complex consistent with the data overlaid. Scale bar, 40 nm. From ref.<sup>120</sup>. **c)** iPALM image  
1294 of a human U2OS cell expressing integrin  $\alpha_v$ -tdEos (left) and actin-mEos2 (right) with color coded  
1295 zoomed insets of boxed regions adapted from<sup>169</sup>. Colors represent the z-position relative to the  
1296 substrate ( $z=0$  nm). Scale bars: 500 nm. **d)** 3D STORM image of actin in a neuronal axon with  
1297 zoomed y/z insets of boxed regions showing actin rings, adapted from<sup>58</sup>. Scale bars: 1  $\mu$ m and  
1298 200 nm.

1299

#### 1300 **Figure 6: Limitations and optimizations**

1301 **a)** SMLM image of microtubules before and after drift correction. Arrows show a fluorescent bead  
1302 used to estimate the drift. **b,c)** Artifacts due to PSF overlaps in simulated images. **b)** Left: ground  
1303 truth image without localization errors, shown as a scatter plot. Middle: SMLM image for a low  
1304 density of activated fluorophores (10 localizations per  $\mu$ m<sup>2</sup>, no PSF overlaps). Right: the same,  
1305 for a high activation density (50 localizations per  $\mu$ m<sup>2</sup>); overlapping PSFs cause artifactual

1306 localizations near the center. **c)** Simulated molecular clusters, with a 10-fold higher density for the  
1307 top cluster. Left: simulated ground truth shown as scatter plot. Middle: SMLM image without  
1308 filtering. Right: the same after filtering of poor localizations due to overlapping PSFs. After filtering,  
1309 the high density cluster is barely visible. **d)** Artifacts in SMLM images of microtubules resulting  
1310 from subpixel localization bias. Top: without bias. Bottom: with bias; the bias is due to  
1311 computational localization with an incorrect PSF model. As a result of bias, the reconstructed  
1312 image shows a grid pattern. Insets show the entire FoV. The localization bias is readily apparent  
1313 in the histogram of  $x$  coordinates relative to the center of pixels in the raw images (drift correction  
1314 was not applied to better highlight the effect of localization bias). **e)** Exchange-PAINT implements  
1315 sequential imaging of multiple targets by DNA-PAINT with different imager strands labeled with  
1316 the same dye. The sample is first labeled with orthogonal docking strands  $P_1, P_2, \dots, P_n$ , then the  
1317 first imager strand species  $P^*_1$ , complementary to docking strand  $P_1$ , is introduced and a DNA-  
1318 PAINT image of  $P_1$  is acquired. Next, the strands  $P^*_1$  are washed out, then imager strands  $P^*_2$   
1319 are introduced and a DNA-PAINT image of  $P_2$  is acquired, etc. for  $n$  cycles. Each DNA-PAINT  
1320 image is assigned a distinct pseudocolor and all  $n$  images are then superposed. **f)** Pseudocolor  
1321 DNA-PAINT images of origami structures displaying digits 0–9. Scale bar: 25 nm.

1322  
1323

### 1324 **Figure 7: New directions in SMLM**

1325 **a,b)** MINFLUX. **a)** MINFLUX excitation concept to precisely probe emitter positions by minimal  
1326 photon fluxes. A doughnut-shaped excitation (green) is moved sequentially to four probing  
1327 positions  $r_0, r_1, r_2, r_3$  (colored circles) in the vicinity of a single fluorophore (orange star). The  
1328 probing range is given by  $L$ . If the doughnut center coincided perfectly with the fluorophore  
1329 position, no photons would be emitted. The position of the fluorophore can be calculated with very  
1330 high precision from the fluorescence photon counts shown below. From ref.<sup>246</sup>. **b)** Example  
1331 nuclear pore complex imaged by MINFLUX. Scale bars: 50 nm. From ref.<sup>249</sup> **c,d)** Expansion-  
1332 SMLM. **c)** In expansion microscopy (ExM), samples are embedded in a gel that expands upon  
1333 hydration. Immunolabeling of epitopes can be performed before or after gelation and expansion  
1334 using linkers that bind to the gel and to a fluorophore. Full or partial protein digestion is commonly  
1335 used to enable isotropic expansion. In order to enable (d)STORM imaging in photoswitching  
1336 buffer the sample is re-embedded in an uncharged polyacrylamide gel after expansion. **d)** Left:  
1337 3D post-labeling Ex-dSTORM image of a 3.2x expanded and re-embedded sample shows the  
1338 ninefold symmetry of the procentriole. Scale bar, 500 nm. Right: 3.1-fold expanded and re-  
1339 embedded tubulin filaments. Magnified view of highlighted region (white box). xz side view cross  
1340 section of a tubulin filament showing its hollow structure. Scale bars, 2  $\mu\text{m}$  (large square), 500 nm  
1341 (vertical rectangle), 200 nm (small square). From ref.<sup>255</sup> **e)** Deep learning accelerates SMLM  
1342 image acquisition. A widefield image (WF) and a sparse SMLM image obtained from  $k=300$   
1343 frames only are fed as inputs to an artificial neural network (ANN) that was previously trained on  
1344 high quality (long acquisition) SMLM images of microtubules. The ANN outputs a super-resolution  
1345 image that is in good agreement with an SMLM image obtained from  $k=30,000$  frames ('ground  
1346 truth'), suggesting a 100-fold reduction in acquisition time without compromising spatial resolution.  
1347 Adapted from ref.<sup>259</sup>.

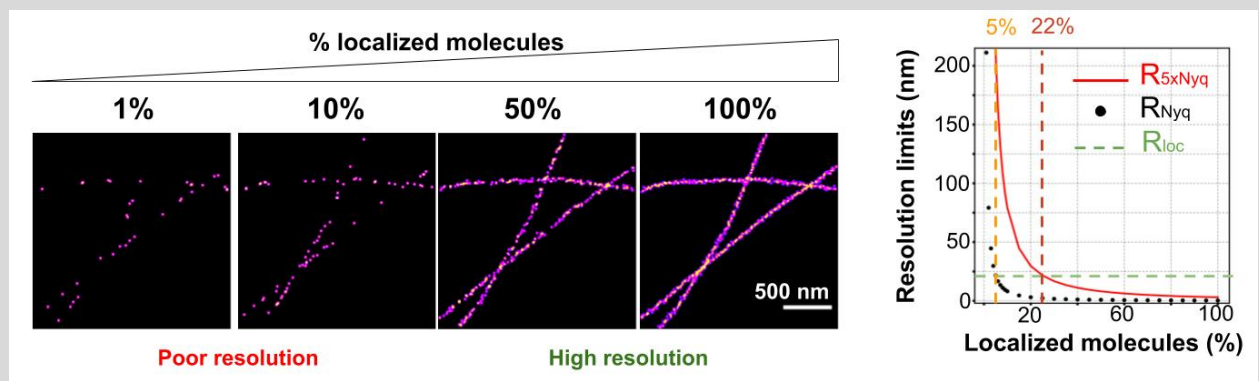
1348

1349 **BOXES**  
1350

1351 **Box 1: The resolution of SMLM images**

1352 Determining the resolution of an SMLM image is not straightforward. The resolution  $R$  cannot be  
1353 better than  $R_{loc} \approx 2.3 \sigma_{loc}$ , thus estimating localization precision  $\sigma_{loc}$  is key. One approach to  
1354 estimate  $\sigma_{loc}$  is to calculate the Cramer-Rao lower bound (CRLB), but this estimate is generally  
1355 too optimistic. More realistic estimates can be obtained from the standard deviations of  
1356 coordinates in small localization clusters likely originating from single molecules. However, both  
1357 estimates ignore potential localization biases or linkage errors. A common alternative is to  
1358 calculate the dispersion of coordinates (e.g. the full width half maximum, or FWHM) across thin  
1359 structures such as cytoskeletal filaments. This provides a conservative upper limit to  $2.3 \sigma_{loc}$ , since  
1360 the FWHM reflects both precision and the width of the labeled structure (including linkage errors).

1361 A critical, but often overlooked requirement to achieving a resolution  $R_{loc} = 2.3 \sigma_{loc}$  is to have a  
1362 good sampling, i.e. a sufficiently high percentage of localized molecules. An early study  
1363 introduced a Nyquist sampling criterion to calculate the sampling limit ( $R_{Nyq}$ ) to resolution based  
1364 on the nearest neighbor distances between localizations<sup>34</sup>, but a reanalysis suggested that 5-fold  
1365 higher sampling ( $R_{5xNyq}$ ) is actually required<sup>89</sup>. In the simulated images below, with  $\sigma_{loc} = 10$  nm,  
1366 this criterion implies that 22% of molecules must be localized to achieve a resolution  $R_{loc} = 23$   
1367 nm. A Fourier Ring Correlation (FRC) criterion<sup>271</sup> — which measures the correlation between  
1368 subsets of localizations — simultaneously accounts for localization precision and sampling, but  
1369 requires a user-defined threshold and can hide spatial variations in resolution. More recently, an  
1370 alternative, threshold-free approach based on phase correlation was proposed<sup>272</sup>.



1371 While useful, such measures are insufficient to rigorously determine the resolution. Compelling  
1372 evidence that an image has resolution  $R$  or better is to clearly distinguish distinct structures at  
1373 distances  $\leq R$ . In biological samples, this is done most convincingly on complexes where  
1374 molecules are located at known distances from each other, such as nuclear pores, which have  
1375 therefore become a gold standard to evaluate resolution<sup>113</sup>.  
1376

1378

**BOX 2: Multicolor SMLM**

1379

1380

1381

1382

1383

1384

The investigation of biomolecular interactions in cells requires super-resolution imaging of multiple target molecules in one experiment. Multicolor SMLM with synthetic dyes can be accomplished using the classical STORM concept with probes that contain both an activator and a reporter fluorophore<sup>8</sup>. Here, various activator-reporter dye pairs attached to an antibody, such as Alexa Fluor 405 & Cy5, Cy2 & Cy5, and Cy3 & Cy5, enable multicolor STORM using three different activation lasers and spectrally-selective activation of the reporter fluorophore Cy5<sup>273</sup>.

1385

1386

1387

1388

1389

Activator-free SMLM with synthetic dyes (*d*STORM) requires fluorophores that exhibit similar blinking efficiency under identical photoswitching buffer conditions. Suitable pairs for two-color *d*STORM include Alexa Fluor 532 & Alexa Fluor 647, ATTO 520 & Alexa Fluor 647, and CF 568 & Alexa Fluor 647, as well as combinations with longer-wavelength absorbing dyes, e.g. DyLight 750<sup>152,274</sup>.

1390

1391

1392

1393

1394

1395

1396

1397

1398

1399

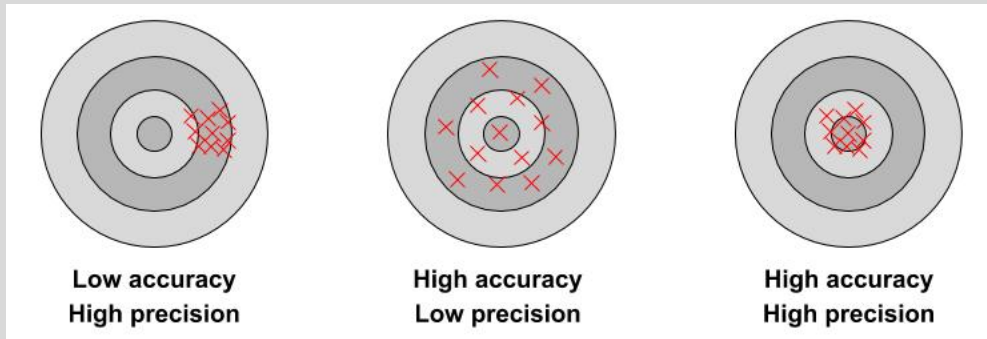
To avoid chromatic aberrations, multicolor SMLM by spectral-demixing can be used. Here, one can use synthetic dyes that exhibit good photoswitching performance in the same thiol switching buffer and can be efficiently excited with the same laser wavelength but exhibit different emission maxima. The emission light is spectrally separated by a dichroic beamsplitter and imaged onto two cameras or separate parts of the same camera chip. The fluorophores are then classified by their emission ratio. Alternatively, the emission signal of different synthetic dyes can be split into two detection paths and recorded simultaneously on two cameras (or two regions of the same camera): one emission spectra recording and one for localization<sup>275-277</sup>. FPs have also been used successfully for multicolor SMLM, either alone, e.g. Dronpa & mEos, or in combination with synthetic fluorophores, e.g. mEos2 & Alexa Fluor 647 or Dronpa & Alexa Fluor 647<sup>177,278</sup>.

1400

1401  
1402  
1403  
1404  
1405  
1406  
1407  
1408  
1409  
1410  
1411  
1412  
1413

### Box 3: Localization precision, accuracy and the Cramer-Rao lower bound

The image  $I$  of a single fluorophore is the result of a stochastic process that depends on several unknown parameters, notably the  $(x, y)$  coordinates of the molecule and the number of collected photons,  $N$ . Localization algorithms attempt to determine  $(x, y)$  from  $I$  and provide estimates  $(\hat{x}, \hat{y})$ . Algorithms are usually assessed based on their mean squared error (MSE):  $MSE(\hat{x}) = \langle (\hat{x} - x)^2 + (\hat{y} - y)^2 \rangle$  where brackets denote statistical averaging. The MSE for coordinate  $x$  can be rewritten:  $MSE(\hat{x}) = Var(\hat{x}) + B^2(\hat{x})$ , where the variance  $Var(\hat{x}) = \langle (\hat{x} - \langle \hat{x} \rangle)^2 \rangle$  is the random component of the errors, while the bias  $B(\hat{x}) = x - \langle \hat{x} \rangle$  is the systematic error (and likewise for  $y$ ). The variance defines the 'precision' of an algorithm, while the bias defines the 'accuracy'. High precision algorithms tend to provide similar coordinates for different images of the same molecule, but these may have a large offset (bias) from the true value. High accuracy algorithms tend to find the correct position on average, but possibly with high dispersion (low precision), implying that individual localizations may still be far from the true location.



1414  
1415  
1416  
1417  
1418  
1419  
1420  
1421  
1422  
1423

One usually considers algorithms without bias, so that  $MSE(\hat{x}) = Var(\hat{x})$ . The Cramer-Rao lower bound (CRLB) provides a lower limit to the variance (and hence precision) of any unbiased algorithm. Assuming for simplicity that the image depends only on  $x$ , the CRLB reads:  $Var(\hat{x}) \geq - \left[ \langle \frac{\partial^2}{\partial x^2} \ln p(I; x) \rangle \right]^{-1}$  where  $p(I; x)$  is the probability of observing  $I$  if the true coordinate is  $x$  ( $p(I; x)$  is also called the likelihood). A handy formula can be derived under strongly idealized conditions, where the point spread function (PSF) is modeled as a Gaussian of standard deviation  $\sigma_0$ , the background and camera noise are neglected, and the exact coordinates of the  $N$  photons hitting the camera is recorded (i.e. ignoring pixelation). Under these assumptions, the CRLB reduces to:  $Var(\hat{x}) \geq \sigma_0^2/N$ , and the precision limit becomes:  $\sigma_{loc} = \sigma(\hat{x}) \geq \sigma_0/\sqrt{N}$ .

1424

1425

### BOX 4: Three-dimensional (3D) SMLM

1426

Biological structures are generally three-dimensional (3D), and should therefore be imaged in 3D with axial resolutions similar to those that can be achieved laterally. Innovations in optical setups exploiting point spread function (PSF) engineering<sup>80,279</sup> or multi-plane<sup>280,281</sup> detection have enabled precise localization of molecules in 3D, in samples up to several micrometers thick<sup>102</sup>.

1427

1428

1429

1430

Methods with engineered PSFs exploit the fact that the 2D image of a fluorescent molecule depends not only on its lateral ( $x, y$ ) coordinates but also on its axial coordinate  $z$ . By analyzing the 2D image pattern, the  $z$  coordinate can be estimated in addition to  $x$  and  $y$ . In this way, 3D super-resolution images can be reconstructed from 2D images obtained without refocusing. The most common approach exploits an astigmatic PSF, generated by inserting a single cylindrical lens into the imaging path<sup>79,80,102</sup> (see Figure). Other PSFs such as double helix (Figure), tetrapod or saddle point, which can be obtained using phase masks, deformable mirrors or other optical devices, can achieve larger axial range<sup>102,279,282,283</sup>.

1431

1432

1433

1434

1435

1436

1437

1438

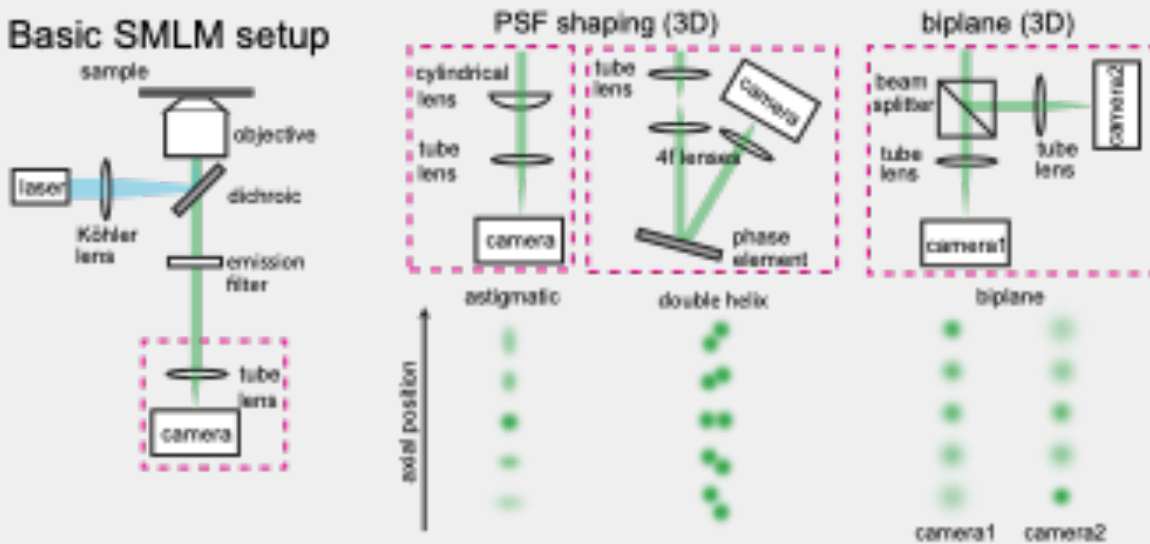
In setups with two or more focal planes (see Figure)<sup>280,281,284</sup>, analyzing the relative intensities in different images of the same molecule also allows to compute  $z$  in addition to ( $x, y$ ). In multifocal microscopy (MFM), a specialized diffractive grating is used to image several (e.g. up to 9) focal planes simultaneously on a single camera<sup>281</sup>. Combining MFM with SMLM allowed fast volumetric imaging of mitochondria in whole cells with high resolution<sup>282</sup>.

1439

1440

1441

1442



1443

PSF shaping or multi-plane detection divert photons for 3D encoding, resulting in a loss of localization precision. The theoretically achievable localization precision and axial range depend on the PSF shape, and can be calculated. Some PSFs have even been engineered to achieve theoretically optimal precisions over a given axial range<sup>99,283</sup>. Many software packages are now available for 3D SMLM with PSF engineering<sup>99</sup>.

1444

1445

1446

1447

1448

1449

1450

## 1451 **Acknowledgements**

1452 M. Lelek and C. Zimmer thank B. Lelandais for excellent comments on the manuscript. Work in  
1453 the Zimmer lab is funded mainly by Institut Pasteur, Fondation pour la Recherche Médicale (grant  
1454 DEQ 20150331762), Région Ile de France, and Agence Nationale de la Recherche. M.  
1455 Lakadamyali acknowledges funding from the National Institutes of Health, National Institutes of  
1456 General Medical Sciences (NIH/NIGMS) under the grant number RO1 GM133842-01. G. Beliu  
1457 and M. Sauer acknowledge funding by the German Research Foundation (DFG, SA829/19-1)  
1458 and the European Regional Development Fund (EFRE project (“Center for Personalized  
1459 Molecular Immunotherapy”). F. Schueder and R. Jungmann acknowledge support by the German  
1460 Research Foundation through the SFB1032 (project A11) and the Max Planck Society. This  
1461 project was supported by the European Union’s H2020 programme under the Marie Skłodowska-  
1462 Curie grant BALTIC (J. Griffié) and ERC Piko (S. Manley).

1463

## 1464 **Competing interests**

1465

1466 Ralf Jungmann is cofounder of Ultivue, Inc. and Massive Photonics GmbH. Christophe Zimmer  
1467 has an ongoing collaboration with Abbelight. All other authors declare no competing interests.

1468

## 1469 **Glossary**

1470

- 1471 • **Diffraction:** bending of light waves at the edges of an obstacle such as an  
1472 aperture.
- 1473
- 1474 • **Point spread function (PSF):** the image of an infinitesimally small light source  
1475 through the optical system.
- 1476
- 1477 • **Airy pattern:** a pattern of light featuring a central bright disk surrounded by  
1478 increasingly dimmer concentric rings formed by diffraction from a circular  
1479 aperture.
- 1480
- 1481 • **Total internal reflection (TIRF):** a configuration in which a strongly inclined  
1482 laser beam is reflected by the coverslip, leaving only a thin (~200 nm) layer from  
1483 the coverslip illuminated, strongly reducing background.
- 1484
- 1485 • **Highly inclined and laminated optical sheet (HILO):** a configuration in which  
1486 the laser beam enters the sample at a sharp angle, allowing to reduce the  
1487 background when imaging at a distance from the coverslip.
- 1488
- 1489 • **Noise:** Random fluctuations of the image pixel values.
- 1490

- 1491
- 1492
- 1493
- 1494
- 1495
- 1496
- 1497
- 1498
- 1499
- 1500
- 1501
- 1502
- 1503
- 1504
- 1505
- 1506
- 1507
- 1508
- 1509
- 1510
- **Poisson noise (shot noise):** A type of statistical noise affecting photon counts and arising from the fact that photons are hitting pixels independently of each other with constant probability per unit time.
  - **Cramer-Rao lower bound (CRLB):** A fundamental limit to the precision (variance) of any estimator without bias.
  - **Ripley's K function:** A function computed from a set of points that helps reveal if points are uniformly randomly distributed or exhibit spatial clustering or dispersion.
  - **Nyquist sampling:** sampling a continuous signal at twice the highest frequency allows to reconstruct it without loss of information.
  - **Fourier ring correlation (FRC):** a measure of image resolution computed from the cross-correlation between two independent noisy versions of the image in Fourier (frequency) space.

1511 **Related links:**

- 1512
- 1513
- 1514
- 1515
- 1516
- 1517
- 1518
- 1519
- 1520
- 1521
- 1522
- 1523
- 1524
- 1525
- 1526
- Single-Molecule Localization Microscopy Software Benchmarking: <http://bigwww.epfl.ch/smlm>
  - Zenodo: an open access repository for research software and data: <https://zenodo.org/>
  - FigShare: <https://figshare.com/> an open access repository for figures, data sets and images
  - Image Data Resource <https://idr.openmicroscopy.org/> a public repository of imaging data

1527

## References:

1528

1529

1530 1 Abbe, E. Beiträge zur Theorie des Mikroskops und der mikroskopischen Wahrnehmung.

1531 *Archiv für Mikroskopische Anatomie* **9**, 413-468, doi:10.1007/BF02956173 (1873).

1532 2 Schermelleh, L. *et al.* Super-resolution microscopy demystified. *Nature Cell Biology* **21**,

1533 72-84, doi:10.1038/s41556-018-0251-8 (2019).

1534 3 Donnert, G. *et al.* Macromolecular-scale resolution in biological fluorescence

1535 microscopy. *Proceedings of the National Academy of Sciences* **103**, 11440-11445,

1536 doi:10.1073/pnas.0604965103 (2006).

1537 4 Gustafsson, M. G. L. Surpassing the lateral resolution limit by a factor of two using

1538 structured illumination microscopy. *J Microsc* **198**, 82-87 (2000).

1539 5 Heintzmann, R., Jovin, T. M. & Cremer, C. Saturated patterned excitation microscopy--a

1540 concept for optical resolution improvement. *J Opt Soc Am A Opt Image Sci Vis* **19**, 1599-

1541 1609 (2002).

1542 6 Betzig, E. *et al.* Imaging intracellular fluorescent proteins at nanometer resolution.

1543 *Science* **313**, 1642-1645 (2006).

1544 7 Hess, S. T., Girirajan, T. P. & Mason, M. D. Ultra-high resolution imaging by

1545 fluorescence photoactivation localization microscopy. *Biophys J* **91**, 4258-4272,

1546 doi:biophysj.106.091116 [pii] 10.1529/biophysj.106.091116 (2006).

1547 8 Rust, M. J., Bates, M. & Zhuang, X. Sub-diffraction-limit imaging by stochastic optical

1548 reconstruction microscopy (STORM). *Nat Methods* **3**, 793-795, doi:nmeth929 [pii]

1549 10.1038/nmeth929 (2006).

1550 9 Heilemann, M. *et al.* Subdiffraction-resolution fluorescence imaging with conventional

1551 fluorescent probes. *Angew. Chemie. Int. Ed* **47**, 6172-6176 (2008).

1552 10 Sharonov, A. & Hochstrasser, R. M. Wide-field subdiffraction imaging by accumulated

1553 binding of diffusing probes. *Proceedings of the National Academy of Sciences* **103**,

1554 18911-18916, doi:10.1073/pnas.0609643104 (2006).

1555 11 Lidke, K., Rieger, B., Jovin, T. & Heintzmann, R. Superresolution by localization of

1556 quantum dots using blinking statistics. *Opt Express* **13**, 7052-7062,

1557 doi:10.1364/opex.13.007052 (2005).

1558 12 van Oijen, A. M., Kohler, J., Schmidt, J., Muller, M. & Brakenhoff, G. J. 3-Dimensional

1559 super-resolution by spectrally selective imaging. *Chem Phys Lett* **292**, 183-187, doi:Doi

1560 10.1016/S0009-2614(98)00673-3 (1998).

1561 13 Gordon, M. P., Ha, T. & Selvin, P. R. Single-molecule high-resolution imaging with

1562 photobleaching. *Proc Natl Acad Sci U S A* **101**, 6462-6465,

1563 doi:10.1073/pnas.0401638101 (2004).

1564 14 Heilemann, M. *et al.* High-resolution colocalization of single dye molecules by

1565 fluorescence lifetime imaging microscopy. *Anal Chem* **74**, 3511-3517,

1566 doi:10.1021/ac025576g (2002).

1567 15 Qu, X., Wu, D., Mets, L. & Scherer, N. F. Nanometer-localized multiple single-molecule

1568 fluorescence microscopy. *Proc Natl Acad Sci U S A* **101**, 11298-11303,

1569 doi:10.1073/pnas.0402155101 (2004).

1570 16 Manley, S. *et al.* High-density mapping of single-molecule trajectories with

1571 photoactivated localization microscopy. *Nature Methods* **5**, 155-157,

1572 doi:10.1038/nmeth.1176 (2008).

1573 17 Biteen, J. S. *et al.* Super-resolution imaging in live *Caulobacter crescentus* cells using

1574 photoswitchable EYFP. *Nat Methods* **5**, 947-949, doi:10.1038/nmeth.1258 (2008).

1575 18 Folling, J. *et al.* Fluorescence nanoscopy by ground-state depletion and single-molecule  
1576 return. *Nat Methods* **5**, 943-945, doi:10.1038/nmeth.1257 (2008).

1577 19 Schnitzbauer, J., Strauss, M. T., Schlichthaerle, T., Schueder, F. & Jungmann, R. Super-  
1578 resolution microscopy with DNA-PAINT. *Nat Protoc* **12**, 1198-1228,  
1579 doi:10.1038/nprot.2017.024 (2017).

1580 20 Bintu, B. *et al.* Super-resolution chromatin tracing reveals domains and cooperative  
1581 interactions in single cells. *Science* **362**, eaau1783, doi:10.1126/science.aau1783  
1582 (2018).

1583 21 Weisenburger, S. *et al.* Cryogenic optical localization provides 3D protein structure data  
1584 with Angstrom resolution. *Nat Methods* **14**, 141-144, doi:10.1038/nmeth.4141 (2017).

1585 22 Klein, T., Proppert, S. & Sauer, M. Eight years of single-molecule localization  
1586 microscopy. *Histochem Cell Biol* **141**, 561-575, doi:10.1007/s00418-014-1184-3 (2014).

1587 23 Bates, M., Blosser, T. R. & Zhuang, X. Short-range spectroscopic ruler based on a  
1588 single-molecule optical switch. *Phys Rev Lett* **94**, 108101,  
1589 doi:10.1103/PhysRevLett.94.108101 (2005).

1590 24 Heilemann, M., Margeat, E., Kasper, R., Sauer, M. & Tinnefeld, P. Carbocyanine Dyes  
1591 as Efficient Reversible Single-Molecule Optical Switch. *J. Am. Chem. Soc.* **127**, 3801-  
1592 3806, doi:10.1021/ja044686x  
1593 10.1021/ja044686x (2005).

1594 25 Lin, Y. *et al.* Quantifying and optimizing single-molecule switching nanoscopy at high  
1595 speeds. *PLoS One* **10**, e0128135, doi:10.1371/journal.pone.0128135 (2015).

1596 26 Diekmann, R. *et al.* Optimizing imaging speed and excitation intensity for single-  
1597 molecule localization microscopy. *Nat Methods* **17**, 909-912, doi:10.1038/s41592-020-  
1598 0918-5 (2020).

1599 27 van de Linde, S. *et al.* Direct stochastic optical reconstruction microscopy with standard  
1600 fluorescent probes. *Nature protocols* **6**, 991-1009, doi:10.1038/nprot.2011.336 (2011).

1601 28 Wombacher, R. *et al.* Live-cell super-resolution imaging with trimethoprim conjugates.  
1602 *Nature Methods* **7**, 717-719 (2010).

1603 29 Andresen, M. *et al.* Structural basis for reversible photoswitching in Dronpa. *Proceedings*  
1604 *of the National Academy of Sciences* **104**, 13005, doi:10.1073/pnas.0700629104 (2007).

1605 30 Bossi, M. *et al.* Multicolor Far-Field Fluorescence Nanoscopy through Isolated Detection  
1606 of Distinct Molecular Species. *Nano Lett.* **8**, 2463-2468, doi:10.1021/nl801471d  
1607 10.1021/nl801471d (2008).

1608 31 Grimm, J. B. *et al.* Bright photoactivatable fluorophores for single-molecule imaging. *Nat*  
1609 *Methods* **13**, 985-988, doi:10.1038/nmeth.4034 (2016).

1610 32 Michie, M. S. *et al.* Cyanine Conformational Restraint in the Far-Red Range. *J Am Chem*  
1611 *Soc* **139**, 12406-12409, doi:10.1021/jacs.7b07272 (2017).

1612 33 Lukyanov, K. A., Chudakov, D. M., Lukyanov, S. & Verkhusha, V. V. Photoactivatable  
1613 fluorescent proteins. *Nature Reviews Molecular Cell Biology* **6**, 885-890,  
1614 doi:10.1038/nrm1741 (2005).

1615 34 Shroff, H., Galbraith, C. G., Galbraith, J. A. & Betzig, E. Live-cell photoactivated  
1616 localization microscopy of nanoscale adhesion dynamics. *Nature Methods* **5**, 417-423,  
1617 doi:10.1038/nmeth.1202 (2008).

1618 35 Wang, S., Moffitt, J. R., Dempsey, G. T., Xie, X. S. & Zhuang, X. Characterization and  
1619 development of photoactivatable fluorescent proteins for single-molecule-based  
1620 superresolution imaging. *Proc Natl Acad Sci U S A* **111**, 8452-8457,  
1621 doi:10.1073/pnas.1406593111 (2014).

1622 36 Turkowyd, B., Virant, D. & Endesfelder, U. From single molecules to life: microscopy at  
1623 the nanoscale. *Anal Bioanal Chem* **408**, 6885-6911, doi:10.1007/s00216-016-9781-8  
1624 (2016).

- 1625 37 McEvoy, A. L. *et al.* mMaple: a photoconvertible fluorescent protein for use in multiple  
1626 imaging modalities. *PLoS One* **7**, e51314, doi:10.1371/journal.pone.0051314 (2012).
- 1627 38 Uno, S. N. *et al.* A spontaneously blinking fluorophore based on intramolecular  
1628 spirocyclization for live-cell super-resolution imaging. *Nat Chem* **6**, 681-689,  
1629 doi:10.1038/nchem.2002 (2014).
- 1630 39 Takakura, H. *et al.* Long time-lapse nanoscopy with spontaneously blinking membrane  
1631 probes. *Nat Biotechnol* **35**, 773-780, doi:10.1038/nbt.3876 (2017).
- 1632 40 Uno, S. N., Kamiya, M., Morozumi, A. & Urano, Y. A green-light-emitting, spontaneously  
1633 blinking fluorophore based on intramolecular spirocyclization for dual-colour super-  
1634 resolution imaging. *Chem Commun (Camb)* **54**, 102-105, doi:10.1039/c7cc07783a  
1635 (2017).
- 1636 41 Macdonald, P. J. *et al.* Rhodamine-Derived Fluorescent Dye with Inherent Blinking  
1637 Behavior for Super-Resolution Imaging. *Anal Chem* **90**, 9165-9173,  
1638 doi:10.1021/acs.analchem.8b01645 (2018).
- 1639 42 Giannone, G. *et al.* Dynamic superresolution imaging of endogenous proteins on living  
1640 cells at ultra-high density. *Biophys J* **99**, 1303-1310, doi:10.1016/j.bpj.2010.06.005  
1641 (2010).
- 1642 43 Jungmann, R. *et al.* Single-molecule kinetics and super-resolution microscopy by  
1643 fluorescence imaging of transient binding on DNA origami. *Nano Lett* **10**, 4756-4761,  
1644 doi:10.1021/nl103427w (2010).
- 1645 44 Dai, M., Jungmann, R. & Yin, P. Optical imaging of individual biomolecules in densely  
1646 packed clusters. *Nat Nanotechnol* **11**, 798-807, doi:10.1038/nnano.2016.95 (2016).
- 1647 45 Shcherbakova, D. M., Sengupta, P., Lippincott-Schwartz, J. & Verkhusha, V. V.  
1648 Photocontrollable fluorescent proteins for superresolution imaging. *Annu Rev Biophys*  
1649 **43**, 303-329, doi:10.1146/annurev-biophys-051013-022836 (2014).
- 1650 46 Thorn, K. Genetically encoded fluorescent tags. *Mol Biol Cell* **28**, 848-857,  
1651 doi:10.1091/mbc.E16-07-0504 (2017).
- 1652 47 Rodriguez, E. A. *et al.* The Growing and Glowing Toolbox of Fluorescent and  
1653 Photoactive Proteins. *Trends Biochem Sci* **42**, 111-129, doi:10.1016/j.tibs.2016.09.010  
1654 (2017).
- 1655 48 Li, H. & Vaughan, J. C. Switchable Fluorophores for Single-Molecule Localization  
1656 Microscopy. *Chem Rev* **118**, 9412-9454, doi:10.1021/acs.chemrev.7b00767 (2018).
- 1657 49 Fernandez-Suarez, M. & Ting, A. Y. Fluorescent probes for super-resolution imaging in  
1658 living cells. *Nat Rev Mol Cell Biol* **9**, 929-943, doi:10.1038/nrm2531 (2008).
- 1659 50 Ries, J., Kaplan, C., Platonova, E., Eghlidi, H. & Ewers, H. A simple, versatile method for  
1660 GFP-based super-resolution microscopy via nanobodies. *Nat Methods* **9**, 582-584,  
1661 doi:10.1038/nmeth.1991 (2012).
- 1662 51 Herce, H. D. *et al.* Cell-permeable nanobodies for targeted immunolabelling and antigen  
1663 manipulation in living cells. *Nat Chem* **9**, 762-771, doi:10.1038/nchem.2811 (2017).
- 1664 52 Conic, S. *et al.* Imaging of native transcription factors and histone phosphorylation at  
1665 high resolution in live cells. *Journal of Cell Biology* **217**, 1537-1552,  
1666 doi:10.1083/jcb.201709153 (2018).
- 1667 53 Schnell, U., Dijk, F., Sjollem, K. A. & Giepmans, B. N. Immunolabeling artifacts and the  
1668 need for live-cell imaging. *Nat Methods* **9**, 152-158, doi:10.1038/nmeth.1855 (2012).
- 1669 54 Yan, Q. & Bruchez, M. P. Advances in chemical labeling of proteins in living cells. *Cell*  
1670 *Tissue Res* **360**, 179-194, doi:10.1007/s00441-015-2145-4 (2015).
- 1671 55 Liss, V., Barlag, B., Nietschke, M. & Hensel, M. Self-labelling enzymes as universal tags  
1672 for fluorescence microscopy, super-resolution microscopy and electron microscopy. *Sci*  
1673 *Rep* **5**, 17740, doi:10.1038/srep17740 (2015).
- 1674 56 Lelek, M., Di Nunzio, F. & Zimmer, C. in *Exocytosis and Endocytosis Methods in*  
1675 *Molecular Biology* (ed Andrei I. Ivanov) 183-193 (Springer New York, 2014).

1676 57 Klein, T. *et al.* Live-cell dSTORM with SNAP-tag fusion proteins. *Nat Methods* **8**, 7-9,  
1677 doi:nmeth0111-7b [pii] 10.1038/nmeth0111-7b (2011).

1678 58 Xu, K., Zhong, G. & Zhuang, X. Actin, Spectrin, and Associated Proteins Form a Periodic  
1679 Cytoskeletal Structure in Axons. *Science* **339** (2013).

1680 59 Wijesooriya, C. S. *et al.* A Photoactivatable BODIPY Probe for Localization-Based  
1681 Super-Resolution Cellular Imaging. *Angew Chem Int Ed Engl* **57**, 12685-12689,  
1682 doi:10.1002/anie.201805827 (2018).

1683 60 Shim, S. H. *et al.* Super-resolution fluorescence imaging of organelles in live cells with  
1684 photoswitchable membrane probes. *Proceedings of the National Academy of Sciences*  
1685 *of the United States of America* **109**, 13978-13983, doi:10.1073/pnas.1201882109  
1686 (2012).

1687 61 Neubert, F. *et al.* Bioorthogonal Click Chemistry Enables Site-specific Fluorescence  
1688 Labeling of Functional NMDA Receptors for Super-Resolution Imaging. *Angew Chem Int*  
1689 *Ed Engl* **57**, 16364-16369, doi:10.1002/anie.201808951 (2018).

1690 62 Beliu, G. *et al.* Bioorthogonal labeling with tetrazine-dyes for super-resolution  
1691 microscopy. *Commun Biol* **2**, 261, doi:10.1038/s42003-019-0518-z (2019).

1692 63 Lang, K. & Chin, J. W. Cellular incorporation of unnatural amino acids and bioorthogonal  
1693 labeling of proteins. *Chem Rev* **114**, 4764-4806, doi:10.1021/cr400355w (2014).

1694 64 Lew, M. D. *et al.* Three-dimensional superresolution colocalization of intracellular protein  
1695 superstructures and the cell surface in live *Caulobacter crescentus*. *Proc Natl Acad Sci*  
1696 *U S A* **108**, E1102-1110, doi:10.1073/pnas.1114444108 (2011).

1697 65 Spahn, C. K. *et al.* A toolbox for multiplexed super-resolution imaging of the *E. coli*  
1698 nucleoid and membrane using novel PAINT labels. *Sci Rep* **8**, 14768,  
1699 doi:10.1038/s41598-018-33052-3 (2018).

1700 66 Agasti, S. S. *et al.* DNA-barcoded labeling probes for highly multiplexed Exchange-  
1701 PAINT imaging. *Chem Sci* **8**, 3080-3091, doi:10.1039/c6sc05420j (2017).

1702 67 Schlichthaerle, T. *et al.* Direct Visualization of Single Nuclear Pore Complex Proteins  
1703 Using Genetically-Encoded Probes for DNA-PAINT. *Angew Chem Int Ed Engl* **58**,  
1704 13004-13008, doi:10.1002/anie.201905685 (2019).

1705 68 Sograte-Idrissi, S. *et al.* Circumvention of common labelling artefacts using secondary  
1706 nanobodies. *Nanoscale* **12**, 10226-10239, doi:10.1039/d0nr00227e (2020).

1707 69 Schlichthaerle, T. *et al.* Site-Specific Labeling of Affimers for DNA-PAINT Microscopy.  
1708 *Angew Chem Int Ed Engl* **57**, 11060-11063, doi:10.1002/anie.201804020 (2018).

1709 70 Strauss, S. *et al.* Modified aptamers enable quantitative sub-10-nm cellular DNA-PAINT  
1710 imaging. *Nat Methods* **15**, 685-688, doi:10.1038/s41592-018-0105-0 (2018).

1711 71 Richter, K. N. *et al.* Glyoxal as an alternative fixative to formaldehyde in immunostaining  
1712 and super-resolution microscopy. *EMBO J* **37**, 139-159, doi:10.15252/embj.201695709  
1713 (2018).

1714 72 Tanaka, K. A. *et al.* Membrane molecules mobile even after chemical fixation. *Nat*  
1715 *Methods* **7**, 865-866, doi:10.1038/nmeth.f.314 (2010).

1716 73 Baumgart, F. *et al.* Varying label density allows artifact-free analysis of membrane-  
1717 protein nanoclusters. *Nat Methods* **13**, 661-664, doi:10.1038/nmeth.3897 (2016).

1718 74 Tuijtel, M. W., Koster, A. J., Jakobs, S., Faas, F. G. A. & Sharp, T. H. Correlative cryo  
1719 super-resolution light and electron microscopy on mammalian cells using fluorescent  
1720 proteins. *Sci Rep* **9**, 1369, doi:10.1038/s41598-018-37728-8 (2019).

1721 75 Kopek, B. G. *et al.* Diverse protocols for correlative super-resolution fluorescence  
1722 imaging and electron microscopy of chemically fixed samples. *Nat Protoc* **12**, 916-946,  
1723 doi:10.1038/nprot.2017.017 (2017).

1724 76 Waldchen, S., Lehmann, J., Klein, T., van de Linde, S. & Sauer, M. Light-induced cell  
1725 damage in live-cell super-resolution microscopy. *Sci Rep* **5**, 15348,  
1726 doi:10.1038/srep15348 (2015).

- 1727 77 Holm, T. *et al.* A blueprint for cost-efficient localization microscopy. *ChemPhysChem* **15**,  
1728 651-654 (2014).
- 1729 78 Kwakwa, K. *et al.* easySTORM: a robust, lower-cost approach to localisation and TIRF  
1730 microscopy. *Journal of Biophotonics* **9**, 948-957 (2016).
- 1731 79 Henriques, R. *et al.* QuickPALM: 3D real-time photoactivation nanoscopy image  
1732 processing in ImageJ. *Nature Methods* **7**, 339-340 (2010).
- 1733 80 Huang, B., Wang, W., Bates, M. & Zhuang, X. Three-dimensional super-resolution  
1734 imaging by stochastic optical reconstruction microscopy. *Science* **319**, 810-813,  
1735 doi:10.1126/science.1153529 (2008).
- 1736 81 Mashanov, G. I., Tacon, D., Knight, A. E., Peckham, M. & Molloy, J. E. Visualizing single  
1737 molecules inside living cells using total internal reflection fluorescence microscopy.  
1738 *Methods* **29**, 142-152, doi:10.1016/s1046-2023(02)00305-5 (2003).
- 1739 82 Tokunaga, M., Imamoto, N. & Sakata-Sogawa, K. Highly inclined thin illumination  
1740 enables clear single-molecule imaging in cells. *Nature methods* **5**, 159-161 (2008).
- 1741 83 Thompson, R. E., Larson, D. R. & Webb, W. W. Precise nanometer localization analysis  
1742 for individual fluorescent probes. *Biophys J* **82**, 2775-2783 (2002).
- 1743 84 Ober, R. J., Ram, S. & Ward, E. S. Localization Accuracy in Single-Molecule  
1744 Microscopy. *Biophysical journal* **86**, 1185-1200 (2004).
- 1745 85 Holden, S. J. *et al.* High throughput 3D super-resolution microscopy reveals *Caulobacter*  
1746 *crescentus* in vivo Z-ring organization. *Proceedings of the National Academy of*  
1747 *Sciences of the United States of America* **111**, 4566-4571 (2014).
- 1748 86 Kechkar, A., Nair, D., Heilemann, M., Choquet, D. & Sibarita, J. B. Real-Time Analysis  
1749 and Visualization for Single-Molecule Based Super-Resolution Microscopy. *PLoS ONE*  
1750 **8**, doi:10.1371/journal.pone.0062918 (2013).
- 1751 87 Mund, M. *et al.* Systematic Nanoscale Analysis of Endocytosis Links Efficient Vesicle  
1752 Formation to Patterned Actin Nucleation. *Cell* **174**, 884-896.e817,  
1753 doi:10.1016/j.cell.2018.06.032 (2018).
- 1754 88 Fox-Roberts, P. *et al.* Local dimensionality determines imaging speed in localization  
1755 microscopy. *Nat Commun* **8**, 13558-13558, doi:10.1038/ncomms13558 (2017).
- 1756 89 Legant, W. R. *et al.* High-density three-dimensional localization microscopy across large  
1757 volumes. *Nature Methods* **13**, 359-365, doi:10.1038/nmeth.3797 (2016).
- 1758 90 Jones, S. A., Shim, S. H., He, J. & Zhuang, X. Fast, three-dimensional super-resolution  
1759 imaging of live cells. *Nat Methods* **8**, 499-505, doi:nmeth.1605 [pii] 10.1038/nmeth.1605  
1760 (2011).
- 1761 91 Gelles, J., Schnapp, B. J. & Sheetz, M. P. Tracking kinesin-driven movements with  
1762 nanometre-scale precision. *Nature* **331**, 450-453 (1988).
- 1763 92 Sergé, A., Bertaux, N., Rigneault, H. & Marguet, D. Dynamic multiple-target tracing to  
1764 probe spatiotemporal cartography of cell membranes. *Nat Methods* **5**, 687-694,  
1765 doi:nmeth.1233 [pii] 10.1038/nmeth.1233 (2008).
- 1766 93 Elf, J. & Barkefors, I. Single-Molecule Kinetics in Living Cells. *Annu Rev Biochem* **88**,  
1767 635-659, doi:10.1146/annurev-biochem-013118-110801 (2019).
- 1768 94 Ovesny, M., Kiek, P., Borkovec, J., Vindrych, Z. & Hagen, G. M. ThunderSTORM: a  
1769 comprehensive ImageJ plug-in for PALM and STORM data analysis and super-  
1770 resolution imaging. *Bioinformatics* **30**, 2389-2390, doi:10.1093/bioinformatics/btu202  
1771 (2014).
- 1772 95 Cheng, C.-Y. & Hsieh, C.-L. Background Estimation and Correction for High-Precision  
1773 Localization Microscopy. *ACS Photonics* **4**, 1730-1739,  
1774 doi:10.1021/acsp Photonics.7b00238 (2017).
- 1775 96 Kay, S. M. *Fundamentals of Statistical Signal Processing, Volume 2: Detection Theory*.  
1776 (Prentice Hall PTR, 1998).
- 1777 97 Kay, S. M. *Fundamentals of statistical signal processing: estimation theory*. (1993).

1778 98 Mortensen, K. I., Churchman, L. S., Spudich, J. A. & Flyvbjerg, H. Optimized localization  
1779 analysis for single-molecule tracking and super-resolution microscopy. *Nature Methods*  
1780 **7**, 377-381, doi:10.1038/nmeth.1447 (2010).

1781 99 Sage, D. *et al.* Super-resolution fight club: assessment of 2D and 3D single-molecule  
1782 localization microscopy software. *Nature Methods* **16**, 387-395, doi:10.1038/s41592-  
1783 019-0364-4 (2019).

1784 100 Small, A. & Stahlheber, S. Fluorophore localization algorithms for super-resolution  
1785 microscopy. *Nature Methods* **11**, 267-279, doi:10.1038/nmeth.2844 (2014).

1786 101 Li, Y. *et al.* Real-time 3D single-molecule localization using experimental point spread  
1787 functions. *Nat Methods* **15**, 367-369, doi:10.1038/nmeth.4661 (2018).

1788 102 Aristov, A., Lelandais, B., Rensen, E. & Zimmer, C. ZOLA-3D allows flexible 3D  
1789 localization microscopy over an adjustable axial range. *Nat Commun* **9**, 2409,  
1790 doi:10.1038/s41467-018-04709-4 (2018).

1791 103 Sage, D. *et al.* Quantitative evaluation of software packages for single-molecule  
1792 localization microscopy. *Nature Methods* **12**, 717-724, doi:10.1038/nmeth.3442 (2015).

1793 104 Annibale, P., Vanni, S., Scarselli, M., Rothlisberger, U. & Radenovic, A. Identification of  
1794 clustering artifacts in photoactivated localization microscopy. *Nature Methods* **8**, 527-  
1795 528, doi:10.1038/nmeth.1627 (2011).

1796 105 Sengupta, P. *et al.* Probing protein heterogeneity in the plasma membrane using PALM  
1797 and pair correlation analysis. *Nat Methods* **8**, 969-975, doi:Doi 10.1038/Nmeth.1704  
1798 (2011).

1799 106 Rubin-Delanchy, P. *et al.* Bayesian cluster identification in single-molecule localization  
1800 microscopy data. *Nature Methods* **12**, 1072-1076, doi:10.1038/nmeth.3612 (2015).

1801 107 Khater, I. M., Nabi, I. R. & Hamarneh, G. A Review of Super-Resolution Single-Molecule  
1802 Localization Microscopy Cluster Analysis and Quantification Methods. *Patterns* **1**,  
1803 100038, doi:<https://doi.org/10.1016/j.patter.2020.100038> (2020).

1804 108 Levet, F. *et al.* SR-Tesseler: a method to segment and quantify localization-based super-  
1805 resolution microscopy data. *Nature Methods* **12**, 1065-1071, doi:10.1038/nmeth.3579  
1806 (2015).

1807 109 Durisic, N., Laparra-Cuervo, L., Sandoval-Alvarez, A., Borbely, J. S. & Lakadamyali, M.  
1808 Single-molecule evaluation of fluorescent protein photoactivation efficiency using an in  
1809 vivo nanotemplate. *Nat Methods* **11**, 156-162, doi:10.1038/nmeth.2784 (2014).

1810 110 Bohrer, C. H. *et al.* A Pairwise Distance Distribution Correction (DDC) algorithm to  
1811 eliminate blinking-caused artifacts in super-resolution microscopy. *bioRxiv*, 768051,  
1812 doi:10.1101/768051 (2020).

1813 111 Veatch, S. L. *et al.* Correlation functions quantify super-resolution images and estimate  
1814 apparent clustering due to over-counting. *PLoS One* **7**, e31457,  
1815 doi:10.1371/journal.pone.0031457 (2012).

1816 112 Zanicchi, F. C. *et al.* A DNA origami platform for quantifying protein copy number in  
1817 super-resolution. *Nat Methods* **14**, 789-792, doi:10.1038/nmeth.4342 (2017).

1818 113 Thevathasan, J. V. *et al.* Nuclear pores as versatile reference standards for quantitative  
1819 superresolution microscopy. *Nature Methods* **16**, 1045-1053, doi:10.1038/s41592-019-  
1820 0574-9 (2019).

1821 114 Finan, K., Raulf, A. & Heilemann, M. A set of homo-oligomeric standards allows accurate  
1822 protein counting. *Angew Chem Int Ed Engl* **54**, 12049-12052,  
1823 doi:10.1002/anie.201505664 (2015).

1824 115 Rollins, G. C., Shin, J. Y., Bustamante, C. & Presse, S. Stochastic approach to the  
1825 molecular counting problem in superresolution microscopy. *Proc Natl Acad Sci U S A*  
1826 **112**, E110-118, doi:10.1073/pnas.1408071112 (2015).

1827 116 Lee, S.-H., Shin, J. Y., Lee, A. & Bustamante, C. Counting single photoactivatable  
1828 fluorescent molecules by photoactivated localization microscopy (PALM). *Proceedings of*

1829 *the National Academy of Sciences of the United States of America* **109**, 17436-17441,  
1830 doi:10.1073/pnas.1215175109 (2012).

1831 117 Jungmann, R. *et al.* Quantitative super-resolution imaging with qPAINT. *Nat Methods* **13**,  
1832 439-442, doi:10.1038/nmeth.3804 (2016).

1833 118 Salas, D. *et al.* Angular reconstitution-based 3D reconstructions of nanomolecular  
1834 structures from superresolution light-microscopy images. *Proceedings of the National*  
1835 *Academy of Sciences* **114**, 9273-9278, doi:10.1073/pnas.1704908114 (2017).

1836 119 Sieben, C., Banterle, N., Douglass, K. M., Gönczy, P. & Manley, S. Multicolor single-  
1837 particle reconstruction of protein complexes. *Nature Methods* **15**, 777-780,  
1838 doi:10.1038/s41592-018-0140-x (2018).

1839 120 Szymborska, A. *et al.* Nuclear pore scaffold structure analyzed by super-resolution  
1840 microscopy and particle averaging. *Science (New York, N.Y.)* **341**, 655-658,  
1841 doi:10.1126/science.1240672 (2013).

1842 121 Bolte, S. & Cordelières, F. P. A guided tour into subcellular colocalization analysis in  
1843 light microscopy. *Journal of microscopy* **224**, 213-232 (2006).

1844 122 Lagache, T. *et al.* Mapping molecular assemblies with fluorescence microscopy and  
1845 object-based spatial statistics. *Nat Commun* **9**, 698, doi:10.1038/s41467-018-03053-x  
1846 (2018).

1847 123 Levet, F. *et al.* A tessellation-based colocalization analysis approach for single-molecule  
1848 localization microscopy. *Nat Commun* **10**, 2379, doi:10.1038/s41467-019-10007-4  
1849 (2019).

1850 124 Malkusch, S. *et al.* Coordinate-based colocalization analysis of single-molecule  
1851 localization microscopy data. *Histochemistry and Cell Biology* **137**, 1-10,  
1852 doi:10.1007/s00418-011-0880-5 (2012).

1853 125 Monnier, N. *et al.* Bayesian Approach to MSD-Based Analysis of Particle Motion in Live  
1854 Cells. *Biophysical Journal* **103**, 616-626 (2012).

1855 126 Beheiry, M. E., Dahan, M. & Masson, J.-B. InferenceMAP: mapping of single-molecule  
1856 dynamics with Bayesian inference. *Nature Methods* **12**, 594-595,  
1857 doi:10.1038/nmeth.3441 (2015).

1858 127 Martin, D. S., Forstner, M. B. & Kas, J. A. Apparent subdiffusion inherent to single  
1859 particle tracking. *Biophys J* **83**, 2109-2117, doi:10.1016/S0006-3495(02)73971-4 (2002).

1860 128 Masson, J. B. *et al.* Mapping the energy and diffusion landscapes of membrane proteins  
1861 at the cell surface using high-density single-molecule imaging and Bayesian inference:  
1862 application to the multiscale dynamics of glycine receptors in the neuronal membrane.  
1863 *Biophys J* **106**, 74-83, doi:10.1016/j.bpj.2013.10.027 (2014).

1864 129 Manzo, C. & Garcia-Parajo, M. F. A review of progress in single particle tracking: from  
1865 methods to biophysical insights. *Rep Prog Phys* **78**, 124601, doi:10.1088/0034-  
1866 4885/78/12/124601 (2015).

1867 130 Peters, R., Griffié, J., Burn, G. L., Williamson, D. J. & Owen, D. M. Quantitative fibre  
1868 analysis of single-molecule localization microscopy data. *Scientific Reports* **8**, 10418,  
1869 doi:10.1038/s41598-018-28691-5 (2018).

1870 131 Zhang, Z., Nishimura, Y. & Kanchanawong, P. Extracting microtubule networks from  
1871 superresolution single-molecule localization microscopy data. *Molecular Biology of the*  
1872 *Cell* **28**, 333-345, doi:10.1091/mbc.E16-06-0421 (2017).

1873 132 Gyparaki, M. T. *et al.* Tau forms oligomeric complexes on microtubules that are distinct  
1874 from pathological oligomers in disease. *bioRxiv* (2020).

1875 133 Nicovich, P. R., Owen, D. M. & Gaus, K. Turning single-molecule localization microscopy  
1876 into a quantitative bioanalytical tool. *Nature Protocols* **12**, 453-460,  
1877 doi:10.1038/nprot.2016.166 (2017).

1878 134 Deschout, H., Shivanandan, A., Annibale, P., Scarselli, M. & Radenovic, A. Progress in  
1879 quantitative single-molecule localization microscopy. *Histochemistry and cell biology*  
1880 **142**, doi:10.1007/s00418-014-1217-y (2014).

1881 135 Rowley, M. J. & Corces, V. G. Organizational principles of 3D genome architecture.  
1882 *Nature Reviews Genetics* **19**, 789-800, doi:10.1038/s41576-018-0060-8 (2018).

1883 136 Lakadamyali, M. & Cosma, M. P. Visualizing the genome in high resolution challenges  
1884 our textbook understanding. *Nature Methods* **17**, 371-379, doi:10.1038/s41592-020-  
1885 0758-3 (2020).

1886 137 Nozaki, T. *et al.* Dynamic Organization of Chromatin Domains Revealed by Super-  
1887 Resolution Live-Cell Imaging. *Mol Cell* **67**, 282-293 e287,  
1888 doi:10.1016/j.molcel.2017.06.018 (2017).

1889 138 Gomez-Garcia, P. A. *et al.* Mesoscale Modeling and Single-Nucleosome Tracking  
1890 Reveal Remodeling of Clutch Folding and Dynamics in Stem Cell Differentiation. *Cell*  
1891 *Rep* **34**, 108614, doi:10.1016/j.celrep.2020.108614 (2021).

1892 139 Ricci, M. A., Manzo, C., García-Parajo, M. F., Lakadamyali, M. & Cosma, M. P.  
1893 Chromatin fibers are formed by heterogeneous groups of nucleosomes in vivo. *Cell* **160**,  
1894 1145-1158, doi:10.1016/j.cell.2015.01.054 (2015).

1895 140 Otterstrom, J. *et al.* Super-resolution microscopy reveals how histone tail acetylation  
1896 affects DNA compaction within nucleosomes in vivo. *Nucleic Acids Res* **47**, 8470-8484,  
1897 doi:10.1093/nar/gkz593 (2019).

1898 141 Xu, J. *et al.* Super-Resolution Imaging of Higher-Order Chromatin Structures at Different  
1899 Epigenomic States in Single Mammalian Cells. *Cell Reports* **24**, 873-882,  
1900 doi:10.1016/j.celrep.2018.06.085 (2018).

1901 142 Zessin, P. J., Finan, K. & Heilemann, M. Super-resolution fluorescence imaging of  
1902 chromosomal DNA. *J Struct Biol* **177**, 344-348, doi:10.1016/j.jsb.2011.12.015 (2012).

1903 143 Boettiger, A. N. *et al.* Super-resolution imaging reveals distinct chromatin folding for  
1904 different epigenetic states. *Nature* **529**, 418-422, doi:10.1038/nature16496 (2016).

1905 144 Beagan, J. A. & Phillips-Cremins, J. E. On the existence and functionality of topologically  
1906 associating domains. *Nature Genetics* **52**, 8-16, doi:10.1038/s41588-019-0561-1 (2020).

1907 145 Nir, G. *et al.* Walking along chromosomes with super-resolution imaging, contact maps,  
1908 and integrative modeling. *PLoS Genetics* **14**, e1007872-e1007872,  
1909 doi:10.1371/journal.pgen.1007872 (2018).

1910 146 Boettiger, A. & Murphy, S. Advances in Chromatin Imaging at Kilobase-Scale  
1911 Resolution. *Trends Genet* **36**, 273-287, doi:10.1016/j.tig.2019.12.010 (2020).

1912 147 Cisse, I. I. *et al.* Real-time dynamics of RNA polymerase II clustering in live human cells.  
1913 *Science (New York, N.Y.)* **341**, 664-667, doi:10.1126/science.1239053 (2013).

1914 148 Cho, W. K. *et al.* RNA Polymerase II cluster dynamics predict mRNA output in living  
1915 cells. *eLife* **5**, doi:10.7554/eLife.13617 (2016).

1916 149 Cho, W. K. *et al.* Mediator and RNA polymerase II clusters associate in transcription-  
1917 dependent condensates. *Science* **361**, 412-415, doi:10.1126/science.aar4199 (2018).

1918 150 Hansen, A. S., Pustova, I., Cattoglio, C., Tjian, R. & Darzacq, X. CTCF and cohesin  
1919 regulate chromatin loop stability with distinct dynamics. *eLife* **6**, e25776,  
1920 doi:10.7554/eLife.25776 (2017).

1921 151 Wani, A. H. *et al.* Chromatin topology is coupled to Polycomb group protein subnuclear  
1922 organization. *Nat Commun* **7**, 1-13, doi:10.1038/ncomms10291 (2016).

1923 152 Löscherberger, A. *et al.* Super-resolution imaging visualizes the eightfold symmetry of  
1924 gp210 proteins around the nuclear pore complex and resolves the central channel with  
1925 nanometer resolution. *Journal of cell science* **125**, 570-575, doi:10.1242/jcs.098822  
1926 (2012).

- 1927 153 Broeken, J. *et al.* Resolution improvement by 3D particle averaging in localization  
1928 microscopy. *Methods and applications in fluorescence* **3**, 014003-014003,  
1929 doi:10.1088/2050-6120/3/1/014003 (2015).
- 1930 154 Mudumbi, K. C. *et al.* Nucleoplasmic signals promote directed transmembrane protein  
1931 import simultaneously via multiple channels of nuclear pores. *Nat Commun* **11**, 1-14,  
1932 doi:10.1038/s41467-020-16033-x (2020).
- 1933 155 Zhu, L., Zhang, W., Elnatan, D. & Huang, B. Faster STORM using compressed sensing.  
1934 *Nature Methods* **9**, 721-723, doi:10.1038/nmeth.1978 (2012).
- 1935 156 Bálint, Š., Vilanova, I. V., Álvarez, Á. S. & Lakadamyali, M. Correlative live-cell and  
1936 superresolution microscopy reveals cargo transport dynamics at microtubule  
1937 intersections. *Proceedings of the National Academy of Sciences of the United States of*  
1938 *America* **110**, 3375-3380, doi:10.1073/pnas.1219206110 (2013).
- 1939 157 Verdeny-Vilanova, I. *et al.* Vol. 130 1904-1916 (Company of Biologists Ltd, 2017).
- 1940 158 Mohan, N., Sorokina, E. M., Verdeny, I. V., Alvarez, A. S. & Lakadamyali, M.  
1941 Detyrosinated microtubules spatially constrain lysosomes facilitating lysosome-  
1942 autophagosome fusion. *Journal of Cell Biology* **218**, 632-643,  
1943 doi:10.1083/jcb.201807124 (2019).
- 1944 159 Jakobs, S. & Wurm, C. A. Vol. 20 9-15 (Elsevier Ltd, 2014).
- 1945 160 Brown, T. A. *et al.* Superresolution Fluorescence Imaging of Mitochondrial Nucleoids  
1946 Reveals Their Spatial Range, Limits, and Membrane Interaction. *Molecular and Cellular*  
1947 *Biology* **31**, 4994-5010, doi:10.1128/mcb.05694-11 (2011).
- 1948 161 Nixon-Abell, J. *et al.* Increased spatiotemporal resolution reveals highly dynamic dense  
1949 tubular matrices in the peripheral ER. *Science* **354**, doi:10.1126/science.aaf3928 (2016).
- 1950 162 Karathanasis, C. *et al.* Single-molecule imaging reveals the oligomeric state of functional  
1951 TNFalpha-induced plasma membrane TNFR1 clusters in cells. *Sci Signal* **13**,  
1952 doi:10.1126/scisignal.aax5647 (2020).
- 1953 163 Neumann, J. *et al.* Nanoscale distribution of TLR4 on primary human macrophages  
1954 stimulated with LPS and ATI. *Nanoscale* **11**, 9769-9779, doi:10.1039/c9nr00943d  
1955 (2019).
- 1956 164 Nerreter, T. *et al.* Super-resolution microscopy reveals ultra-low CD19 expression on  
1957 myeloma cells that triggers elimination by CD19 CAR-T. *Nat Commun* **10**, 3137,  
1958 doi:10.1038/s41467-019-10948-w (2019).
- 1959 165 Lillemeier, B. F. *et al.* TCR and Lat are expressed on separate protein islands on T cell  
1960 membranes and concatenate during activation. *Nature Immunology* **11**, 90-96,  
1961 doi:10.1038/ni.1832 (2010).
- 1962 166 Pagoon, S. V. *et al.* Functional role of T-cell receptor nanoclusters in signal initiation and  
1963 antigen discrimination. *Proceedings of the National Academy of Sciences of the United*  
1964 *States of America* **113**, E5454-E5463, doi:10.1073/pnas.1607436113 (2016).
- 1965 167 Rossboth, B. *et al.* TCRs are randomly distributed on the plasma membrane of resting  
1966 antigen-experienced T cells. *Nature Immunology* **19**, 821-827, doi:10.1038/s41590-018-  
1967 0162-7 (2018).
- 1968 168 Stone, M. B., Shelby, S. A. & Veatch, S. L. Super-Resolution Microscopy: Shedding  
1969 Light on the Cellular Plasma Membrane. *Chem Rev* **117**, 7457-7477,  
1970 doi:10.1021/acs.chemrev.6b00716 (2017).
- 1971 169 Kanchanawong, P. *et al.* Nanoscale architecture of integrin-based cell adhesions. *Nature*  
1972 **468**, 580-584, doi:10.1038/nature09621 (2010).
- 1973 170 Liu, J. *et al.* Talin determines the nanoscale architecture of focal adhesions. *Proceedings*  
1974 *of the National Academy of Sciences of the United States of America* **112**, E4864-  
1975 E4873, doi:10.1073/pnas.1512025112 (2015).

1976 171 Dani, A., Huang, B., Bergan, J., Dulac, C. & Zhuang, X. Superresolution Imaging of  
1977 Chemical Synapses in the Brain. *Neuron* **68**, 843-856, doi:10.1016/j.neuron.2010.11.021  
1978 (2010).

1979 172 Ehmann, N. *et al.* Quantitative super-resolution imaging of Bruchpilot distinguishes  
1980 active zone states. *Nat Commun* **5**, 1-12, doi:10.1038/ncomms5650 (2014).

1981 173 Nair, D. *et al.* Super-resolution imaging reveals that AMPA receptors inside synapses  
1982 are dynamically organized in nanodomains regulated by PSD95. *Journal of*  
1983 *Neuroscience* **33**, 13204-13224, doi:10.1523/JNEUROSCI.2381-12.2013 (2013).

1984 174 Kellermayer, B. *et al.* Differential Nanoscale Topography and Functional Role of GluN2-  
1985 NMDA Receptor Subtypes at Glutamatergic Synapses. *Neuron* **100**, 106-119.e107,  
1986 doi:10.1016/j.neuron.2018.09.012 (2018).

1987 175 Ladépêche, L. *et al.* NMDA Receptor Autoantibodies in Autoimmune Encephalitis Cause  
1988 a Subunit-Specific Nanoscale Redistribution of NMDA Receptors. *Cell Reports* **23**, 3759-  
1989 3768, doi:10.1016/j.celrep.2018.05.096 (2018).

1990 176 Siddig, S. *et al.* Super-resolution imaging reveals the nanoscale organization of  
1991 metabotropic glutamate receptors at presynaptic active zones. *Sci Adv* **6**, eaay7193,  
1992 doi:10.1126/sciadv.aay7193 (2020).

1993 177 Lehmann, M. *et al.* Quantitative multicolor super-resolution microscopy reveals tetherin  
1994 HIV-1 interaction. *PLoS Pathog* **7**, e1002456, doi:10.1371/journal.ppat.1002456 (2011).

1995 178 Chojnacki, J. & Eggeling, C. Super-resolution fluorescence microscopy studies of human  
1996 immunodeficiency virus. *Retrovirology* **15**, 41, doi:10.1186/s12977-018-0424-3 (2018).

1997 179 Pak, A. J. *et al.* Immature HIV-1 lattice assembly dynamics are regulated by scaffolding  
1998 from nucleic acid and the plasma membrane. *Proc Natl Acad Sci U S A* **114**, E10056-  
1999 E10065, doi:10.1073/pnas.1706600114 (2017).

2000 180 Lelek, M. *et al.* Superresolution imaging of HIV in infected cells with FIAsh-PALM. *Proc*  
2001 *Natl Acad Sci U S A* **109**, 8564-8569, doi:10.1073/pnas.1013267109 (2012).

2002 181 Van Engelenburg, S. B. *et al.* Distribution of ESCRT machinery at HIV assembly sites  
2003 reveals virus scaffolding of ESCRT subunits. *Science* **343**, 653-656,  
2004 doi:10.1126/science.1247786 (2014).

2005 182 Laine, R. F. *et al.* Structural analysis of herpes simplex virus by optical super-resolution  
2006 imaging. *Nat Commun* **6**, 5980, doi:10.1038/ncomms6980 (2015).

2007 183 Rincheval, V. *et al.* Functional organization of cytoplasmic inclusion bodies in cells  
2008 infected by respiratory syncytial virus. *Nat Commun* **8**, 563, doi:10.1038/s41467-017-  
2009 00655-9 (2017).

2010 184 Fu, G. *et al.* In vivo structure of the E. coli FtsZ-ring revealed by photoactivated  
2011 localization microscopy (PALM). *PLoS One* **5**, e12682,  
2012 doi:10.1371/journal.pone.0012680 (2010).

2013 185 Wang, W., Li, G. W., Chen, C., Xie, X. S. & Zhuang, X. Chromosome organization by a  
2014 nucleoid-associated protein in live bacteria. *Science* **333**, 1445-1449,  
2015 doi:10.1126/science.1204697 (2011).

2016 186 Mostowy, S. *et al.* Entrapment of intracytosolic bacteria by septin cage-like structures.  
2017 *Cell Host Microbe* **8**, 433-444, doi:10.1016/j.chom.2010.10.009 (2010).

2018 187 Singh, M. K. & Kenney, L. J. Super-resolution imaging of bacterial pathogens and  
2019 visualization of their secreted effectors. *FEMS Microbiol Rev*,  
2020 doi:10.1093/femsre/fuaa050 (2020).

2021 188 Williams, E. *et al.* The Image Data Resource: A Scalable Platform for Biological Image  
2022 Data Access, Integration, and Dissemination. *bioRxiv* (2016).

2023 189 Chen, S. Y., Heintzmann, R. & Cremer, C. Sample drift estimation method based on  
2024 speckle patterns formed by backscattered laser light. *Biomed Opt Express* **10**, 6462-  
2025 6475, doi:10.1364/BOE.10.006462 (2019).

2026 190 Wang, Y. *et al.* Localization events-based sample drift correction for localization  
2027 microscopy with redundant cross-correlation algorithm. *Opt. Express* **22**, 15982-15991,  
2028 doi:10.1364/OE.22.015982 (2014).

2029 191 McGorty, R., Kamiyama, D. & Huang, B. Active Microscope Stabilization in Three  
2030 Dimensions Using Image Correlation. *Opt Nanoscopy* **2**, doi:10.1186/2192-2853-2-3  
2031 (2013).

2032 192 Mlodzianoski, M. J. *et al.* Sample drift correction in 3D fluorescence photoactivation  
2033 localization microscopy. *Opt. Express* **19**, 15009, doi:10.1364/OE.19.015009 (2011).

2034 193 Lee, S. H. *et al.* Using fixed fiduciary markers for stage drift correction. *Opt Express* **20**,  
2035 12177-12183, doi:10.1364/oe.20.012177 (2012).

2036 194 Grover, G., Mohrman, W. & Piestun, R. Real-time adaptive drift correction for super-  
2037 resolution localization microscopy. *Opt. Express* **23**, 23887-23898,  
2038 doi:10.1364/OE.23.023887 (2015).

2039 195 Carter, A. R. *et al.* Stabilization of an optical microscope to 0.1 nm in three dimensions.  
2040 *Appl. Opt.* **46**, 421-427, doi:10.1364/AO.46.000421 (2007).

2041 196 Coelho, S. *et al.* Ultraprecise single-molecule localization microscopy enables in situ  
2042 distance measurements in intact cells. *Science Advances* **6**, eaay8271,  
2043 doi:10.1126/sciadv.aay8271 (2020).

2044 197 Pertsinidis, A., Zhang, Y. & Chu, S. Subnanometre single-molecule localization,  
2045 registration and distance measurements. *Nature* **466**, 647-651 (2010).

2046 198 Culley, S. *et al.* Quantitative mapping and minimization of super-resolution optical  
2047 imaging artifacts. *Nature Methods* **15**, 263-266, doi:10.1038/nmeth.4605 (2018).

2048 199 Marsh, R. J. *et al.* Artifact-free high-density localization microscopy analysis. *Nat*  
2049 *Methods* **15**, 689-692, doi:10.1038/s41592-018-0072-5 (2018).

2050 200 Dertinger, T., Colyer, R., Iyer, G., Weiss, S. & Enderlein, J. Fast, background-free, 3D  
2051 super-resolution optical fluctuation imaging (SOFI). *Proc Natl Acad Sci U S A* **106**,  
2052 22287-22292, doi:10.1073/pnas.0907866106 (2009).

2053 201 Ram, S., Ward, E. S. & Ober, R. J. Beyond Rayleigh's criterion: A resolution measure  
2054 with application to single-molecule microscopy. *Proceedings of the National Academy of*  
2055 *Sciences* **103**, 4457-4462 (2006).

2056 202 Gould, T. J., Verkhusha, V. V. & Hess, S. T. Imaging biological structures with  
2057 fluorescence photoactivation localization microscopy. *Nat Protoc* **4**, 291-308,  
2058 doi:10.1038/nprot.2008.246 (2009).

2059 203 Cabriel, C., Bourg, N., Dupuis, G. & Lévêque-Fort, S. Aberration-accounting calibration  
2060 for 3D single-molecule localization microscopy. *Opt. Lett.* **43**, 174-177,  
2061 doi:10.1364/OL.43.000174 (2018).

2062 204 Li, Y., Wu, Y.-L., Hoess, P., Mund, M. & Ries, J. Depth-dependent PSF calibration and  
2063 aberration correction for 3D single-molecule localization. *Biomed. Opt. Express* **10**,  
2064 2708-2718, doi:10.1364/BOE.10.002708 (2019).

2065 205 Engelhardt, J. *et al.* Molecular Orientation Affects Localization Accuracy in  
2066 Superresolution Far-Field Fluorescence Microscopy. *Nano Lett.* **11**, 209-213,  
2067 doi:10.1021/nl103472b (2011).

2068 206 Cruz, C. A. V. *et al.* Quantitative nanoscale imaging of orientational order in biological  
2069 filaments by polarized superresolution microscopy. *Proceedings of the National*  
2070 *Academy of Sciences* **113**, E820-E828, doi:10.1073/pnas.1516811113 (2016).

2071 207 Davis, J. L., Dong, B., Sun, C. & Zhang, H. F. Method to identify and minimize artifacts  
2072 induced by fluorescent impurities in single-molecule localization microscopy. *J Biomed*  
2073 *Opt* **23**, 1-14, doi:10.1117/1.JBO.23.10.106501 (2018).

2074 208 Sigal, Y. M., Speer, C. M., Babcock, H. P. & Correspondence, X. Z. Mapping Synaptic  
2075 Input Fields of Neurons with Super-Resolution Imaging In Brief. *Cell* **163**, 493-505,  
2076 doi:10.1016/j.cell.2015.08.033 (2015).

2077 209 German, C. L., Gudheti, M. V., Fleckenstein, A. E. & Jorgensen, E. M. Vol. 1663 153-  
2078 162 (Humana Press Inc., 2017).

2079 210 Xu, J. *et al.* Super-resolution imaging reveals the evolution of higher-order chromatin  
2080 folding in early carcinogenesis. *Nat Commun* **11**, 1-17, doi:10.1038/s41467-020-15718-7  
2081 (2020).

2082 211 Tobin, S. J. *et al.* Single molecule localization microscopy coupled with touch  
2083 preparation for the quantification of trastuzumab-bound HER2. *Sci Rep* **8**, 15154,  
2084 doi:10.1038/s41598-018-33225-0 (2018).

2085 212 Archetti, A. *et al.* Waveguide-PAINT offers an open platform for large field-of-view super-  
2086 resolution imaging. *Nat Commun* **10**, doi:10.1038/s41467-019-09247-1 (2019).

2087 213 Douglass, K. M., Sieben, C., Archetti, A., Lambert, A. & Manley, S. Super-resolution  
2088 imaging of multiple cells by optimized flat-field epi-illumination. *Nature Photonics* **10**,  
2089 705-708, doi:10.1038/nphoton.2016.200 (2016).

2090 214 Stehr, F., Stein, J., Schueder, F., Schwille, P. & Jungmann, R. Flat-top TIRF illumination  
2091 boosts DNA-PAINT imaging and quantification. *Nat Commun* **10**, doi:10.1038/s41467-  
2092 019-09064-6 (2019).

2093 215 Klevanski, M. *et al.* Automated highly multiplexed super-resolution imaging of protein  
2094 nano-architecture in cells and tissues. *Nat Commun* **11**, 1-11, doi:10.1038/s41467-020-  
2095 15362-1 (2020).

2096 216 Jungmann, R. *et al.* Multiplexed 3D cellular super-resolution imaging with DNA-PAINT  
2097 and Exchange-PAINT. *Nat Methods* **11**, 313-318, doi:10.1038/nmeth.2835 (2014).

2098 217 Schueder, F. *et al.* Universal Super-Resolution Multiplexing by DNA Exchange. *Angew  
2099 Chem Int Ed Engl* **56**, 4052-4055, doi:10.1002/anie.201611729 (2017).

2100 218 Wade, O. K. *et al.* 124-Color Super-resolution Imaging by Engineering DNA-PAINT  
2101 Blinking Kinetics. *Nano Lett* **19**, 2641-2646, doi:10.1021/acs.nanolett.9b00508 (2019).

2102 219 Gómez-García, P. A., Garbacik, E. T., Otterstrom, J. J., Garcia-Parajo, M. F. &  
2103 Lakadamyali, M. Excitation-multiplexed multicolor superresolution imaging with fm-  
2104 STORM and fm-DNA-PAINT. *Proceedings of the National Academy of Sciences of the  
2105 United States of America* **115**, 12991-12996, doi:10.1073/pnas.1804725115 (2018).

2106 220 Zhuang, X. Spatially resolved single-cell genomics and transcriptomics by imaging. *Nat  
2107 Methods* **18**, 18-22, doi:10.1038/s41592-020-01037-8 (2021).

2108 221 Beghin, A. *et al.* Localization-based super-resolution imaging meets high-content  
2109 screening. *Nature Methods* **14**, 1184-1190, doi:10.1038/nmeth.4486 (2017).

2110 222 Almada, P. *et al.* Automating multimodal microscopy with NanoJ-Fluidics. *Nat Commun*  
2111 **10**, 1-9, doi:10.1038/s41467-019-09231-9 (2019).

2112 223 Huang, F. *et al.* Video-rate nanoscopy using sCMOS camera-specific single-molecule  
2113 localization algorithms. *Nat Methods* **10**, 653-658, doi:10.1038/nmeth.2488 (2013).

2114 224 Barentine, A. E. S. *et al.* 3D Multicolor Nanoscopy at 10,000 Cells a Day. *bioRxiv*,  
2115 606954-606954, doi:10.1101/606954 (2019).

2116 225 Auer, A., Strauss, M. T., Schlichthaerle, T. & Jungmann, R. Fast, Background-Free  
2117 DNA-PAINT Imaging Using FRET-Based Probes. *Nano Lett* **17**, 6428-6434,  
2118 doi:10.1021/acs.nanolett.7b03425 (2017).

2119 226 Lee, J., Park, S. & Hohng, S. Accelerated FRET-PAINT microscopy. *Mol Brain* **11**, 70,  
2120 doi:10.1186/s13041-018-0414-3 (2018).

2121 227 Lee, J., Park, S., Kang, W. & Hohng, S. Accelerated super-resolution imaging with  
2122 FRET-PAINT. *Mol Brain* **10**, 63, doi:10.1186/s13041-017-0344-5 (2017).

2123 228 Schueder, F. *et al.* An order of magnitude faster DNA-PAINT imaging by optimized  
2124 sequence design and buffer conditions. *Nat Methods* **16**, 1101-1104,  
2125 doi:10.1038/s41592-019-0584-7 (2019).

2126 229 Filius, M. *et al.* High-Speed Super-Resolution Imaging Using Protein-Assisted DNA-  
2127 PAINT. *Nano Lett* **20**, 2264-2270, doi:10.1021/acs.nanolett.9b04277 (2020).

2128 230 Strauss, S. & Jungmann, R. Up to 100-fold speed-up and multiplexing in optimized DNA-  
2129 PAINT. *Nat Methods*, doi:10.1038/s41592-020-0869-x (2020).

2130 231 Diederich, B., Then, P., Jugler, A., Forster, R. & Heintzmann, R. cellSTORM-Cost-  
2131 effective super-resolution on a cellphone using dSTORM. *PLoS One* **14**, e0209827,  
2132 doi:10.1371/journal.pone.0209827 (2019).

2133 232 Ma, H., Fu, R., Xu, J. & Liu, Y. A simple and cost-effective setup for super-resolution  
2134 localization microscopy. *Sci Rep* **7**, 1542, doi:10.1038/s41598-017-01606-6 (2017).

2135 233 Auer, A. *et al.* Nanometer-scale Multiplexed Super-Resolution Imaging with an Economic  
2136 3D-DNA-PAINT Microscope. *Chemphyschem* **19**, 3024-3034,  
2137 doi:10.1002/cphc.201800630 (2018).

2138 234 Cella Zanacchi, F. *et al.* Live-cell 3D super-resolution imaging in thick biological  
2139 samples. *Nature Methods* **8**, 1047-1050, doi:10.1038/nmeth.1744 (2011).

2140 235 Huisken, J., Swoger, J., Del Bene, F., Wittbrodt, J. & Stelzer, E. H. Optical sectioning  
2141 deep inside live embryos by selective plane illumination microscopy. *Science* **305**, 1007-  
2142 1009, doi:10.1126/science.1100035 (2004).

2143 236 Waldchen, F. *et al.* Whole-cell imaging of plasma membrane receptors by 3D lattice  
2144 light-sheet dSTORM. *Nat Commun* **11**, 887, doi:10.1038/s41467-020-14731-0 (2020).

2145 237 Mlodzianoski, M. J. *et al.* Active PSF shaping and adaptive optics enable volumetric  
2146 localization microscopy through brain sections. *Nat Methods* **15**, 583-586,  
2147 doi:10.1038/s41592-018-0053-8 (2018).

2148 238 Sochacki, K. A., Shtengel, G., van Engelenburg, S. B., Hess, H. F. & Taraska, J. W.  
2149 Correlative super-resolution fluorescence and metal-replica transmission electron  
2150 microscopy. *Nat Methods* **11**, 305-308, doi:10.1038/nmeth.2816 (2014).

2151 239 Sochacki, K. A., Dickey, A. M., Strub, M. P. & Taraska, J. W. Endocytic proteins are  
2152 partitioned at the edge of the clathrin lattice in mammalian cells. *Nat Cell Biol* **19**, 352-  
2153 361, doi:10.1038/ncb3498 (2017).

2154 240 Vassilopoulos, S., Gibaud, S., Jimenez, A., Caillol, G. & Leterrier, C. Ultrastructure of the  
2155 axonal periodic scaffold reveals a braid-like organization of actin rings. *Nat Commun* **10**,  
2156 1-13, doi:10.1038/s41467-019-13835-6 (2019).

2157 241 Dahlberg, P. D. *et al.* Cryogenic single-molecule fluorescence annotations for electron  
2158 tomography reveal in situ organization of key proteins in *Caulobacter*. *Proc Natl Acad*  
2159 *Sci U S A* **117**, 13937-13944, doi:10.1073/pnas.2001849117 (2020).

2160 242 Hoffman, D. P. *et al.* Correlative three-dimensional super-resolution and block-face  
2161 electron microscopy of whole vitreously frozen cells. *Science* **367**,  
2162 doi:10.1126/science.aaz5357 (2020).

2163 243 Xu, K., Babcock, H. P. & Zhuang, X. Dual-objective STORM reveals three-dimensional  
2164 filament organization in the actin cytoskeleton. *Nat Methods* **9**, 185-188,  
2165 doi:10.1038/nmeth.1841 (2012).

2166 244 Shtengel, G. *et al.* Interferometric fluorescent super-resolution microscopy resolves 3D  
2167 cellular ultrastructure. *Proc Natl Acad Sci U S A* **106**, 3125-3130,  
2168 doi:10.1073/pnas.0813131106 (2009).

2169 245 Huang, F. *et al.* Ultra-High Resolution 3D Imaging of Whole Cells. *Cell* **166**, 1028-1040,  
2170 doi:10.1016/j.cell.2016.06.016 (2016).

2171 246 Balzarotti, F. *et al.* Nanometer resolution imaging and tracking of fluorescent molecules  
2172 with minimal photon fluxes. *Science* **355**, 606-612, doi:10.1126/science.aak9913 (2017).

2173 247 Cnossen, J. *et al.* Localization microscopy at doubled precision with patterned  
2174 illumination. *Nat Methods* **17**, 59-63, doi:10.1038/s41592-019-0657-7 (2020).

2175 248 Gu, L. *et al.* Molecular resolution imaging by repetitive optical selective exposure. *Nat*  
2176 *Methods* **16**, 1114-1118, doi:10.1038/s41592-019-0544-2 (2019).

2177 249 Gwosch, K. C. *et al.* MINFLUX nanoscopy delivers 3D multicolor nanometer resolution in  
2178 cells. *Nat Methods* **17**, 217-224, doi:10.1038/s41592-019-0688-0 (2020).

2179 250 Chen, F., Tillberg, P. W. & Boyden, E. S. Expansion microscopy. *Science* **347**, 543-548,  
2180 doi:10.1126/science.1260088 (2015).

2181 251 Chang, J. B. *et al.* Iterative expansion microscopy. *Nat Methods* **14**, 593-599,  
2182 doi:10.1038/nmeth.4261 (2017).

2183 252 Tillberg, P. W. *et al.* Protein-retention expansion microscopy of cells and tissues labeled  
2184 using standard fluorescent proteins and antibodies. *Nat Biotechnol* **34**, 987-992,  
2185 doi:10.1038/nbt.3625 (2016).

2186 253 Wen, G. *et al.* Evaluation of Direct Grafting Strategies via Trivalent Anchoring for  
2187 Enabling Lipid Membrane and Cytoskeleton Staining in Expansion Microscopy. *ACS*  
2188 *Nano*, doi:10.1021/acsnano.9b09259 (2020).

2189 254 Shi, X. *et al.* Label-retention expansion microscopy. *bioRxiv*, 687954-687954,  
2190 doi:10.1101/687954 (2019).

2191 255 Zwettler, F. U. *et al.* Molecular resolution imaging by post-labeling expansion single-  
2192 molecule localization microscopy (Ex-SMLM). *bioRxiv*, 2020.2003.2012.988923,  
2193 doi:10.1101/2020.03.12.988923 (2020).

2194 256 LeCun, Y., Bengio, Y. & Hinton, G. Deep learning. *Nature* **521**, 436-444,  
2195 doi:10.1038/nature14539 (2015).

2196 257 Mockl, L., Roy, A. R. & Moerner, W. E. Deep learning in single-molecule microscopy:  
2197 fundamentals, caveats, and recent developments [Invited]. *Biomed Opt Express* **11**,  
2198 1633-1661, doi:10.1364/BOE.386361 (2020).

2199 258 Nehme, E. *et al.* DeepSTORM3D: dense 3D localization microscopy and PSF design by  
2200 deep learning. *Nat Methods* **17**, 734-740, doi:10.1038/s41592-020-0853-5 (2020).

2201 259 Ouyang, W., Aristov, A., Lelek, M., Hao, X. & Zimmer, C. Deep learning massively  
2202 accelerates super-resolution localization microscopy. *Nature Biotechnology* **36**, 460-468,  
2203 doi:10.1038/nbt.4106 (2018).

2204 260 Weigert, M. *et al.* Content-aware image restoration: pushing the limits of fluorescence  
2205 microscopy. *Nature Methods* **15**, 1090, doi:10.1038/s41592-018-0216-7 (2018).

2206 261 Falk, T. *et al.* U-Net: deep learning for cell counting, detection, and morphometry. *Nat*  
2207 *Methods* **16**, 67-70, doi:10.1038/s41592-018-0261-2 (2019).

2208 262 Haberl, M. G. *et al.* CDeep3M-Plug-and-Play cloud-based deep learning for image  
2209 segmentation. *Nat Methods* **15**, 677-680, doi:10.1038/s41592-018-0106-z (2018).

2210 263 Belthangady, C. & Royer, L. A. Applications, promises, and pitfalls of deep learning for  
2211 fluorescence image reconstruction. *Nat Methods* **16**, 1215-1225, doi:10.1038/s41592-  
2212 019-0458-z (2019).

2213 264 Dempsey, G. T., Vaughan, J. C., Chen, K. H., Bates, M. & Zhuang, X. Evaluation of  
2214 fluorophores for optimal performance in localization-based super-resolution imaging. *Nat*  
2215 *Methods* **8**, 1027-1036, doi:10.1038/nmeth.1768 (2011).

2216 265 Jradi, F. M. & Lavis, L. D. Chemistry of Photosensitive Fluorophores for Single-Molecule  
2217 Localization Microscopy. *ACS Chem Biol* **14**, 1077-1090,  
2218 doi:10.1021/acscchembio.9b00197 (2019).

2219 266 Li, Y. *et al.* Real-time 3D single-molecule localization using experimental point spread  
2220 functions. *Nature Methods*, doi:10.1038/nmeth.4661 (2018).

2221 267 Ries, J. SMAP: a modular super-resolution microscopy analysis platform for SMLM data.  
2222 *Nat Methods* **17**, 870-872, doi:10.1038/s41592-020-0938-1 (2020).

2223 268 Jimenez, A., Friedl, K. & Leterrier, C. About samples, giving examples: Optimized Single  
2224 Molecule Localization Microscopy. *Methods* **174**, 100-114,  
2225 doi:10.1016/j.ymeth.2019.05.008 (2020).

2226 269 Manley, S., Gillette, J. M. & Lippincott-Schwartz, J. Single-particle tracking  
2227 photoactivated localization microscopy for mapping single-molecule dynamics. *Methods*  
2228 *Enzymol* **475**, 109-120, doi:10.1016/S0076-6879(10)75005-9 (2010).

2229 270 Kaplan, C. & Ewers, H. Optimized sample preparation for single-molecule localization-  
2230 based superresolution microscopy in yeast. *Nat Protoc* **10**, 1007-1021,  
2231 doi:10.1038/nprot.2015.060 (2015).

2232 271 Nieuwenhuizen, R. P. J. *et al.* Measuring image resolution in optical nanoscopy. *Nature*  
2233 *methods* **10**, 557-562, doi:10.1038/nmeth.2448 (2013).

2234 272 Descloux, A., Grussmayer, K. S. & Radenovic, A. Parameter-free image resolution  
2235 estimation based on decorrelation analysis. *Nat Methods* **16**, 918-924,  
2236 doi:10.1038/s41592-019-0515-7 (2019).

2237 273 Bates, M., Huang, B., Dempsey, G. T. & Zhuang, X. Multicolor Super-Resolution  
2238 Imaging with Photo-Switchable Fluorescent Probes. *Science*, 1146598v1146591 (2007).

2239 274 Flottmann, B. *et al.* Correlative light microscopy for high-content screening.  
2240 *Biotechniques* **55**, 243-252, doi:10.2144/000114099 (2013).

2241 275 Yan, R., Moon, S., Kenny, S. J. & Xu, K. Spectrally Resolved and Functional Super-  
2242 resolution Microscopy via Ultrahigh-Throughput Single-Molecule Spectroscopy. *Acc*  
2243 *Chem Res* **51**, 697-705, doi:10.1021/acs.accounts.7b00545 (2018).

2244 276 Testa, I. *et al.* Multicolor fluorescence nanoscopy in fixed and living cells by exciting  
2245 conventional fluorophores with a single wavelength. *Biophys J* **99**, 2686-2694,  
2246 doi:10.1016/j.bpj.2010.08.012 (2010).

2247 277 Dong, B. *et al.* Super-resolution spectroscopic microscopy via photon localization. *Nat*  
2248 *Commun* **7**, 12290, doi:10.1038/ncomms12290 (2016).

2249 278 Muranyi, W., Malkusch, S., Muller, B., Heilemann, M. & Krausslich, H. G. Super-  
2250 resolution microscopy reveals specific recruitment of HIV-1 envelope proteins to viral  
2251 assembly sites dependent on the envelope C-terminal tail. *PLoS Pathog* **9**, e1003198,  
2252 doi:10.1371/journal.ppat.1003198 (2013).

2253 279 Pavani, S. R. P. *et al.* Three-dimensional, single-molecule fluorescence imaging beyond  
2254 the diffraction limit by using a double-helix point spread function. *Proceedings of the*  
2255 *National Academy of Sciences of the United States of America* **106**, 2995-2999 (2009).

2256 280 Juette, M. F. *et al.* Three-dimensional sub-100 nm resolution fluorescence microscopy of  
2257 thick samples. *Nature Methods* **5**, 527-529 (2008).

2258 281 Abrahamsson, S. *et al.* Fast multicolor 3D imaging using aberration-corrected multifocus  
2259 microscopy. *Nature Methods* **10**, 60-63, doi:10.1038/NMETH.2277 (2013).

2260 282 Hajj, B., Beheiry, M. E., Izeddin, I., Darzacq, X. & Dahan, M. Accessing the third  
2261 dimension in localization-based super-resolution microscopy. *Physical Chemistry*  
2262 *Chemical Physics* **16**, 16340-16348, doi:10.1039/C4CP01380H (2014).

2263 283 Shechtman, Y., Sahl, S. J., Backer, A. S. & Moerner, W. E. Optimal point spread  
2264 function design for 3D imaging. *Physical Review Letters* **113**,  
2265 doi:10.1103/PhysRevLett.113.133902 (2014).

2266 284 Ram, S., Prabhat, P., Ward, E. S. & Ober, R. J. Improved single particle localization  
2267 accuracy with dual objective multifocal plane microscopy. *Opt Express* **17**, 6881-6898,  
2268 doi:10.1364/oe.17.006881 (2009).

2269